

Assessment of global phytoplankton growth inferred from satellite and
physiological model-based analyses



Dissertation

in fulfillment of the requirements for the degree

Dr.rer.nat.

of the Faculty of Mathematics and Natural Sciences

at Christian-Albrechts-Universität zu Kiel

submitted by

Lionel Alejandro Arteaga Quintero

Kiel, 2015

First referee: Prof. Dr. Andreas Oschlies

Second referee: Dr. Habil. Markus Pahlow

Date of oral examination: 27.05.2015

Approved for publication: 27.05.2015

Signed: Prof. Dr. Wolfgang J. Duschl

Contents

Summary	7
Zusammenfassung	9
1 Introduction	11
1.1 The carbon cycle	12
1.2 The biological carbon pump	12
1.3 Modelling phytoplankton growth and marine primary production	14
1.3.1 Satellite-based models	14
1.3.2 Mechanistic models of phytoplankton growth	18
1.3.3 Optimality-based models	20
1.4 Thesis overview and author contributions	23
References	25
2 Thesis chapters	33
2.1 Chapter 1: <i>Global patterns of phytoplankton nutrient and light colimitation inferred from an optimality-based model.</i>	33
2.2 Chapter 2: <i>Global monthly sea surface nitrate fields estimated from remotely sensed sea surface temperature, chlorophyll, and modeled mixed layer depth.</i>	49
2.3 Chapter 3: <i>Contribution of phytoplankton to particulate organic carbon in the global ocean.</i>	61
2.4 Chapter 4: <i>Nitrogen cycling driven by organic matter export in the South Pacific oxygen minimum zone.</i>	85
3 Synthesis	93
3.1 Phytoplankton C:N:P: acclimation vs. adaptation	93
3.2 Phytoplankton physiology and oceanic productivity	95
3.3 Coupling an optimality-based phytoplankton formulation into an Earth system climate model	97
3.3.1 Model implementation	97
3.3.2 Preliminary results	100
3.4 Conclusions and future directions	103
References	106

Acknowledgements	110
Curriculum Vitae	111
Eidesstattliche Erklärung	115

Summary

Prior to industrial times, the global carbon cycle is considered to have been roughly in a steady state, with no major net carbon fluxes between the different compartments of the Earth system. As a result of anthropogenic carbon emissions, fluxes as well as reservoirs have changed, and the ocean is now considered an important sink of carbon. Photosynthesis by phytoplankton constitutes the principal supply route of carbon into the marine ecosystem. Phytoplankton, hence, act as a major regulator of the carbon sink in the ocean. The main aim of this thesis is to evaluate the constraints of phytoplankton growth in the global ocean through a combination of satellite-based and novel physiological models. The broader goal of this work is to better describe and project biogeochemical cycles affected by the physiological regulation of phytoplankton elemental composition.

Chapter 1 of this thesis describes a global analysis of nutrient and light limitation of phytoplankton growth inferred from an optimality-based model. This analysis indicates strong nutrient limitation in the tropical and subtropical ocean, and light limitation in high latitudes, particularly in the Southern Ocean. Nutrient limitation is mainly due to nitrogen, while phosphorus acts as a secondary, co-limiting nutrient. Motivated by these results, a satellite- and model-based method to predict global surface nitrate variations was developed and is detailed in Chapter 2. This method is able to reproduce seasonal and interannual variations of in situ nitrate observations at four different stations: the Bermuda Atlantic Time Series, the Hawaii Ocean Time series, the California coast, and the southern New Zealand region. Chapter 3 combines the studies above to estimate global vertically integrated primary production rates and surface phytoplankton carbon concentration from an optimality-based model. Global patterns from this carbon-based model study show highest production rates in low latitudes, particularly in the Equatorial Pacific. Phytoplankton contribution to total particulate organic matter is also highest in tropical and subtropical regions ($\sim 50\%$), and decreases towards higher latitudes ($\sim 15\%$). Chapter 4 presents a study of nitrogen loss processes in the eastern tropical South Pacific oxygen minimum zone. The relevance of this work within the context of this thesis is the estimation of production and export rates combining bio-optical and satellite-based algorithms. The main conclusion from this work is that organic matter export regulates the lateral distribution and cycling of nitrogen in this oxygen minimum zone.

The results presented in this thesis show that optimality-based formulations can describe much of the variability in phytoplankton stoichiometry. Moreover, formulations of phytoplankton physiological acclimation can produce distinct global marine primary production patterns according to different nutrient and light colimitation regimes. Ongoing work evaluates the effects of coupling an optimality-based formulation into

an Earth system model. This work will permit to assess the sensitivity of marine biogeochemical cycles to changes in phytoplankton elemental composition, and its consequences on marine primary production and carbon export.

Zusammenfassung

In vorindustrieller Zeit war der globale Kohlenstoffkreislauf überwiegend im Gleichgewicht, ohne dass es signifikante netto Kohlenstoffflüsse zwischen den verschiedenen Bereichen des Erdsystems gab. In heutiger Zeit haben sich die Kohlenstoffflüsse und -reservoirs als Folge anthropogener Kohlenstoffemissionen verändert; der Ozean wird nunmehr als wichtige Senke für Kohlenstoff angesehen. Kohlenstoff wird größtenteils durch die Photosynthese von Phytoplankton in das marine Ökosystem eingebracht. Marines Phytoplankton reguliert somit einen Großteil der ozeanischen Kohlenstoffsенke. Das Hauptziel der vorliegenden Dissertation ist es, die Wachstumsbedingungen von Phytoplankton im globalen Ozean durch eine Kombination von satellitenbasierten und neuen, physiologischen Modellen zu analysieren, und dadurch die biogeochemischen Kreisläufe, die durch die phytoplanktonische Elementzusammensetzung beeinflusst werden, besser zu beschreiben und vorauszuberechnen.

Kapitel 1 der Dissertation analysiert die globalen Nährstoff- und Lichtlimitierungen auf das Phytoplanktonwachstum abgeleitet von einem optimalitätsbasierten Modell. Die Analyse deutet auf starke Nährstofflimitierung im tropischen und subtropischen Ozean, sowie Lichtlimitierung in den hohen Breitengraden, insbesondere im Antarktischen Ozean, hin. Die Nährstofflimitierung resultiert dabei primär aus limitierter Stickstoffverfügbarkeit, während Phosphor als sekundärer, co-limitierender Nährstoff fungiert. Basierend auf diesen Ergebnissen wurde in Kapitel 2 eine satelliten- und modelbasierte Methode entwickelt, welche global die Variationen von Nitrat im Oberflächenwasser berechnet. Die Methode vermag es, die in situ Nitrat Beobachtungen von vier verschiedenen Messstationen vorherzusagen: von der Bermuda Atlantik Zeitreihe, der Hawaii Ozean Zeitreihe, der Kalifornischen Küste, sowie der Region südlich von Neuseeland. Kapitel 3 kombiniert die genannten Studien, um global die vertikal-integrierten Primärproduktionsraten, sowie die Konzentration des Phytoplanktonkohlenstoffs im Oberflächenwasser mit einem optimalitätsbasierten Modell abzuschätzen. Diese kohlenstoffbasierte Modellstudie zeigt global den Trend höchster Produktionsraten in den niederen Breitengraden, insbesondere im äquatorialen Pazifik. Auch der Anteil von Phytoplankton am gesamten partikulären organischen Material ist in den tropischen und subtropischen Regionen am höchsten (50 %) und nimmt in Richtung höherer Breitengrade ab (15 %). Kapitel 4 präsentiert eine Untersuchung der Stickstoffverlustprozesse in der Sauerstoffminimumzone des tropischen Südostpazifiks. Die Bedeutung dieser Untersuchung im Zusammenhang der vorliegenden Dissertation ist die Abschätzung von Produktions- und Exportraten durch die Kombination von bio-optischen und satellitenbasierten Algorithmen. Die Hauptaussage ist, dass der Export von organischem Material die laterale Verteilung von Prozessen des Stickstoffkreislaufs in der Sauerstoffminimumzone reguliert.

Die Ergebnisse dieser Dissertation zeigen, dass optimalitätsbasierte Modelle einen Teil der Variabilität in Phytoplankton-Stöchiometry beschreiben können. Darüberhinaus können Modelle der physiologischen Anpassung des Phytoplanktons an verschiedene Nährstoff- und Lichtverhältnisse bestimmte globale Trends mariner Primärproduktion, entsprechend der gegebenen Co-Limitierung, produzieren. Eine noch laufende Studie bewertet den Effekt der Eingliederung einer optimalitätsbasierten Modelle in ein Erdsystem-Modell. Diese Arbeit wird es erlauben, die Empfindlichkeit mariner biogeochemischer Kreisläufe auf Veränderungen in phytoplanktischer Elementzusammensetzung, sowie deren Folgen für die marine Primärproduktion und den Kohlenstoffexport abzuschätzen.

1 Introduction

Over the last decades, there has been an increasing interest in understanding the fluxes and distribution of the major elements that regulate life on Earth. A great part of this interest is due to the realization that global biogeochemical cycles can be altered by human activities, resulting in changes in the balance of radiative energy of the Earth (Broecker, 1975), and hence global surface temperature (Fig. 1). However, the flux of elements between the different compartments of the planet (atmosphere, ocean, and land) also occurs under natural circumstances (i.e., not induced by human activities) (Broecker and Henderson, 1998), and these cycles regulate the composition of elements of the different compartments of Earth, as well as the overall temperature of the planet.

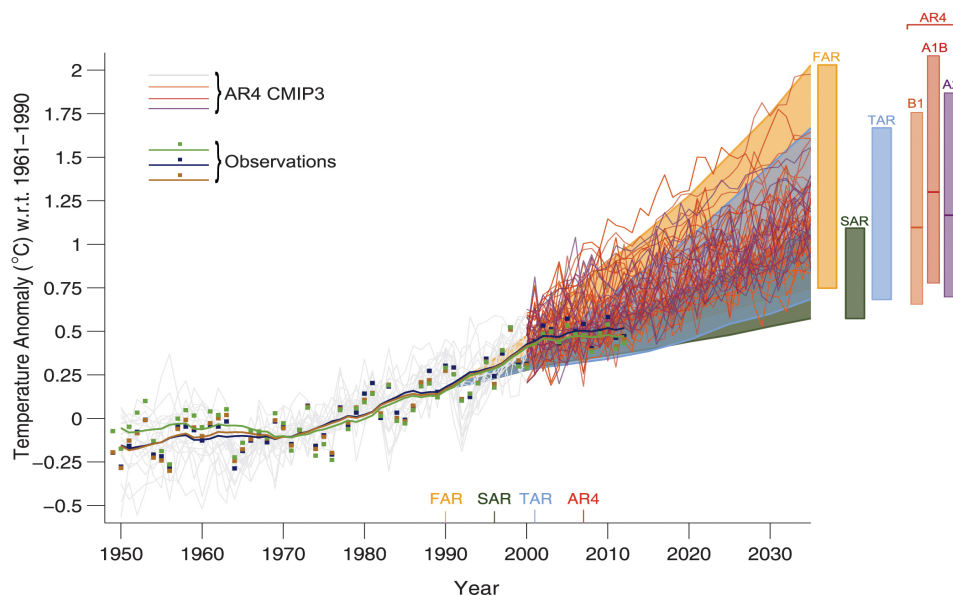


Figure 1: Estimated changes in the observed globally and annually averaged surface temperature anomaly relative to 1961-1990 (in $^{\circ}\text{C}$) since 1950 compared with the range of projections from the previous assessments of the Intergovernmental Panel on Climate Change (IPCC), taken from Cubasch et al. (2013). Values are harmonized to start from the same value in 1990. Observed global annual mean surface air temperature anomaly, relative to 1961-1990, is shown as squares and smoothed time series as solid lines (National Aeronautics and Space Administration (NASA) (dark blue), National Oceanic and Atmospheric Administration (NOAA) (warm mustard), and the UK Hadley Centre (bright green) reanalyses). The coloured shading shows the projected range of global annual mean surface air temperature change from 1990 to 2035 for models used in the First Assessment Report (FAR), Second Assessment Report (SAR), Third Assessment Report (TAR). For the Fourth Assessment Report (AR4) results are presented as single model runs of the third Coupled Model Intercomparison Project (CMIP3) ensemble for the historical period from 1950 to 2000 (light grey lines) and for three scenarios (A2, A1B and B1) from 2001 to 2035 (see Cubasch et al. (2013) for details). The bars at the right-hand side of the graph show the full range given for 2035 for each assessment report.

1.1 The carbon cycle

Carbon dioxide (CO_2) is among the most important gases affecting the radiative properties of the atmosphere, despite only comprising less than 1 % of the Earth’s atmosphere (*Cubasch et al., 2013*). The global carbon (C) cycle can be conceptually divided into two domains characterized by the C turnover time of each domain. The “fast exchange domain” includes carbon stored in the oceans, atmosphere, surface sediments, land vegetation, as well as freshwater sources, and is characterized by turnover times from years to decades and millennia. The “slow exchange domain” is the largest one, it includes carbon stored in rocks and deep sediments, and its turnover times are around 10,000 years or longer (*Ciais et al., 2013*). Carbon exchange between the two domains is relatively small ($< 0.3 \text{ Pg C y}^{-1}$), and it occurs through volcanism, chemical weathering, and sedimentation (*Ciais et al., 2013*). However, due to fossil fuel extraction and combustion, the amount of carbon released from geological reservoirs into the atmosphere has increased strongly over the Industrial Era, resulting in an accumulation of CO_2 in the atmosphere (*Canadell et al., 2007*) (Fig. 2).

The oceans constitute the largest reservoir of carbon within the “fast exchange domain”, with about 38,000 Pg C (*Sundquist, 1985, 1993*). Most of this carbon reservoir ($\sim 98 \%$) is in the form of dissolved inorganic carbon (DIC), while $\sim 700 \text{ Pg C}$ are estimated to be in the form of dissolved organic carbon (DOC) (*Hansell et al., 2009*). Prior to industrial times, the carbon cycle was considered to be roughly in a steady state, with the sum of all fluxes in and out of each reservoir being close to zero. As a result of anthropogenic carbon emissions, fluxes and reservoir sizes have changed (*Seigenthaler and Sarmiento, 1993*). The ocean is now considered to be an important sink of carbon. The average amount of C taken up by the ocean since the beginning of the industrial revolution has been estimated to be $\sim 1 \text{ Pg C y}^{-1}$ (*Tans et al., 1990; Sabine et al., 2004*). Carbon is transported into the ocean by gas transfer, which is mainly regulated by changes in temperature and salinity of the surface ocean, and the CO_2 partial pressure (pCO_2). Carbon is then further carried into the deep ocean through water convection driven by the global oceanic circulation. The overall mechanism of C sink into the ocean controlled mainly by physical processes is known as the Physical (or Solubility) Carbon Pump.

1.2 The biological carbon pump

The transport of carbon into the marine environment is also regulated by a set of processes carried out by living microorganisms, which constitute about 3 Pg C out of the total pool of 38,000 Pg C resident in the world’s oceans. This rather small amount of biomass represents $\sim 0.2 \%$ of global primary producer biomass, but is nonetheless responsible for about 50 % of the total C fixed into organic matter in the planet (*Field,*

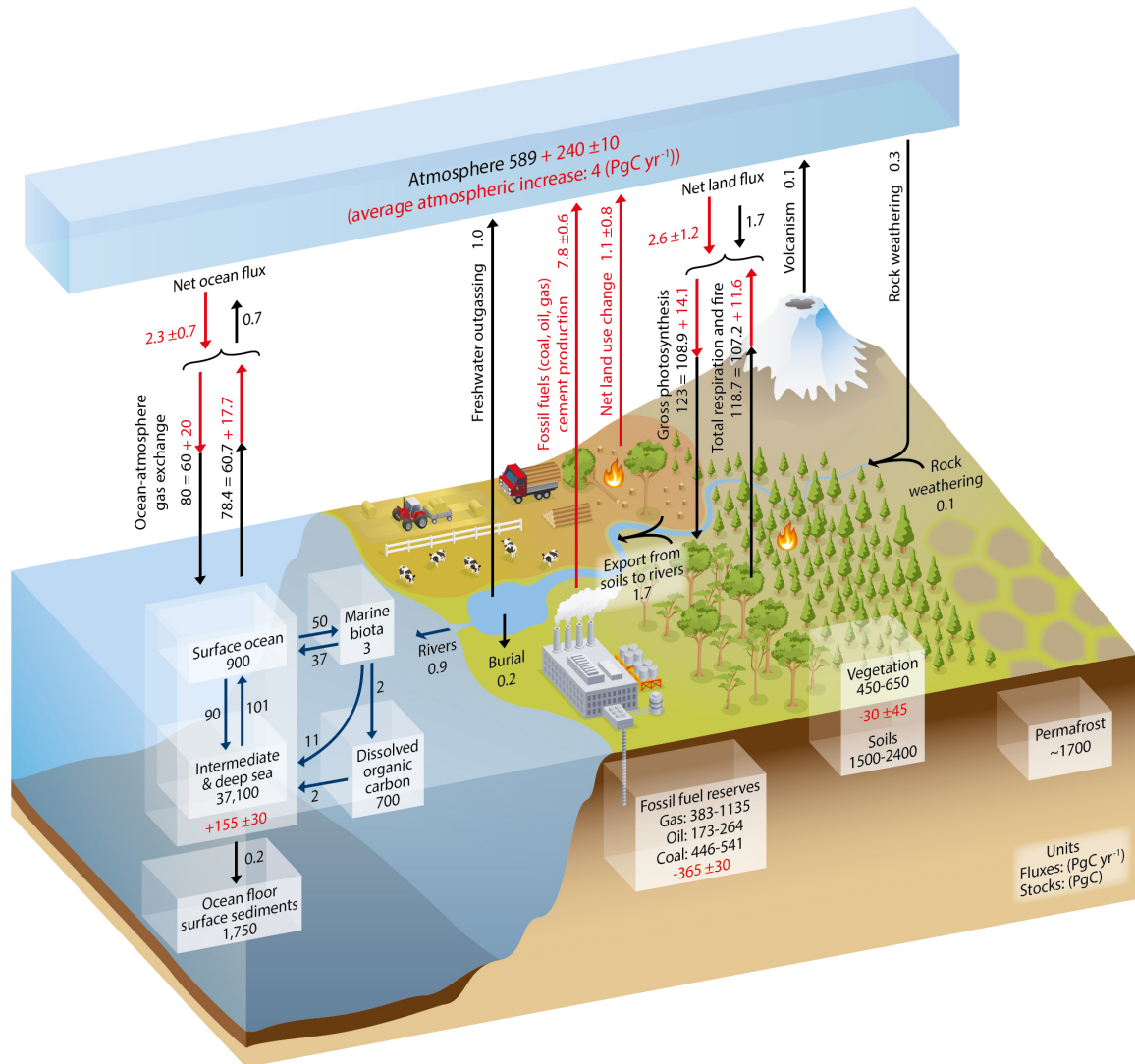


Figure 2: Simplified schematic of the global carbon cycle. Numbers represent reservoir mass in Pg C and annual carbon exchange fluxes (in Pg C yr⁻¹). Black numbers and arrows indicate reservoir mass and exchange fluxes estimated for the time prior to the Industrial Era, about 1750. Red arrows and numbers indicate annual anthropogenic fluxes averaged over the 2000-2009 time period. These fluxes are a perturbation of the carbon cycle during Industrial Era post 1750. The uptake of anthropogenic CO₂ by the ocean and by terrestrial ecosystems, often called carbon sinks, are the red arrows part of Net land flux and Net ocean flux. Red numbers in the reservoirs denote cumulative changes of anthropogenic carbon over the Industrial Period 1750-2011. By convention, a positive cumulative change means that a reservoir has gained carbon since 1750. Uncertainties are reported as 90 % confidence intervals. Taken from *Ciais et al. (2013)*.

1998). The set of processes by which C is fixed into organic (or inorganic) matter and eventually transferred to the deeper layers of the ocean is known as the Biological Carbon Pump. This biological pump is divided into: the organic or soft tissue pump driven by the formation of organic matter through photosynthesis; and the inorganic carbon pump, which results in the formation of inorganic carbon compounds and is driven by calcareous organisms. Both pumps have different immediate and long term consequences on the overall carbon cycle and CO₂ in particular. From here on, the term “biological carbon pump” will only refer to the organic carbon pump.

The biological carbon pump is a key process that transports photosynthetically fixed organic carbon from the sunlit surface layer to the deep ocean. Photosynthesis by phytoplankton constitutes the principal supply route of carbon into the marine ecosystem, contributing substantially to global biogeochemical fluxes, and hence acting as a major regulator of carbon sink in the ocean (*Raven and Falkowski, 1999*). The efficiency of the biological pump depends on how much of the carbon fixed by phytoplankton sinks into the deep ocean, and is prevented from immediate release back to the atmosphere. The efficiency of this carbon pump varies in different parts of the ocean (Fig. 3), and depends on physical properties as well as the overall trophic structure of the ecosystem (*Martin et al., 1987; Laws et al., 2000; Henson et al., 2012*).

The efficiency and strength of the biological pump is believed to have varied over geological time scales, influencing, for example, the development of glacial/interglacial cycles (*Sigman and Boyle, 2000*). Part of this variability is attributed to alterations of phytoplankton primary production (PP) and changes in nutrient availability and utilization (*Sigman and Boyle, 2000; Martin, 1990*). In the same manner, simulations of the future ocean predict a decrease in global primary production induced by changes in the availability of nutrients and light, mainly as a result of increased stratification of the surface ocean (*Sarmiento et al., 2004; Bopp et al., 2013*).

1.3 Modelling phytoplankton growth and marine primary production

1.3.1 Satellite-based models

Global marine primary production is $\sim 50 \text{ Pg C y}^{-1}$ (*Chavez et al., 2011*). Global estimates of marine PP are mainly obtained through satellite-based models. These models are founded on either idealized relationships between net photosynthesis and irradiance or measurements of net primary production (*Behrenfeld and Falkowski, 1997a*). These algorithms depend on remotely sensed global observations of chlorophyll (Chl) and irradiance. The spatial and temporal resolution obtained from remote sensing methods has not yet been achieved by any other observation system. Satellite-based algorithms have been used to estimate

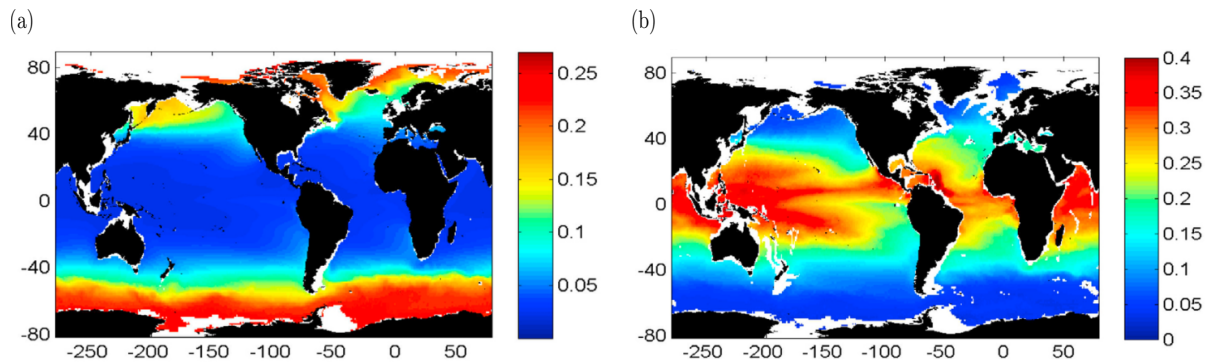


Figure 3: Global patterns in carbon export efficiency as shown in *Henson et al. (2012)*. a) Particulate export efficiency, defined as the ratio of particulate organic carbon (POC) at 100m to primary production (PP) (POC at 100m:PP). b) Transfer efficiency, defined as the fraction of exported organic carbon that reaches the deep ocean (flux of organic C at 2000m:POC export at 100 m).

global marine production rates from Coastal Zones Color Scanner data (CZCS) (*Longhurst et al., 1995; Antoine et al., 1996; Behrenfeld and Falkowski, 1997b*), the Sea-viewing Wide Field-of-view Sensor data (SeaWiFS) (*Behrenfeld et al., 2001*), and recently also from Moderate Resolution Imaging Spectroradiometer data (*Behrenfeld et al., 2005; Westberry et al., 2008*).

There is a wide range of bio-optical algorithms. The various models differ in the number and kind of environmental variables that they employ to estimate PP, the description of the vertical distribution of these properties within the euphotic zone, the number of parameters they use, and the general complexity of the models (*Campbell et al., 2002*). However, satellite-based models of marine PP are overall constrained by five main variables: surface phytoplankton biomass (C_{surf}), a photoadaptive variable (P_{opt}^b), euphotic depth (Z_{eu}), an irradiance dependent function (I), and daylength or photoperiod (D) (*Behrenfeld and Falkowski, 1997a*). Beyond this general structure, there is no clear difference in the ability of models to estimate PP, independently of the mathematical construction or complexity of the algorithms (*Campbell et al., 2002*).

One of the most commonly used PP satellite algorithms is the Vertical Generalized Production Model (VGPM, *Behrenfeld and Falkowski, 1997b*). The VGPM serves as a good example of a general bio-optical model. The VGPM estimates primary production integrated over the euphotic depth (PP_{eu}) via,

$$PP_{\text{eu}} = P_{\text{opt}}^b \cdot 0.66125 \cdot \frac{E_0}{E_0 + 4.1} \cdot Z_{\text{eu}} \cdot C_{\text{opt}} \cdot D \quad (1)$$

where E_0 is the sea surface daily photosynthetic active radiation (PAR) (mol quanta m^{-2}), and C_{opt} is the

Chl concentration (mg Chl m^{-3}) at $P_{\text{opt}}^{\text{b}}$ ($\text{mg C mg Chl}^{-1} \text{ h}^{-1}$) (commonly taken as surface concentration). Z_{eu} has units of meters (m), and D is the photoperiod in decimal hours. *Behrenfeld and Falkowski (1997b)* reached the conclusion that expanding the VGPM to explain PP_{eu} at each vertical level does not significantly increase the explanatory power of the model, and that the algorithm performance in estimating PP_{eu} is critically dependent on the ability to accurately represent spatial (i.e., horizontal) and temporal variability in $P_{\text{opt}}^{\text{b}}$. Once Z_{eu} , Chl concentration, and D were accounted for, PP could be adequately modeled with a simple formulation of an empirically determined, variable, light-dependent term ($\frac{E_0}{E_0+4.1}$) (*Behrenfeld and Falkowski, 1997b*).

A key variable characteristic of each bio-optical algorithm is the description of how light-saturated photosynthetic efficiency varies in the environment (*Campbell et al., 2002; Carr et al., 2006*). In the VGPM, this is described by $P_{\text{opt}}^{\text{b}}$, which represents the maximum C fixation rate in the water column. $P_{\text{opt}}^{\text{b}}$ varies exclusively as a function of sea surface temperature (SST) (Fig. 4). As $P_{\text{opt}}^{\text{b}}$ is mechanistically related to the Chl-normalized maximum rate of C fixation $P_{\text{max}}^{\text{b}}$ ($\text{mg C mg Chl}^{-1} \text{ h}^{-1}$), the dependence of $P_{\text{opt}}^{\text{b}}$ on SST is justified from a physiological perspective. Maximum photosynthetic rates are controlled by the capacity of Calvin cycle reactions and proportional to the number of functional photosynthetic reaction centers and their turnover rates (*Falkowski, 1980; Sukenik et al., 1987; Orellana and Perry, 1992*). However, the relation between $P_{\text{opt}}^{\text{b}}$ and SST also describes the global general connection between warmer waters, shallower surface mixing depths and higher surface radiation. These conditions favor high-light acclimated phytoplankton, leading to higher photosynthetic rates as SST increases. There is nonetheless a countering effect, as warm ocean areas are also generally accompanied by low surface nutrient concentrations, inducing nutrient limitation of phytoplankton growth. $P_{\text{opt}}^{\text{b}}$ starts to decrease beyond 20°C (Fig. 4). This decline is attributed to nutrient stress effects on phytoplankton (*Behrenfeld and Falkowski, 1997b*).

Most satellite-based PP models infer phytoplankton biomass from surface Chl concentrations. An important drawback of these models is that they do not account for the acclimation of phytoplankton to changes in the environment via the chlorophyll to carbon ratio (Chl:C). This simplification implies that variations in phytoplankton C biomass can be linearly derived from Chl concentrations, which is not generally true (*Geider et al., 1986; Armstrong, 2006*). Chl-based models, like the VGPM, show a global pattern of marine productivity with high PP rates in high latitudes and upwelling regions ($\sim 800 \text{ mg C m}^2 \text{ d}^{-1}$), and low PP ($< 200 \text{ mg C m}^2 \text{ d}^{-1}$) in tropical and subtropical regions, except for the Equatorial Pacific, where production rates are also high (Fig. 5a). Over recent years, optical models capable of estimating production rates based on carbon (instead of Chl) have been developed, showing important differences in the global

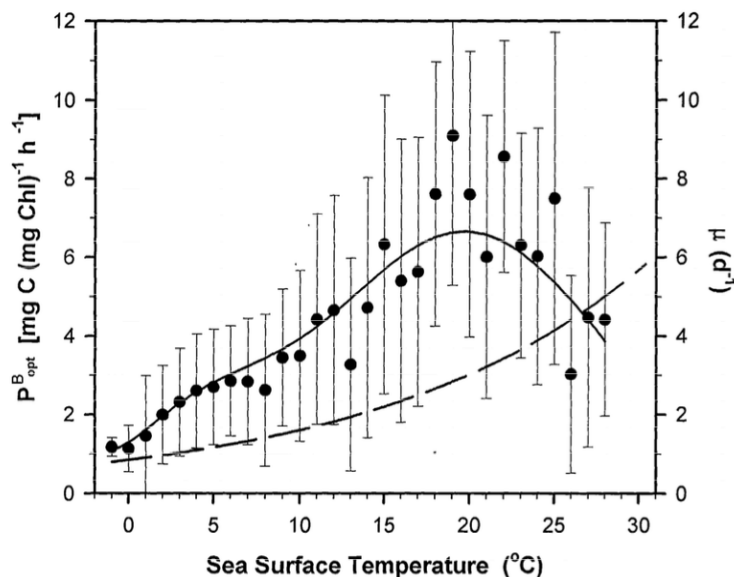


Figure 4: Measured (black dots, \pm standard deviation) and modeled (continuous line) photoadaptive parameter, $P_{\text{opt}}^{\text{B}}$, as a function of sea surface temperature (as presented in *Behrenfeld and Falkowski, 1997b*). Dashed curve indicates the theoretical maximum specific growth rate, μ (d^{-1}), of photoautotrophic unicellular algae described by *Eppley (1972)*.

distribution of oceanic PP (*Behrenfeld et al., 2005; Westberry et al., 2008*). These C-based models estimate higher production rates in low latitudes, particular over the Equatorial Pacific, Atlantic, and Indian Ocean (Fig. 5b). The differences and implications between the two approaches (Chl and C-based) will be further discussed in Chapter 3.

Satellite-based models are driven by the understanding of how photosynthetic rates vary as a function of biomass, temperature, and light. However, these formulations are inherently empirical and do not describe the physiological processes that lead to phytoplankton growth and carbon fixation. Oceanic primary production rates can also be inferred via the mechanistic description of the processes that limit phytoplankton growth. These kind of formulations are commonly combined with circulation models in order to project changes and trends in marine primary productivity and the future carbon cycle.

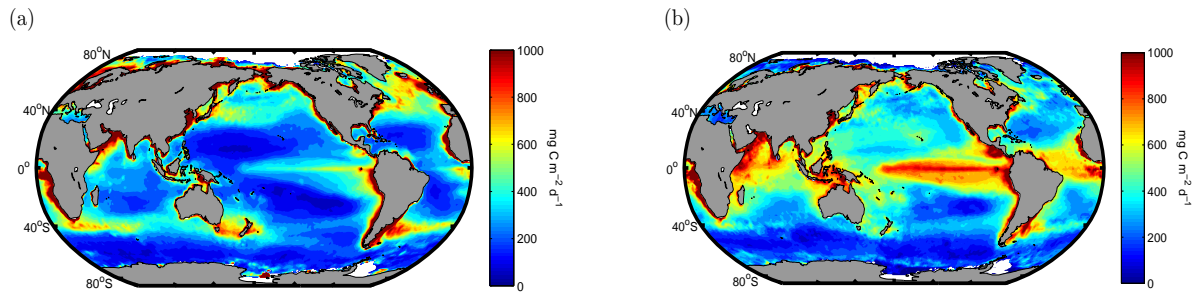


Figure 5: Global mean PP for 2005 estimated with a Chl-based (VGPM, *Behrenfeld and Falkowski, 1997b*) and a C-based model (*Westberry et al., 2008*).

1.3.2 Mechanistic models of phytoplankton growth

Nutrient limited phytoplankton growth is commonly represented by an hyperbolic function described by the Monod equation (Eq. 2, Fig. 6) (*Monod, 1949*),

$$\mu = \mu_{\max} \cdot \frac{S}{K + S} \quad (2)$$

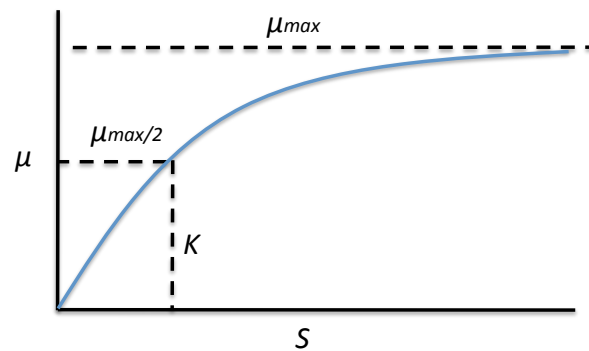


Figure 6: Schematic view of the rate of growth (μ) of phytoplankton as a function of nutrient concentration (S), as described by the Monod equation (*Monod, 1949*). μ_{\max} is the maximum growth rate under nutrient replete conditions, and K is the half-saturation constant.

where μ is the growth rate, μ_{\max} is the maximum growth rate under nutrient replete conditions, K is the concentration of the nutrient at which μ is half of μ_{\max} (i.e. half-saturation constant), and S is substrate or extracellular nutrient concentration. The Monod equation is identical the Michaelis-Menten equation

which describes enzyme kinetics. The Monod equation describes bacterial (and phytoplankton) growth as a function of one (limiting) nutrient. The treatment of multiple limiting nutrients is commonly dealt with by additive, multiplicative or threshold functional forms (O'Neill *et al.*, 1989).

The maximum growth rate (μ_{\max}) is obtained under replete nutrient and light conditions. In the ocean, the amount of available light is controlled by diverse factors such as the latitudinal position, time of the day, cloud coverage, as well as the attenuation of light in the water column caused by the absorption and scattering by particulates and dissolved organic matter (Sathyendranath and Platt, 1989). The response of photosynthesis (P) to irradiance (I) is described by the P-I curve (Fig. 7). The P-I curve looks somewhat similar to the Monod curve (Fig. 6). The P-I curve has been represented by a number of analytical expressions, some of which are similar to Eq. 2 (Platt and Jassby, 1976). Nutrient and light limited phytoplankton growth is commonly described by combining a formulation for P-I and Eq. 2.

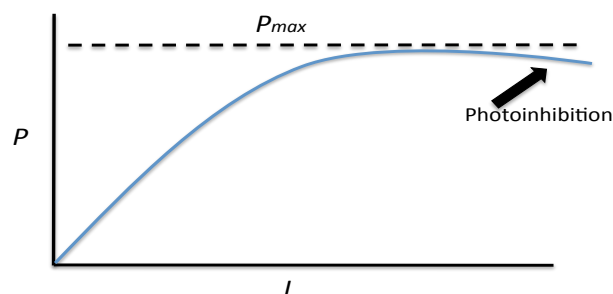


Figure 7: Schematic view of the rate of photosynthetic activity (P) as a function of irradiance (I). P_{\max} is the maximum photosynthetic rate. The P-I curve is similar to the Monod curve. A noticeable difference in the P-I curve is the final decrease in P as a product of photoinhibition due to excessive irradiation levels.

Phytoplankton growth is commonly simulated as a function of the most limiting nutrient employing Eq. 2. Nitrogen (N) is considered the most limiting nutrient in the global ocean, particularly over the tropical and subtropical areas, seconded by Phosphorus (P) (Moore *et al.*, 2013). Iron has also been identified as a limiting micronutrient in some marine environments such as the Equatorial Pacific (Behrenfeld *et al.*, 1996) and the Southern Ocean (Martin *et al.*, 1990). C-fixation rates are simulated by assuming a fixed cellular stoichiometric ratio among major limiting nutrients N, P, and C (Redfield ratio, Redfield, 1934). While the inference of constant elemental stoichiometry seems to hold on average for particulate organic matter (POM) in the global ocean, there is evidence of important variations across different latitudinal regimes (Martiny *et al.*, 2013a). The assumption of constant stoichiometry is at odds with observed temporal and regional variations of elemental composition of phytoplankton and associated biogeochemical fluxes (Geider

and La Roche, 2002; Körtzinger et al., 2001). C:N:P ratios are observed to vary widely among different groups of phytoplankton (Quigg et al., 2003; Klausmeier et al., 2004) and in response to nutrient and light limitation (Flynn, 2010). Furthermore, variations in the strength of the biological carbon pump resulting from phytoplankton acclimation to different nutrient and light regimes, or carbon fertilization induced via ocean acidification, cannot be assessed with models that do not allow for phytoplankton flexible stoichiometry. An alternative way of modelling growth and carbon uptake by phytoplankton is employing cell-quota and optimality-based models. Cell-quota models (e.g., Droop, 1983) are capable of decoupling C, N, and P, while optimality-based models of phytoplankton growth offer the potential to understand the interrelations between phytoplankton stoichiometry and primary production in the ocean (Smith et al., 2011).

1.3.3 Optimality-based models

The inclusion of several nutrients commonly uses multiplicative or threshold formulae to combine the respective individual limiting effects on phytoplankton growth. The application of several Michaelis-Menten equations to describe multiple nutrient limitation tends to overestimate the uptake rate of non-limiting nutrients when applied to data from chemostat experiments (Droop, 1974; Rhee, 1974). Most models account for multiple independent nutrient limitation (Saito et al., 2008), but do not fully describe the physiological effects of multiple-nutrient colimitation on phytoplankton growth. Several cell-quota and optimality-based models have been described yielding more accurate uptake rates for non-limiting nutrients, as well as a better description of the acclimation of photosynthetic cells to diverse light and nutrient regimes (Droop, 1973; Geider et al., 1998; Pahlow, 2005; Armstrong, 2006; Smith and Yamanaka, 2007; Pahlow et al., 2013). The kinetics of nutrient uptake are thought to resemble enzyme reactions (Lehninger, 1971). K , and the maximum uptake rate for a given nutrient (V_{\max}), are often assumed to be meaningful biological parameters able to describe competitive ability at low nutrient concentrations. Nevertheless, several studies have shown that nutrient uptake rates vary from nutrient limited (faster uptake) to nutrient replete (slower uptake) conditions (Syrett, 1956; Goldman et al., 1981). This suggests that phytoplankton can adapt its resource utilization rate accordingly to alterations in the ambient. Thus, the parameters setting the rate of nutrient uptake (K and V_{\max}) must also vary as a function of the environmental conditions.

Nutrient uptake is an active processes that moves a certain nutrient (ion) from the surrounding environment to inside the cell. This process depends among other factors on the number of uptake sites (n), the area of uptakes sites (A), the handling time (h), and the velocity of transfer or mass transfer coefficient (v). Aksnes

and *Egge (1991)* related some of these factors to K and V_{\max} through a common parameter, α .

$$\alpha = \frac{V_{\max}}{K} = n \cdot A \cdot v \quad (3)$$

Aksnes and Egge (1991) concluded that the application of the Michaelis-Menten model for nutrient uptake (V_n) is a particular case of a more elaborate equation (Eq. 4),

$$V_n = \frac{n \cdot h^{-1} \cdot N}{(A \cdot v \cdot h)^{-1} + N} \quad (4)$$

in which n , A , h and v (and hence K and V_{\max}) are constant. This new formulation was modified by *Pahlow (2005)* in order to include a scheme for the optimal allocation of resources between nutrient uptake and nutrient turnover within the nutrient uptake apparatus. This optimization is achieved by describing α as a function of a maximum nutrient uptake affinity (α_0) and an allocation parameter, f_A , representing the amount of N-quota employed for nutrient uptake and enzyme activity ($1-f_A$).

$$\alpha = \alpha_0 \cdot f_A \quad (5)$$

The optimality-based model of *Pahlow (2005)* combines theoretical derivations of nutrient uptake (*Aksnes and Egge, 1991*) as well as photosynthesis and photoacclimation (*Baumert, 1996*) into an unifying theory where phytoplankton cells maximize their growth rate by optimally allocating their limited nutrient and energy resources among competing metabolic requirements.

Pahlow and Oschlies (2009) extended the formulations of *Pahlow (2005)* in order to include nitrogen and phosphorus colimitation. This new formulation describes the integrated effects of N and P on phytoplankton physiology and growth. A further allocation level, f_V , was later introduced by (*Pahlow et al., 2013*), which optimizes resource utilization between the nutrient acquisition and light harvesting apparatus. f_V varies between 0 (all internal N-quota allocated for nutrient uptake) and 1 (internal N-quota fully allocated for photochemical machinery and enzyme activity). f_V is optimized in order to achieve the maximum possible growth rate under given nutrient and light conditions (Fig. 8). The model of (*Pahlow et al., 2013*) also describes a multiple allocation scheme which includes a partition level that subdivides cellular N used for dissolved inorganic nitrogen (DIN) uptake and N_2 fixation (*Pahlow et al., 2013*) (Fig. 9).

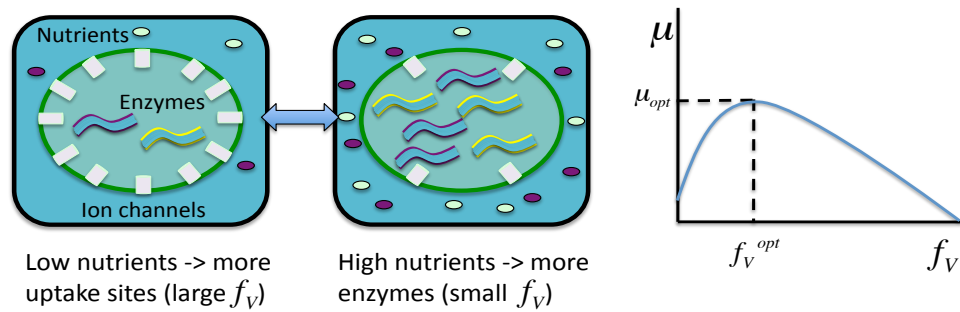


Figure 8: Schematic view of the optimal allocation of resources between nutrient uptake and photochemically-related enzyme activity via f_V , and its effect on μ . μ_{opt} is the maximum growth rate given by the optimization of f_V (f_V^{opt}).

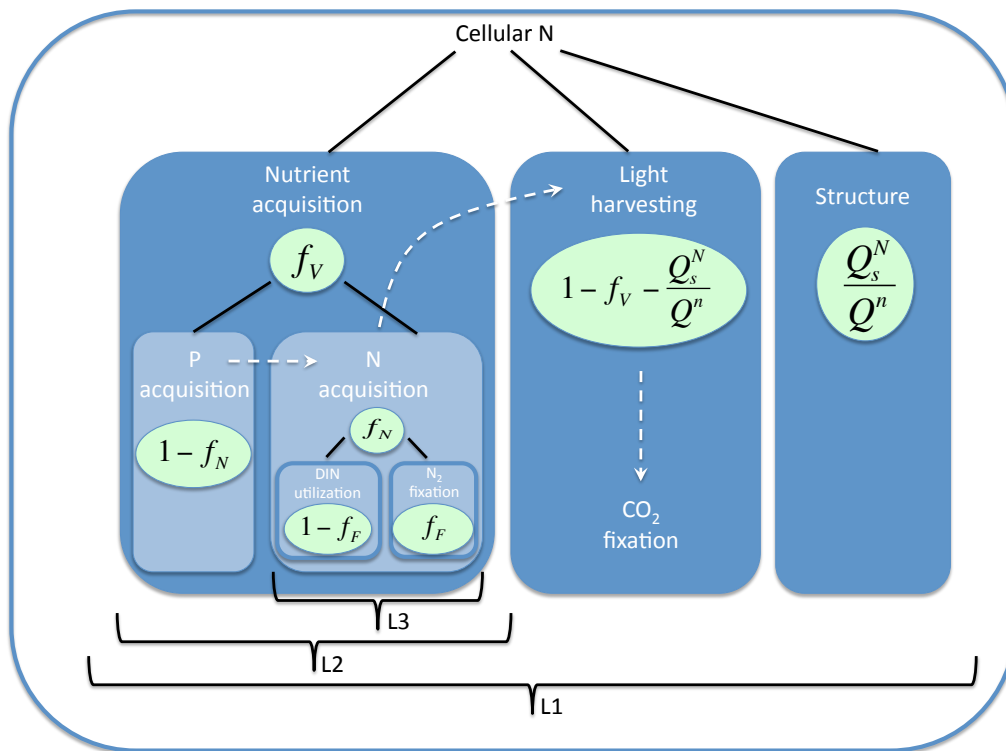


Figure 9: Schematic view of the multiple allocation scheme in the model of *Pahlow et al. (2013)*. Level 1 encompasses the whole cell and divides cellular N into 3 fractions, devoted to nutrient acquisition (f_V), structural protein (Q_s^N/Q^N), and light harvesting ($1 - f_V - Q_s^N/Q^N$). Level 2 partitions nutrient acquisition into P and N-acquisition compartments, described by the allocation factor f_N . Level 3 partitions the N acquisition branch into compartments responsible for dissolved inorganic nitrogen (DIN) uptake and N_2 fixation via allocation factor f_F . Dashed arrows indicate the chain of interactions among P, N, and C acquisition (adapted from *Pahlow et al., 2013*).

1.4 Thesis overview and author contributions

The motivation of this thesis is the understanding of the physiological regulation of phytoplankton growth with the goal to better describe and project biogeochemical cycles affected by phytoplankton stoichiometry. With this aim, the constraints of phytoplankton growth in the global ocean are assessed through a combination of satellite and model-based analysis. Satellite-derived products are used to drive the physiological plankton model, and to obtain new products of major biogeochemical significance. Most of the model analyses described in this thesis were carried out using the optimality-based model of *Pahlow et al. (2013)*. This thesis begins with a novel analysis of nutrient and light colimitation of phytoplankton growth in the global ocean (Chapter 1). Motivated by the results of this study, a method to infer global surface marine nitrate concentrations was developed and evaluated against in situ observations and previous methods (Chapter 2). Chapter 3 merges the results described in the previous chapters in order to estimate global production rates and C biomass of primary producers by allowing physiological acclimation of phytoplankton stoichiometry. A study of processes controlling nitrogen loss in the Pacific Ocean is presented in Chapter 4. This study is based on satellite analyses to estimate production and carbon export and its relation to nitrogen loss in oxygen minimum zones. The thesis ends with a general discussion of the main results obtained and future directions, including an initial examination of the integration of optimality-based formulations in an Earth System Climate model.

Chapter 1. *Global patterns of phytoplankton nutrient and light colimitation inferred from an optimality-based model.* Lionel Arteaga, Markus Pahlow, and Andreas Oschlies. The original idea and experimental design were developed by LA, MP, and AO. Modeling work and data analysis were carried out by LA. The final manuscript was prepared by LA, with comments and corrections from MP and AO. This chapter describes the inference of variable phytoplankton cell-quotas employing an optimality-based model. Cell-quotas are used as a base to calculate nitrogen, phosphorus, and light limitation indices, and obtain global patterns of phytoplankton nutrient and light colimitation. The main results indicate that nitrogen is the major limiting nutrient in the tropical and subtropical ocean, with a secondary co-limiting interaction with phosphorus. Light limitation dominates in high latitudes. Predicted latitudinal patterns of C:P and N:P ratios agree to some extent with observed trends in stoichiometry of particulate organic matter.

Chapter 2. *Global monthly sea surface nitrate fields estimated from remotely sensed sea surface temperature, chlorophyll, and modeled mixed layer depth.* Lionel Arteaga, Markus Pahlow, and Andreas Oschlies.

Original idea was developed by LA. Experimental design was constructed by LA, MP, and AO. Modeling work and data analysis were carried out by LA. The final manuscript was prepared by LA, with comments and corrections from MP and AO. This chapter describes a novel method to estimate surface nitrate fields in the global ocean. Multiple local linear regressions between satellite-inferred Chl, SST and model-derived mixed layer depth (MLD) are employed on a 1° by 1° grid to assess the variability of surface nitrate on a monthly-basis. This method is able to predict nitrate concentrations at four different oceanographic stations distributed in the Atlantic, Pacific and Southern Ocean, based on independent in situ observations. This satellite-based approach can be employed for continuous monitoring of surface ocean nutrient variations.

Chapter 3. *Contribution of phytoplankton to particulate organic carbon in the global ocean.* Lionel Arteaga, Markus Pahlow, and Andreas Oschlies. Original idea was developed by LA. Experimental design was constructed by LA, MP, and AO. Modeling work and data analysis were carried out by LA. The final manuscript was prepared by LA, with comments and corrections from MP and AO. This chapter describes the estimation of global primary production rates employing an optimality-based model of phytoplankton growth and satellite-derived estimates of surface ocean Chl and particulate organic carbon. Global production rates are compared with bio-optical models of PP based on the inference of phytoplankton Chl and C. An assessment of the contribution of phytoplankton to total carbon biomass in the global ocean is presented. Phytoplankton contributes to about 60 % of total POC in low latitudes, and about 15 % in higher latitudes.

Chapter 4. *Nitrogen cycling driven by organic matter export in the South Pacific oxygen minimum zone.* Tim Kalvelage, Gaute Lavik, Phyllis Lam, Sergio Contreras, Lionel Arteaga, Carolin R. Löscher, Andreas Oschlies, Aurelién Paulmier, and Marcel M. M. Kuypers. TK, GL and MMMK. designed the study. TK, GL, SC and AP performed ^{15}N -labelling experiments. TK, GL and PL analysed the data. CRL carried out functional gene analyses. LA and AO modelled export production rates. LS provided CTD and ADCP data. TK, GL, PL and MMMK. wrote the manuscript with input from all co-authors. This chapter describes an analysis of anammox and denitrification rates in the oxygen minimum zone of the South Pacific Ocean. The relation of this study with the overall context of this thesis is the calculation of production and export rates of organic matter with bio-optical and satellite-based algorithms. This work concludes that export rates of organic matter regulate nitrogen loss from oxygen minimum zones.

References

- Aksnes, D. J., and J. K. Egge (1991), A theoretical model for nutrient uptake in phytoplankton, *Marine Ecology Progress Series*, 70, 65–72.
- Antoine, D., J. M. André, and A. Morel (1996), Ocean primary production 2. Estimation at global scale from satellite (Coastal Zone Color Scanner) chlorophyll, *Global Biogeochemical Cycles*, 10(1), 57–69.
- Armstrong, R. (2006), Optimality-based modeling of nitrogen allocation and photoacclimation in photosynthesis, *Deep Sea Research Part II: Topical Studies in Oceanography*, 53(5-7), 513–531, doi: 10.1016/j.dsr2.2006.01.020.
- Baumert, H. (1996), On the theory of photosynthesis and growth in phytoplankton. part I: Light limitation and constant temperature, *Internationale Revue der gesamten Hydrobiologie und Hydrographie*, 81(1), 109–139, doi: 10.1002/iroh.19960810113.
- Behrenfeld, M. J., and P. G. Falkowski (1997a), A consumer’s guide to phytoplankton primary productivity models, *Limnology and Oceanography*, 42(7), 1479–1491, doi: 10.4319/lo.1997.42.7.1479.
- Behrenfeld, M. J., and P. G. Falkowski (1997b), Photosynthetic rates derived from satellite-based chlorophyll concentration, *Limnology and Oceanography*, 42(1), 1–20, doi: 10.4319/lo.1997.42.1.0001.
- Behrenfeld, M. J., A. J. Bale, Z. S. Kolber, J. Aiken, and P. G. Falkowski (1996), Confirmation of iron limitation of phytoplankton in the equatorial Pacific Ocean, *Nature*, 383, 508–511, doi: 10.1038/383508a0.
- Behrenfeld, M. J., J. T. Randerson, C. R. McClain, G. C. Feldman, S. O. Los, C. J. Tucker, P. G. Falkowski, C. B. Field, R. Frouin, W. E. Esaias, D. D. Kolber, and N. H. Pollack (2001), Biospheric primary production during an enso transition, *Science*, 291(5513), 2594–2597, doi: 10.1126/science.1055071.
- Behrenfeld, M. J., E. Boss, D. A. Siegel, and D. M. Shea (2005), Carbon-based ocean productivity and phytoplankton physiology from space, *Global Biogeochemical Cycles*, 19, GB1006, doi:10.1029/2004GB002299.
- Bopp, L., L. Resplandy, J. C. Orr, S. C. Doney, J. P. Dunne, M. Gehlen, P. Halloran, C. Heinze, T. Ilyina, R. Séférian, J. Tjiputra, and M. Vichi (2013), Multiple stressors of ocean ecosystems in the 21st century: projections with cmip5 models, *Biogeosciences*, 10(10), 6225–6245, doi: 10.5194/bg-10-6225-2013.
- Broecker, W. S. (1975), Climatic change: Are we on the brink of a pronounced global warming?, *Science*, 189(4201), 460–463, doi: 10.1126/science.189.4201.460.

- Broecker, W. S., and G. M. Henderson (1998), The sequence of events surrounding termination ii and their implications for the cause of glacial-interglacial CO₂ changes, *Paleoceanography*, *13*(4), 352–364, doi: 10.1029/98PA00920.
- Campbell, J., D. Antoine, R. Armstrong, K. Arrigo, W. Balch, R. Barber, M. Behrenfeld, R. Bidigare, J. Bishop, M.-E. Carr, W. Esaias, P. Falkowski, N. Hoepffner, R. Iverson, D. Kiefer, S. Lohrenz, J. Marra, A. Morel, J. Ryan, V. Vedernikov, K. Waters, C. Yentsch, and J. Yoder (2002), Comparison of algorithms for estimating ocean primary production from surface chlorophyll, temperature, and irradiance, *Global Biogeochemical Cycles*, *16*(3), 9–1–9–15, doi: 10.1029/2001GB001444.
- Canadell, J. G., C. Le Qur, M. R. Raupach, C. B. Field, E. T. Buitenhuis, P. Ciais, T. J. Conway, N. P. Gillett, R. A. Houghton, and G. Marland (2007), Contributions to accelerating atmospheric CO₂ growth from economic activity, carbon intensity, and efficiency of natural sinks, *Proceedings of the National Academy of Sciences*, *104*(47), 18,866–18,870, doi: 10.1073/pnas.0702737104.
- Carr, M., M. Friedrichs, M. Schmeltz, M. Noguchiaita, D. Antoine, K. Arrigo, I. Asanuma, O. Aumont, R. Barber, and M. Behrenfeld (2006), A comparison of global estimates of marine primary production from ocean color, *Deep Sea Research Part II: Topical Studies in Oceanography*, *53*(5-7), 741–770, doi: 10.1016/j.dsr2.2006.01.028.
- Chavez, F. P., M. Messié, and J. T. Pennington (2011), Marine primary production in relation to climate variability and change, *Annual review of marine science*, *3*, 227–260, doi: 10.1146/annurev.marine.010908.163917.
- Ciais, P., C. Sabine, G. Bala, L. Bopp, V. Brovkin, J. Canadell, A. Chhabra, R. DeFriesa, J. Galloway, M. Heimann, C. Jones, C. L. Quere, R. Myneni, S. Piao, and P. Thornton (2013), *Carbon and Other Biogeochemical Cycles*. In, *Climate Change 2013: The Physical Science Basis. Contribution of Working Group I to the Fifth Assessment Report of the Intergovernmental Panel on Climate Change*, Cambridge University Press, Cambridge, United Kingdom and New York, NY, USA.
- Cubasch, U., D. Wuebbles, D. Chen, M. Facchini, D. Frame, N. Mahowald, and J.-G. Winther (2013), *Introduction*. In, *Climate Change 2013: The Physical Science Basis. Contribution of Working Group I to the Fifth Assessment Report of the Intergovernmental Panel on Climate Change*, Cambridge University Press, Cambridge, United Kingdom and New York, NY, USA.

- Droop, M. R. (1973), Some thoughts on nutrient limitation in algae, *Journal of Phycology*, 9(3), 264–272, doi: 10.1111/j.1529-8817.1973.tb04092.x.
- Droop, M. R. (1974), The nutrient status of algal cells in continuous culture, *Journal of the Marine Biological Association of the United Kingdom*, 54, 825–855, doi: 10.1017/S002531540005760X.
- Droop, M. R. (1983), 25 Years of algal growth kinetics a personal view, *Botanica Marina*, XXVI, 99–112, doi: 10.1515/botm.1983.26.3.99.
- Eppley, R. W. (1972), Temperature and phytoplankton growth in the sea, *Fishery Bulletin*, 70(4), 1063–1085.
- Falkowski, P. (1980), Light-shade adaptation in marine phytoplankton, in *Primary Productivity in the Sea, Environmental Science Research*, vol. 19, edited by P. Falkowski, pp. 99–119, Springer US, doi: 10.1007/978-1-4684-3890-1.6.
- Field, C. B. (1998), Primary Production of the Biosphere: Integrating Terrestrial and Oceanic Components, *Science*, 281(5374), 237–240, doi: 10.1126/science.281.5374.237.
- Flynn, K. J. (2010), Do external resource ratios matter?, *Journal of Marine Systems*, 83, 170–180, doi: 10.1016/j.jmarsys.2010.04.007.
- Geider, R., and J. La Roche (2002), Redfield revisited: variability of C:N:P in marine microalgae and its biochemical basis, *European Journal of Phycology*, 37(1), 1–17, doi: 10.1017/S0967026201003456.
- Geider, R. J., T. Platt, and J. Raven (1986), Size dependence of growth and photosynthesis in diatoms: a synthesis, *Marine Ecology Progress Series*, 30, 93–104.
- Geider, R. J., H. L. MacIntyre, and T. Kana (1998), A dynamic regulatory model of phytoplanktonic acclimation to light, nutrients, and temperature, *Limnology and Oceanography*, 43(4), 679–694, doi: 10.4319/lo.1998.43.4.0679.
- Goldman, J., C. Taylor, and P. Glibert (1981), Nonlinear Time-Course Uptake of Carbon and Ammonium by Marine Phytoplankton, *Marine Ecology Progress Series*, 6, 137–148, doi: 10.3354/meps006137.
- Hansell, D., C. Carlson, D. Repeta, and R. Schlitzer (2009), Dissolved Organic Matter in the Ocean: A Controversy Stimulates New Insights, *Oceanography*, 22(4), 202–211, doi: 10.5670/oceanog.2009.109.
- Henson, S. A., R. Sanders, and E. Madsen (2012), Global patterns in efficiency of particulate organic carbon export and transfer to the deep ocean, *Global Biogeochemical Cycles*, 26(1), doi: 10.1029/2011GB004099.

- Klausmeier, C., E. Litchman, T. Daufresne, and S. Levin (2004), Optimal nitrogen-to-phosphorus stoichiometry of phytoplankton, *Nature*, *429*, 171–174, doi: 1.1029/2001GL014649.
- Körtzinger, A., W. Koeve, P. Kähler, and L. Mintrop (2001), C : N ratios in the mixed layer during the productive season in the northeast Atlantic Ocean, *Deep-Sea Research Part I*, *48*(3), 661–688, doi: 10.1016/S0967-0637(00)00051-0.
- Laws, E. A., P. G. Falkowski, W. O. Smith, H. Ducklow, and J. J. McCarthy (2000), Temperature effects on export production in the open ocean, *Global Biogeochemical Cycles*, *14*(4), 1231–1246, doi: 10.1029/1999GB001229.
- Lehninger, A. L. (1971), *Bioenergetics*, Benjaming/Cummings, New York.
- Longhurst, A., S. Sathyendranath, T. Platt, and C. Caverhill (1995), An estimate of global primary production in the ocean from satellite radiometer data, *Journal of Plankton Research*, *17*(6), 1245–1271.
- Martin, J. (1990), Glacial-interglacial CO₂ change: The iron hypothesis, *Paleoceanography*, *5*, 1–13, doi: 10.1029/PA005i001p00001.
- Martin, J., R. M. Gordon, and S. E. Fitzwater (1990), Iron in Antarctic waters, *Nature*, *345*, 156–158, doi:10.1038/345156a0.
- Martin, J. H., G. A. Knauer, D. M. Karl, and W. W. Broenkow (1987), Vertex: carbon cycling in the northeast pacific, *Deep Sea Research Part A. Oceanographic Research Papers*, *34*(2), 267 – 285, doi: [http://dx.doi.org/10.1016/0198-0149\(87\)90086-0](http://dx.doi.org/10.1016/0198-0149(87)90086-0).
- Martiny, A. C., C. T. a. Pham, F. W. Primeau, J. a. Vrugt, J. K. Moore, S. a. Levin, and M. W. Lomas (2013a), Strong latitudinal patterns in the elemental ratios of marine plankton and organic matter, *Nature Geoscience*, *6*, 279–283, doi: 10.1038/ngeo1757.
- Monod, J. (1949), The growth of bacterial cultures, *Annual Review of Microbiology*, *3*(1), 371–394, doi: 10.1146/annurev.mi.03.100149.002103.
- Moore, C. M., M. M. Mills, K. R. Arrigo, I. Berman-Frank, L. Bopp, P. W. Boyd, E. D. Galbraith, R. J. Geider, C. Guieu, S. L. Jaccard, T. D. Jickells, J. La Roche, T. M. Lenton, N. M. Mahowald, E. Marañón, I. Marinov, J. K. Moore, T. Nakatsuka, A. Oschlies, M. A. Saito, T. F. Thingstad, A. Tsuda, and O. Ulloa (2013), Processes and patterns of oceanic nutrient limitation, *Nature Geoscience*, *6*, doi: 10.1038/ngeo1765.

- O'Neill, R., D. DeAngelis, J. Pastor, B. Jackson, and W. Post (1989), Multiple nutrient limitations in ecological models, *Ecological Modelling*, 46(34), 147 – 163, doi: [http://dx.doi.org/10.1016/0304-3800\(89\)90015-X](http://dx.doi.org/10.1016/0304-3800(89)90015-X).
- Orellana, M. V., and M. J. Perry (1992), An immunoprobe to measure Rubisco concentrations and maximal photosynthetic rates of individual phytoplankton cells, *Limnology and Oceanography*, 37(3), 478–490, doi: 10.4319/lo.1992.37.3.0478.
- Pahlow, M. (2005), Linking chlorophyll-nutrient dynamics to the Redfield N:C ratio with a model of optimal phytoplankton growth, *Marine Ecology Progress Series*, 287, 33–43, doi: 10.3354/meps287033.
- Pahlow, M., and A. Oschlies (2009), Chain model of phytoplankton P, N and light colimitation, *Marine Ecology Progress Series*, 376, 69–83, doi: 10.3354/meps07748.
- Pahlow, M., H. Dietze, and A. Oschlies (2013), Optimality-based model of phytoplankton growth and diazotrophy, *Marine Ecology Progress Series*, 489, 1–16, doi: 10.3354/meps10449.
- Platt, T., and A. D. Jassby (1976), The relationship between photosynthesis and light for natural assemblages of coastal marine phytoplankton, *Journal of Phycology*, 12(4), 421–430, doi: 10.1111/j.1529-8817.1976.tb02866.x.
- Quigg, A., Z. V. Finkel, A. J. Irwin, Y. Rosenthal, T.-Y. Ho, J. R. Reinfelder, O. Schofield, F. M. M. Morel, and P. G. Falkowski (2003), The evolutionary inheritance of elemental stoichiometry in marine phytoplankton., *Nature*, 425, 291–294, doi: 10.1038/nature01953.
- Raven, J. a., and P. G. Falkowski (1999), Oceanic sinks for atmospheric CO₂, *Plant, Cell and Environment*, 22(6), 741–755, doi: 10.1046/j.1365-3040.1999.00419.x.
- Redfield, A. (1934), On the proportions of organic derivatives in sea water and their relation to the composition of plankton, *James Johnstone Memorial Volume, University Press of Liverpool*, 176–192.
- Rhee, G.-Y. (1974), Phosphate uptake under nitrate limitation by *scenedesmus* sp. and its ecological implications, *Journal of Phycology*, 10(4), 470–475, doi: 10.1111/j.1529-8817.1974.tb02742.x.
- Sabine, C. L., R. a. Feely, N. Gruber, R. M. Key, K. Lee, J. L. Bullister, R. Wanninkhof, C. S. Wong, D. W. R. Wallace, B. Tilbrook, F. J. Millero, T.-H. Peng, A. Kozyr, T. Ono, and A. F. Rios (2004), The oceanic sink for anthropogenic CO₂, *Science*, 305, 367–71, doi: 10.1126/science.1097403.

- Saito, M. A., T. J. Goepfert, and J. J. Ritt (2008), Some thoughts on the concept of colimitation: Three definitions and the importance of bioavailability, *Limnology and Oceanography*, *53*(1), 276–290.
- Sarmiento, J. L., R. Slater, R. Barber, L. Bopp, S. C. Doney, A. C. Hirst, J. Kleypas, R. Matear, U. Mikolajewicz, P. Monfray, S. V., S. A. Spall, and R. Stouffer (2004), Response of ocean ecosystems to climate warming, *Global Biogeochemical Cycles*, *18*, GB3003, doi:10.1029/2003GB002134.
- Sathyendranath, S., and T. Platt (1989), Computation of aquatic primary production: Extended formalism to include effect of angular and spectral distribution of light, *Limnology and Oceanography*, *34*(1), 188–198, doi: 10.4319/lo.1989.34.1.0188.
- Seigenthaler, U., and J. L. Sarmiento (1993), Atmospheric carbon dioxide in the ocean, *Nature*, *363*, 119–125, doi: 10.1038/365119a0.
- Sigman, D. M., and E. A. Boyle (2000), Glacial/interglacial variations in atmospheric carbon dioxide, *Nature*, *407*(6806), 859–869, doi: 10.1038/35038000.
- Smith, S. L., and Y. Yamanaka (2007), Optimization-based model of multnutrient uptake kinetics, *Limnology and Oceanography*, *52*(4), 1545–1558, doi: 10.4319/lo.2007.52.4.1545.
- Smith, S. L., M. Pahlow, A. Merico, and K. W. Wirtz (2011), Optimality-based modeling of planktonic organisms, *Limnology and Oceanography*, *56*(6), 2080–2094, doi: 10.4319/lo.2011.56.6.2080.
- Sukenik, A., J. Bennett, and P. Falkowski (1987), Light-saturated photosynthesis, limitation by electron transport or carbon fixation?, *Biochimica et Biophysica Acta (BBA) - Bioenergetics*, *891*(3), 205 – 215, doi: [http://dx.doi.org/10.1016/0005-2728\(87\)90216-7](http://dx.doi.org/10.1016/0005-2728(87)90216-7).
- Sundquist, E. T. (1985), *The Carbon Cycle and Atmospheric CO₂: Natural Variations Archean to Present*, 5–59 pp., American Geophysical Union, Washington, DC, USA.
- Sundquist, E. T. (1993), The global carbon dioxide budget, *Science*, *259*(5097), 934–941, doi: 10.1126/science.259.5097.934.
- Syrett, P. J. (1956), The assimilation of ammonia and nitrate by nitrogen-starved cells of *Chlorella vulgaris*, *Physiologia Plantarum*, *9*(1), 19–27, doi: 10.1111/j.1399-3054.1956.tb08988.x.
- Tans, P. P., I. Y. Fung, and T. Takahashi (1990), Observational constraints on the global atmospheric CO₂ budget, *Science*, *247*(4949), 1431–1438, doi: 10.1126/science.247.4949.1431.

Westberry, T., M. J. Behrenfeld, D. A. Siegel, and E. Boss (2008), Carbon-based primary productivity modeling with vertically resolved photoacclimation, *Global Biogeochemical Cycles*, 22, GB2024, doi: 10.1029/2007GB003078.

2 Thesis chapters

2.1 Chapter 1: *Global patterns of phytoplankton nutrient and light colimitation inferred from an optimality-based model.*

Lionel Arteaga, Markus Pahlow, and Andreas Oschlies.

Published article: Arteaga, L., M. Pahlow, and A. Oschlies (2014), Global patterns of phytoplankton nutrient and light colimitation inferred from an optimality-based model, *Global Biogeochemical Cycles*, 28(7), 648–661, doi: 10.1002/2013GB004668



Global Biogeochemical Cycles

RESEARCH ARTICLE

10.1002/2013GB004668

Key Points:

- Description of phytoplankton growth colimitation by nutrients and light
- Prediction of phytoplankton cellular quotas of N, P, and Chl

Correspondence to:

L. Arteaga,
larteaga@geomar.de

Citation:

Arteaga, L., M. Pahlow, and A. Oschlies (2014), Global patterns of phytoplankton nutrient and light colimitation inferred from an optimality-based model, *Global Biogeochem. Cycles*, 28, doi:10.1002/2013GB004668.

Received 5 JUN 2013

Accepted 11 JUN 2014

Accepted article online 13 JUN 2014

Global patterns of phytoplankton nutrient and light colimitation inferred from an optimality-based model

Lionel Arteaga¹, Markus Pahlow¹, and Andreas Oschlies¹

¹GEOMAR Helmholtz Centre for Ocean Research Kiel, Kiel, Germany

Abstract The widely used concept of constant “Redfield” phytoplankton stoichiometry is often applied for estimating which nutrient limits phytoplankton growth in the surface ocean. Culture experiments, in contrast, show strong relations between growth conditions and cellular stoichiometry with often substantial deviations from Redfield stoichiometry. Here we investigate to what extent both views agree by analyzing remote sensing and in situ data with an optimality-based model of nondiazotrophic phytoplankton growth in order to infer seasonally varying patterns of colimitation by light, nitrogen (N), and phosphorus (P) in the global ocean. Our combined model-data analysis suggests strong N and N-P colimitation in the tropical ocean, seasonal light, and N-P colimitation in the Northern Hemisphere, and strong light limitation only during winter in the Southern Ocean. The eastern equatorial Pacific appears as the only ocean area that is essentially not limited by N, P, or light. Even though our optimality-based approach specifically accounts for flexible stoichiometry, inferred patterns of N and P limitation are to some extent consistent with those obtained from an analysis of surface inorganic nutrients with respect to the Redfield N:P ratio. Iron is not part of our analysis, implying that we cannot accurately predict N cell quotas in high-nutrient, low-chlorophyll regions. Elsewhere, we do not expect a major effect of iron on the relative distribution of N, P, and light colimitation areas. The relative importance of N, P, and light in limiting phytoplankton growth diagnosed here by combining observations and an optimal growth model provides a useful constraint for models used to predict future marine biological production under changing environmental conditions.

1. Introduction

Attempts to construct a synthesis of global marine production and its impacts on global biogeochemical cycles often rely on the assumption of constant elemental stoichiometry of phytoplankton (Redfield stoichiometry, [Redfield, 1934]). While convenient and roughly consistent with globally averaged relations inferred from biogeochemical tracer distributions [Fanning, 1992], the assumption of constant elemental stoichiometry is at odds with observed temporal and regional variations of elemental composition of phytoplankton and associated biogeochemical fluxes [Geider and LaRoche, 2002; Körtzinger et al., 2001]. Carbon:nitrogen:phosphorus (C:N:P) ratios are observed to vary widely among different groups of phytoplankton [Quigg et al., 2003; Klausmeier et al., 2004] and in response to nutrient and light limitation [Flynn, 2010; Healey, 1985; Laws and Bannister, 1980].

There is no clear physiological reason why C:N:P ratios of phytoplankton should strictly adhere to any particular stoichiometry (e.g., Redfield stoichiometry, [Geider and LaRoche, 2002]). Although the molar Redfield N:P ratio of 16 is commonly used as a threshold indicating either N or P limitation [Fanning, 1992; Goldman et al., 1979], we are not aware of any direct evidence that a N:P ratio of 16 separates N and P limitation of phytoplankton growth. On the contrary, chemostat experiments suggest that the transition from N to P limitation occurs at N:P supply ratios of about 30 [Rhee, 1978]. This leads to the conclusion that previous methods for inferring N or P limitation in the surface ocean may need to be revised.

The ratio of dissolved inorganic N:P (DIN:DIP) in the ocean (mainly NO_3^- , NH_4^+ , and PO_4^{3-}) results from the balance of nutrient supply from below and differential utilization by phytoplankton and bacteria within the euphotic zone. Shifts in phytoplankton optimal N:P will likely induce alterations in the DIN:DIP ratio [Weber and Deutsch, 2012]. Empirical cell quota models [Droop, 1983] are capable of decoupling C, N, and P, while optimality-based models of phytoplankton growth offer the potential to help understand the interrelations between phytoplankton stoichiometry and primary production in the ocean [Smith et al., 2011]. Recently,

Table 1. Model Parameters Values and Settings for the Sensitivity Experiments

Symbol	Default	Case I	Case II	Description
A_0	0.7	1	0.06	Potential nutrient affinity ($\text{m}^3 \text{mmol C}^{-1} \text{d}^{-1}$)
α	0.7	0.5	3.7	Chl-specific light absorption coefficient ($\text{m}^2 \text{mol C E}^{-1} \text{g Chl}^{-1}$)
Q_0^N	0.046	0.1	0.026	Subsistence N:C (mol N mol C^{-1})
Q_0^P	0.0016	0.0008	0.0027	Subsistence P:C (mol P mol C^{-1})
R_M^{Chl}	0.1	0.1	0.1	Cost of Chl maintenance (d^{-1})
ζ^{Chl}	0.4	0.3	0.6	Cost of photosynthesis coefficient (mol C g Chl^{-1})
ζ^N	0.6	1	0.7	Cost of DIN uptake (mol C mol N^{-1})
V_0^C, V_0^N, V_0^P				Potential C, N, and P acquisition rates dependent on temperature: $1.4 \times 1.066^{\text{TEMP}}$ ($\text{mol C, N, P mol C}^{-1}$)

the behavior of Droop's cell quota model [Droop, 1983] could be related to that of optimality-based models [Pahlow and Oschlies, 2013].

Here we use an optimality-based model of phytoplankton growth [Pahlow *et al.*, 2013] as a mechanistic foundation for the physiological regulation of nutrient acquisition and light harvesting to diagnose N, P, and light limitation, based on field and satellite data of nutrients, light, and temperature in the surface ocean. One aim of this study is to investigate to what extent the results of this combined model-data analysis are consistent with earlier more pragmatic attempts [Fanning, 1992] that infer limiting factors from an analysis of surface DIN:DIP with respect to the Redfield ratio.

2. Methods

In order to estimate N, P, and light colimitation in the global ocean, we calculated the light-limited steady state solution of the optimality-based chain model of Pahlow *et al.* [2013], modified to allow for temperature dependence (see Appendix A). The model was forced with nutrient, light, and temperature data of the surface mixed layer derived from the World Ocean Atlas 2009 (WOA09) database (http://www.nodc.noaa.gov/OC5/WOA09/pr_woa09.html) and satellite observations from the Moderate Resolution Imaging Spectroradiometer (MODIS) (at <http://oceancolor.gsfc.nasa.gov/>), using the Default parameters in Table 1. Temperature, surface nitrate, and phosphate concentrations were obtained as monthly means from WOA09 on a 1° resolution spatial grid. While there are other sources of bioavailable N and P, nitrate and phosphate are the dominant forms and we believe they can serve to describe the general picture of nondiazotrophic phytoplankton growth (co)limitation by N and P in the global ocean. Mixed layer depth (MLD) was defined as the depth at which density exceeds surface density by 0.125 kg m^{-3} [Levitus, 1982]. Density was calculated from global gridded (1°) monthly temperature and salinity data from WOA09.

Light was estimated as “median mixed layer light level” (I_g) [Behrenfeld *et al.*, 2005],

$$I_g = \frac{1}{D} \cdot \text{PAR} \cdot e^{-K_{490} \frac{\text{MLD}}{2}} \quad (1)$$

I_g depends on the day-length-fraction (D , given by the time of the year), surface photosynthetically active radiation (PAR) ($\text{E m}^{-2} \text{d}^{-1}$), the diffusive light attenuation coefficient estimated at 490 nm (K_{490}) (m^{-1}) and MLD (m) [Behrenfeld *et al.*, 2005]. Surface PAR and K_{490} were obtained from MODIS and regridded to a 1° resolution spatial grid. Owing to the saturation of photosynthesis at relatively low light intensities compared to surface PAR, I_g yields a better representation of light limitation of photosynthesis (see S_1 below) than the mean mixed layer light level, which strongly overestimates average mixed layer photosynthesis. The WOA09 compilation represents monthly mean values of data collected over many years, whereas satellite data were obtained as monthly means specifically for the period between January 2005 and December 2010 and averaged into a monthly “climatology” in order to match the temporal resolution of the WOA09 data set.

2.1. Optimality-Based Chain Model

The chain model of Pahlow *et al.* [2013] is a phytoplankton cell quota growth model. The model defines the physiological roles of N and P based on their association with specific functional cellular compartments [Stern *et al.*, 2002], whereby net C fixation (phytoplankton growth) is directly limited by cellular N. N is associated with enzyme activity, thus controlling major cellular metabolic processes and limiting growth

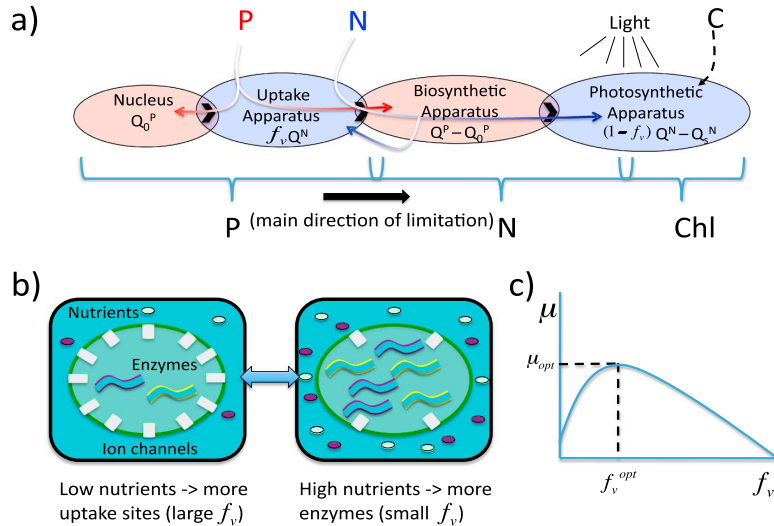


Figure 1. (a) Chain model compartments and associated partial nutrient quotas for N and P: P is associated with the nucleus (Q_0^P) and the biosynthetic apparatus ($Q^P - Q_0^P$). N is associated with the nutrient uptake apparatus ($f_v Q^N$) and the photosynthetic apparatus ($(1 - f_v) Q^N - Q_s^N$). In the model dynamics P limits N acquisition, while N limits Chl synthesis and C fixation. (b) Optimal allocation of N maximizes nutrient (N and P) assimilation: A greater N quota fraction (f_v) is allocated for nutrient acquisition under low extracellular nutrient concentration. Under high-nutrient conditions a greater N fraction is preferentially allocated for carbon fixation. (c) Net cell growth (μ) is maximized via optimization of f_v (see Appendix A for details).

rate via C fixation and light harvesting. In the case of nitrate and nitrite, inorganic N first has to be reduced to ammonium before it is assimilated into protein. N assimilation occurs in the biosynthetic apparatus (ribosomes) and is constrained by P, which is a major component of ribosomes. In this way P limits N acquisition and N limits C fixation [Ågren, 2004]. The model optimizes the allocation of cellular N and energy among requirements for nutrient acquisition and light harvesting to maximize growth rate for the given inorganic nutrient concentrations and light availability (Figure 1) (see Appendix A for details). The present analysis aims to describe N, P, and light (co)limitation of a nondiazotrophic phytoplankton.

2.2. Cell Quota, Nutrient and Light Limitation Estimates

Limitation is here defined as the effect of light and nutrients on phytoplankton growth rate. Nutrient limitation is estimated from phytoplankton cell quotas of N ($Q_N = N:C$) and P ($Q_P = P:C$) in the surface mixed layer as diagnosed from the model and the relative difference with respect to the N and P subsistence quotas Q_0^N and Q_0^P (i.e., the lowest N:C and P:C ratios that the cells can assume in the model (Table 1)). N:C molar ratios can vary from about 0.04 (C:N = 25 mol mol⁻¹) in low nutrient conditions to over 0.2 (C:N = 5 mol mol⁻¹) in nutrient replete conditions [Geider and LaRoche, 2002], while P:C can vary between roughly 0.002 and 0.01 (C:P = 500 and 10 mol mol⁻¹) [Terry et al., 1985; Healey, 1985].

Photosynthetically active radiation is represented here by the median mixed layer light level (I_g , equation (1)). In the model I_g is used as the light intensity reaching the photosynthetic apparatus in the chloroplast. The effect of light limitation is then quantified by the degree of light saturation of the cellular light-harvesting apparatus [S_l , Pahlow, 2005],

$$S_l = 1 - e^{-\frac{\alpha I_g \hat{\theta}^c}{V_0^c}} \quad (2)$$

where α is the light absorption coefficient, V_0^c is the potential C fixation rate, and $\hat{\theta}^c$ is the chlorophyll to carbon ratio of the chloroplast.

In order to obtain a quantitative assessment of nutrient (N and P) and light colimitation, we define limitation indices based on nutrient cell quotas and light saturation. The nutrient limitation index (L_{nutrient})



is defined by the relative difference between actual cell quota Q^{nutrient} and subsistence cell quota Q_0^{nutrient} via

$$L_{\text{nutrient}} = 1 - \frac{Q^{\text{nutrient}} - Q_0^{\text{nutrient}}}{Q^{\text{nutrient}}} = \frac{Q_0^{\text{nutrient}}}{Q^{\text{nutrient}}} \quad (3)$$

with $L_{\text{nutrient}} = 1$ for $Q^{\text{nutrient}} = Q_0^{\text{nutrient}}$ indicating strong limitation and zero growth, and L_{nutrient} declines for large cell quotas under nutrient replete conditions. The light limitation index (L_l) is defined in an analogous manner as one minus the degree of light saturation of the cellular light-harvesting apparatus, i.e.,

$$L_l = 1 - S_l \quad (4)$$

and serves as an indicator of light limitation experienced by the cells in the mixed layer.

2.3. Estimation of the Chlorophyll to Carbon Ratio

The chlorophyll to carbon (Chl:C) ratio combines the effects of nutrient and light limitation driven by the growth requirements of the cell [Cullen and Lewis, 1988]. The Chl:C ratio is regulated to maximize the energy available for N assimilation [Pahlow et al., 2013]. First, the Chl:C ratio of the chloroplast ($\hat{\theta}^c$) is obtained via

$$\hat{\theta}^c = \frac{1}{\zeta^{\text{Chl}}} + \frac{V_0^c}{aI_g} \left\{ 1 - W_0 \left[\left(1 + \frac{R_m^{\text{Chl}}}{DV_0^c} \right) e^{\frac{aI_g}{V_0^c \zeta^{\text{Chl}} + 1}} \right] \right\} \quad \text{if } I_g > I_{g_0} \quad (5)$$

$$\hat{\theta}^c = 0 \quad \text{if } I_g \leq I_{g_0}$$

where ζ^{Chl} is the cost of photosynthesis, R_m^{Chl} is the cost of Chl maintenance, and W_0 is the 0 branch of the Lambert W function, and

$$I_{g_0} = \frac{\zeta^{\text{Chl}} R_m^{\text{Chl}}}{D\alpha} \quad (6)$$

is the threshold irradiance for chlorophyll synthesis.

The Chl:C ratio of the entire cell is then obtained as a direct result of N and light limitation, represented by Q^{N} and $\hat{\theta}^c$, respectively,

$$\text{Chl:C} = \hat{\theta}^c \left(1 - \frac{Q_s^{\text{N}}}{Q^{\text{N}}} - f_v \right) \quad (7)$$

where Q_s^{N} is the partial N quota bound in structural protein, and f_v is the fraction of Q^{N} allocated for nutrient acquisition [Pahlow et al., 2013].

3. Results and Discussion

3.1. Nitrogen and Phosphorus Cell Quota

To be consistent with the literature on biogeochemical fluxes, we report our global model-based results as C:N and C:P ratios. The phytoplankton C:N ratio inferred from our seasonally resolved data model analysis (Figures 2a–2d) shows permanently relatively high values of about 20 mol mol⁻¹ in the subtropical ocean between 40°N and 40°S. The eastern equatorial Pacific, however, shows lower C:N ratios throughout all seasons, of about 10 mol mol⁻¹. High Northern Hemisphere latitudes display stronger seasonal variability, with relatively low C:N (~5 mol mol⁻¹) between January and March. C:N ratios increase in April–June and are highest in July–September approaching values close to 10 mol mol⁻¹ (Figures 2a–2d). In autumn, nitrate concentrations increase and light declines, and phytoplankton C:N ratios at high northern latitudes decrease again during October–December. The Southern Ocean shows much less clear seasonality, with permanently low C:N ratios of around 5 mol mol⁻¹. Overall, there is a clear latitudinal gradient of low to high C:N ratios from high to low latitudes, which is consistent with recent observations [Martiny et al., 2013a].

Patterns of diagnosed phytoplankton C:P ratios also show a clear latitudinal trend with low C:P ratios at high latitudes and high C:P in low latitudes (Figures 2e–2h). Nonetheless, our predicted C:P ratios display also stronger longitudinal variability, with high values in the western North Pacific and particularly the North Atlantic, where the highest C:P is around 450 mol mol⁻¹ during July–September (Figure 2g), reflecting essentially depleted phosphate concentrations in this area [Wu et al., 2000]. The remaining tropical

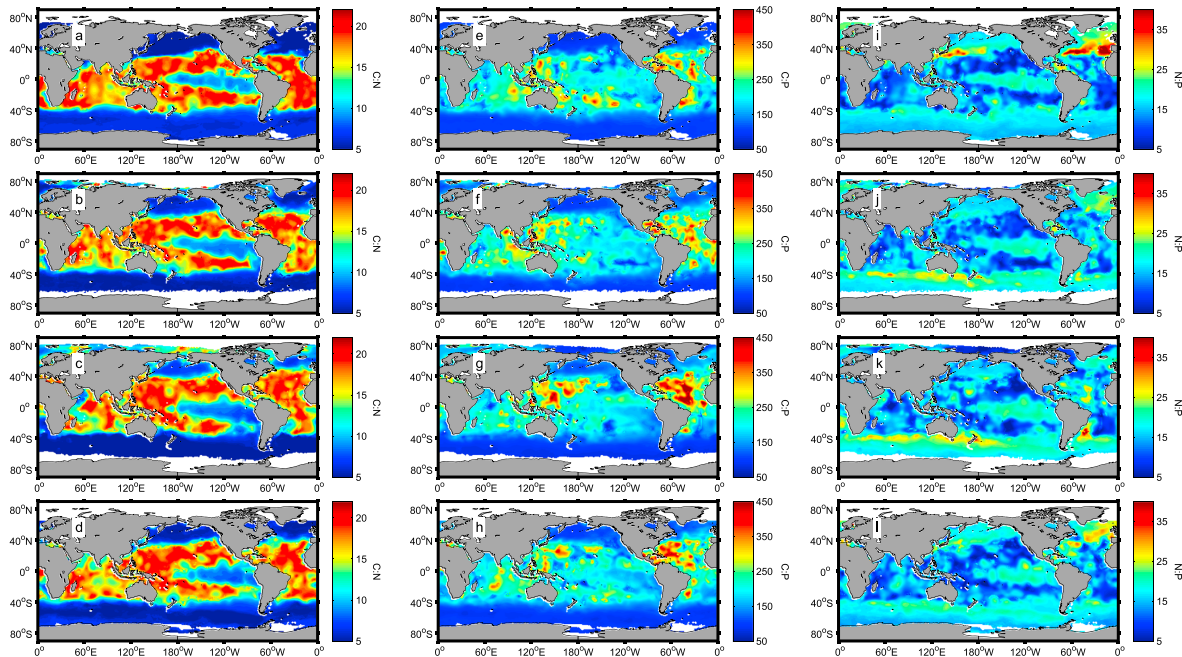


Figure 2. Global patterns of the model-derived phytoplankton cellular (a–d) C:N, (e–h) C:P, and (i–l) N:P ratio (mol mol^{-1}) in the ocean. Each image is a 3 month average composite: (Figures 2a, 2e, and 2i) January–March, (Figures 2b, 2f, and 2j) April–June, (Figures 2c, 2g, and 2k) July–September, and (Figures 2d, 2h, and 2l) October–December.

and subtropical ocean shows C:P ratios of about 200 mol mol^{-1} . Higher latitudes show the lowest C:P of $\sim 100 \text{ mol mol}^{-1}$ (Figures 2e–2h), which is close to the Redfield ratio of 106 mol mol^{-1} .

Figure 3a compares our modeled C:P latitudinal pattern to observations. Black asterisks in Figure 3a show the lognormal average of the observations of particulate organic carbon:particulate organic phosphorus (POC:POP) ratios for each latitudinal band from *Martiny et al.* [2013b]. To make our results more comparable with observations, modeled C:P in Figure 3a are also calculated as lognormal longitudinal averages. There is a close agreement between model and observations, showing low C:P at high latitudes, and vice versa, with the lowest C:P located in southern high latitudes. The agreement in the C:P trend is an encouraging result, as *Martiny et al.* [2013b] indicate that the contribution of living phytoplankton and bacteria to the POP pool in their data set was around 98%, suggesting that the C:P diagnosed from the bulk particulate organic matter (POM) data could be viewed as representative of phytoplankton C:P.

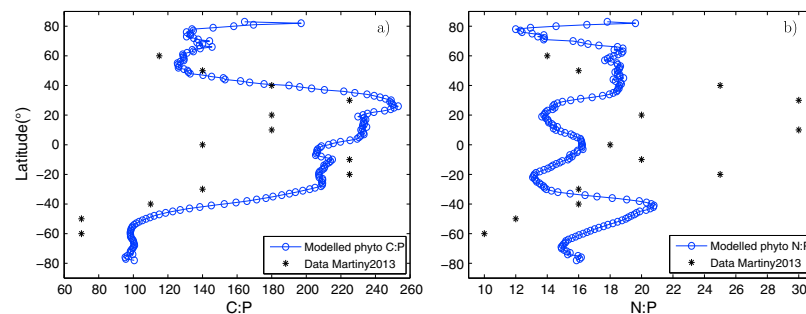


Figure 3. Annual lognormal (a) C:P and (b) N:P latitudinal patterns. Black asterisks show lognormal averages of POC:POP and PON:POP observations for each latitudinal band, presented in Figure 2 of *Martiny et al.* [2013b].

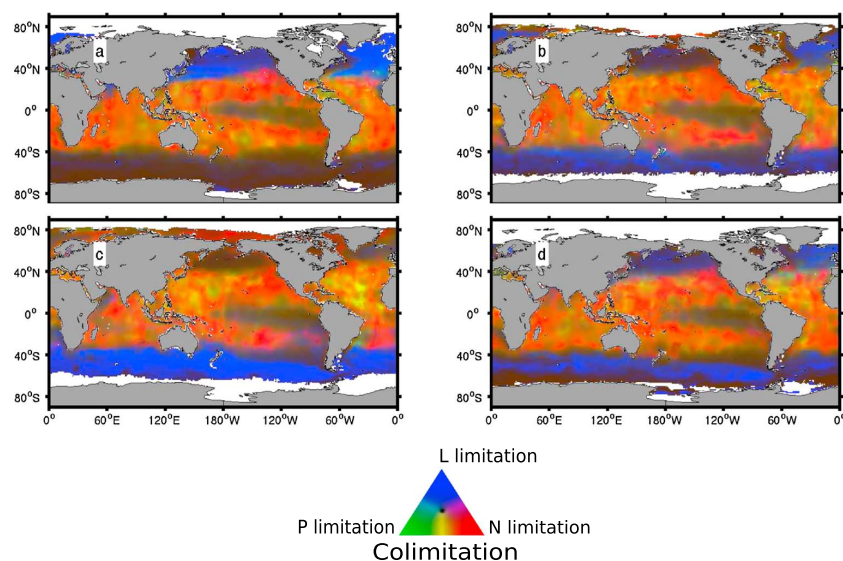


Figure 4. Diagnosed seasonal oceanic N, P, and light colimitation of marine phytoplankton. The maps are red-green-blue (RGB) composites of N limitation (red), P limitation (green), and light (L) limitation (blue). Colimitation is reflected by the combination of colors: purple (N-light colimitation), yellow (N-P colimitation), and cyan (P-light colimitation). Bright colors indicate limitation, whereas dark colors indicate saturation (no limitation). Seasonal images are 3 month average composites: (a) January–March, (b) April–June, (c) July–September, and (d) October–December.

Our simulated N:P ratio (Figures 2i–2l) shows relatively weak seasonal and spatial trends. In general, the lowest N:P are found in oligotrophic areas due to the effect of N limitation, while highest N:P is found in the eastern north Atlantic and western north Pacific, during January–March (Figure 2i). The latitudinal distribution of our modeled N:P (lognormal averages) across all seasons is shown in Figure 3b, together with bulk POM data from *Martiny et al.* [2013b]. Modeled N:P ratios show a rather unclear latitudinal trend when compared with observations, varying between 12 and 22. The lowest longitudinally averaged N:P values are obtained at high latitudes around 80°N (N:P~12), followed by an increase between 60°N and 30°N, and a decrease between 30°N and 30°S, where the phytoplankton N:P stays close to 16 (the Redfield N:P ratio). Between 40°S and 80°S our predicted N:P increases to 22 and decreases again to 16. The POM-derived observations present a much wider range of variation in the N:P ratios, between 10 and 30, with lowest values at high latitudes and vice versa. Our modeled phytoplankton N:P presents some features that are similar to those of *Martiny et al.* [2013b], such as low values in higher northern latitudes, and a slight increase toward lower latitudes. However, the main discrepancy between model and observations is the high N:P values obtained at subtropical regions in PON:POP data, which results in a much clearer low-to-high N:P latitudinal pattern. A possible explanation for this mismatch could be that data on particulate organic matter (POM) might not accurately represent the stoichiometry of phytoplankton, which is what our model analysis describes. In fact, *Martiny et al.* [2013a] analyzed phytoplankton and bulk particulate C:N ratios and found that the phytoplankton C:N was almost twice the bulk value in the western North Atlantic. This implies a relatively low N content of the phytoplankton compared to bulk POM, so that at least part of the N:P discrepancy between our model and the observations of *Martiny et al.* [2013b] might reflect true differences between phytoplankton and bulk POM composition.

Further model development and inclusion of other processes and relevant limiting nutrients in the model physiological dynamics could further reconcile the model and in situ observations. For example, we expect the inclusion of diazotrophy to increase the predicted N:P ratio [*Krauk et al.*, 2006] in midlatitude regions, where nitrogen fixation may be important [*Gruber and Sarmiento*, 1997]. Accounting for other nitrogen sources not represented in the climatology, such as ammonium, could also affect nitrogen uptake [*Dortch*, 1982] in low latitudes and hence phytoplankton N:P ratios. Iron can also limit nitrogen assimilation and

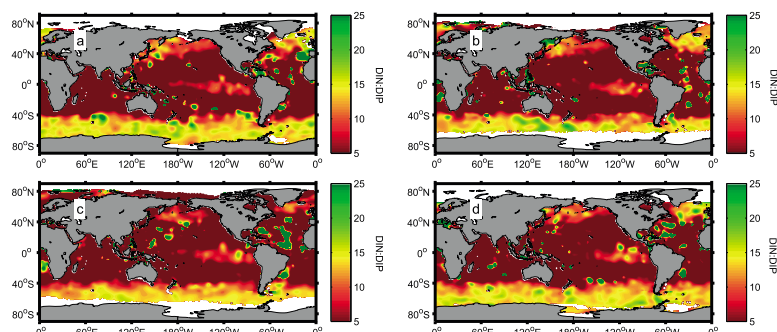


Figure 5. Seasonal oceanic DIN:DIP ratio calculated from WOA09. Each image is a 3 month average composite: (a) January–March, (b) April–June, (c) July–September, and (d) October–December.

carbon fixation, which can potentially alter our predicted cell quotas in high-nutrient, low-chlorophyll (HNLC) regions (see below).

3.2. Light and Nutrient Colimitation

Using L_i together with the N and P limitation indices L_N and L_P diagnosed from the model, we produced seasonal light and nutrient colimitation maps on a $1^\circ \times 1^\circ$ grid for the global ocean (Figure 4). These composite maps of N (red), P (green), and light (blue) (co)limitation identify the roles of each of these factors in controlling phytoplankton growth according to our model. Red and blue areas indicate N and light limitation, respectively, while green areas indicate P limitation. The combination of red and blue (purple areas) indicates nitrogen-light colimitation; red and green (yellow areas) indicates nitrogen-phosphorus colimitation, while green and blue (cyan areas) indicates phosphorus-light colimitation. Brighter colors indicate strong (co)limitation, while dark colors suggest absence of limitation (by either N, P, or light).

The colimitation maps (Figure 4) indicate a dominance of N limitation and N-P colimitation (red and yellow areas respectively) over large parts of the tropical oceans between 40°N and 40°S . Strong N limitation appears over the north and south eastern subtropical Pacific. The Atlantic Ocean, particularly above the equator, shows strong N-P colimitation, which is most severe during the period of July–September (Figure 4c). The eastern equatorial Pacific displays a general lack of limitation, resulting from increased DIN and DIP concentrations due to the equatorial upwelling, which injects nutrients into the surface ocean. The strongest seasonality in limitation patterns is observed at high latitudes, especially over the Pacific Ocean. Here light limitation is present in winter in January–March, followed by generally low light, N, and P limitation in April–June. Nutrient (N-P) colimitation appears in July–September, particularly north of 40°N , while slight light limitation occurs again during October–December.

Contrary to northern latitudes, there is no sign of clear N or P limitation for the Southern Ocean in our colimitation maps. No limitation is observed during the austral summer (January–March), while clear light limitation is present during winter (July–September). Over the periods April–June and October–December, the Southern Ocean appears in general not limited, except for some areas showing exclusive light limitation (Figure 4).

Low C:N and C:P ratios diagnosed for the Southern Ocean (Figure 2) suggest absence of N or P limitation, which is consistent with our expectation for the real ocean for which iron is well established as the primary limiting nutrient in this region [Martin *et al.*, 1990; Boyd *et al.*, 2007]. Light limitation is only clearly evident during austral winter, as expected due to low irradiance and deep mixed layers. Iron regulates the assimilation of nitrate and is an important constituent of the photosynthetic electron transport chain [Geider and LaRoche, 1994]. As iron limitation interferes with the ability of phytoplankton cells to photoacclimate [Greene *et al.*, 1992], and our model does not explicitly account for the effects of iron, the results presented here should actually underestimate true light limitation under iron-limited conditions. Hence, following the idea of a chain of (co)limitations, light could be a strongly limiting factor of phytoplankton growth in this region [Mitchell *et al.*, 1991; Nelson and Smith, 1991] even if iron dynamics are considered.

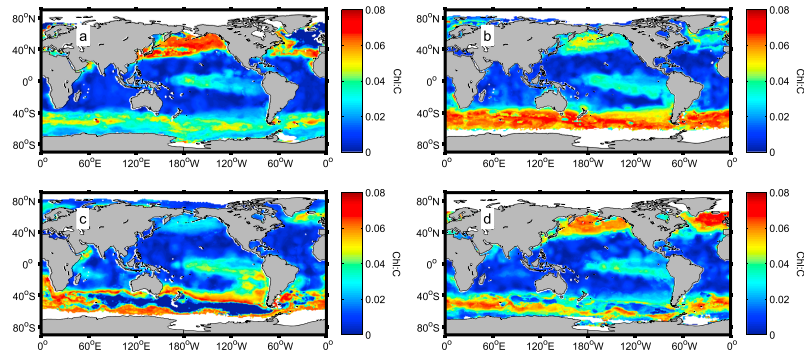


Figure 6. Global patterns of the model-based phytoplankton Chl:C ratio in the ocean. Each image is a 3 month average composite: (a) January–March, (b) April–June, (c) July–September, and (d) October–December.

Another important factor to take into account is the effect of iron on the nitrogen cell quota and thus phytoplankton cellular stoichiometry. As discussed above, the neglect of iron in the current version of the chain model [Pahlow *et al.*, 2013], likely results in an overestimation of the N:P ratio in areas where iron is an important limiting agent of phytoplankton growth, such as the Southern Ocean. Nitrate utilization can be limited by low ambient iron concentrations, as iron compounds serve as co-factors in the reduction from nitrate via nitrite to ammonium [Timmermans *et al.*, 1994]. Hence, we expect that the inclusion of iron in the model cellular dynamics should result in a reduction of the N:P ratio, particularly south of 40°S, where also the lowest N:P ratios are found in the POM data.

The results of our model-derived colimitation analysis can be compared against a traditional analysis of inorganic nutrient ratios in the surface layer. Shown in Figure 5 are seasonal global maps of DIN:DIP ratios extracted from WOA09. The DIN:DIP maps are similar to our colimitation maps in that both show a dominance of N as the main limiting nutrient, particularly in low latitudes. However, while indicating the relative proportion of dissolved N and P in the water, the DIN:DIP ratio does not allow assessing the absolute intensity of the individual nutrient limitation or colimitation. Conversely, our analysis is able to show that P does have a significant importance as a colimiting nutrient for nondiazotrophic phytoplankton, particularly in the Atlantic Ocean. Changes in seasonal colimitation at high latitudes are not evident in the DIN:DIP maps, while our colimitation analysis shows a clear transition from light to N-P colimitation from winter to summer. For the Southern Ocean, both maps suggest neither N nor P limitation (DIN:DIP ~ 16), but our model-based analysis is able to detect strong light limitation during winter. If iron was considered, it would likely turn out as another strong limiting factor in the Southern Ocean. As iron limitation interferes with photoacclimation, we expect that light limitation could be stronger than that shown in Figure 4. Iron limitation also prevents nitrate assimilation, which in turn, should increase C:N ratios and thereby cause N limitation in this region. Consequently, we expect the net effect of iron limitation in terms of our analysis to be enhanced N light colimitation.

Our global patterns generally agree with previous model studies of nutrient limitation in the ocean. Aumont *et al.* [2003] showed that N or P limitation is mainly restricted between 40°N and 40°S for nanophytoplankton and diatoms. However, Aumont *et al.* [2003] cannot differentiate between N and P limitation, thus, a direct comparison with our results is not possible. Moore *et al.* [2002] employed a similar approach based on cellular quotas, but noted that nutrient limitation was difficult to assess during times of strong light limitation due to its effect on cell quotas. This shortcoming is overcome in our analysis by diagnosing the effect of light limitation independently ($1-S_l$, where S_l quantifies the degree of light saturation of the cellular light-harvesting apparatus), and comparing it with N and P limitation. Nevertheless, Moore *et al.* [2002] also find strong N limitation in midocean gyres and substantial P limitation in the north Atlantic and western north Pacific. An important difference between previous model-based nutrient limitation analyses and our model is that most previous models are based on static formulations of the Michaelis-Menten equation applied to different nutrients in order to identify the limiting nutrient. In the chain model used here, colimitation exists in the sense that P availability in the cell directly affects the cell's ability to assimilate N, which in turn limits carbon fixation. Furthermore, and perhaps more relevant in terms of future ocean

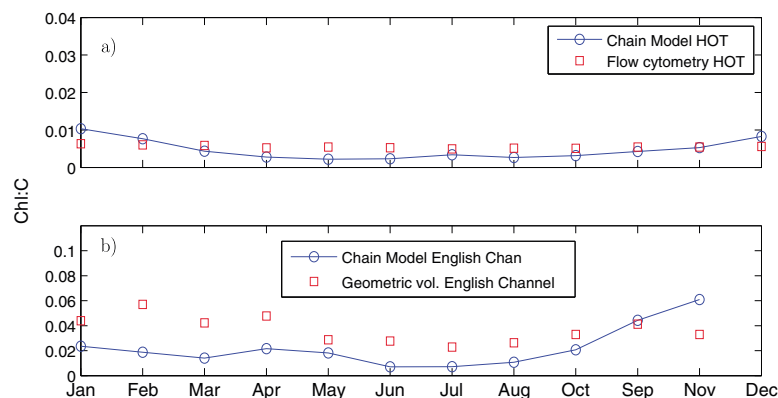


Figure 7. Monthly patterns of phytoplankton Chl:C ratio in the (a) Hawaii Ocean Time series (HOT), and (b) English Channel. Red squares are flow cytometry data for HOT [Winn *et al.*, 1995] scaled to Chl:C [Westberry *et al.*, 2008] and Chl:C estimations from phytoplankton cell volume through cell geometry analysis for the English channel [Llewellyn *et al.*, 2005]. Blue circles connected with lines are model results. Model outputs are obtained using the Default parameter set.

escenarios, our optimality-based approach allows for variable nutrient affinity, which depends on both the intracellular and external nutrient concentration. This permits the representation of more flexible nutrient acquisition dynamics and allows for acclimation of phytoplankton to different environmental conditions.

3.3. Chlorophyll to Carbon Ratio

Our model-based colimitation maps predict N limitation and N-P colimitation in midlatitudes and a seasonal succession of light limitation and N-P colimitation in northern latitudes. The eastern equatorial Pacific and the Southern Ocean show a general absence of limitation, except for the austral winter, where the Southern Ocean appears clearly light limited. Considering N and P limitation, our results are in agreement with recently reviewed experimental evidence [Moore *et al.*, 2013]. These spatial and temporal environmental patterns are also reflected in the modeled chlorophyll to carbon ratio (Chl:C) ratio, which serves as a physiological indicator of phytoplankton (Figure 6). The Chl:C ratio integrates the combined effects of N, P, and light limitation, driven by the requirements of N for CO₂ fixation and Chl for light harvesting. Low light conditions together with high-nutrient concentrations produce the highest Chl:C ratios, as cells photo-acclimate by increasing the Chl cell quota. This is only possible when sufficient nitrogen is available to meet the demand of the enzymatic machinery that processes the energy acquired through light harvesting [Falkowski and Raven, 1997]. Nitrogen is also required in pigment-bound proteins and used for pigment synthesis, which is accounted for in the model as part of the N allocated to the generic light-harvesting compartment. Lowest Chl:C ratios occur when light levels are high, as cells down-regulate the synthesis of Chl, or when low nitrogen concentrations limit Chl synthesis and hence photo-acclimation. Extreme low light conditions, however, will increase the cost of Chl synthesis significantly, resulting in Chl:C ratios = 0 (equation 5). This occurs in our model-based results during winter (July–September) in some areas of the Southern Ocean (Figure 6c), where despite high nutrient availability, light is too low for phytoplankton growth. The range of predicted Chl:C ratios is then the result of a balance between the need and the possibility for photoacclimation as driven by the availability of nutrients and light.

As the chlorophyll to carbon ratio reflects phytoplankton cellular physiology under nutrient and/or light limitation [Geider *et al.*, 1998], we evaluate our model-based results against available observations of seasonal Chl:C variations. We chose Chl:C ratios to validate our results because it appears to be more directly linked to phytoplankton growth than other cellular ratios (e.g., N:P) [Terry *et al.*, 1983, 1985]. Also, observations on Chl:C found in the literature are more directly related to phytoplankton cellular components and not total POM, as is often the case for N:P measurements. Data were obtained from fluorescence measurements at the Hawaii Ocean Time series (HOT) [Winn *et al.*, 1995], scaled to Chl:C [Westberry *et al.*, 2008] and cell volumes estimated from cell geometry in the English Channel [Llewellyn *et al.*, 2005]. At both sites, the temporal evolution of the observed Chl:C ratios can be reproduced reasonably well, although the model slightly underestimates the Chl:C at the English Channel location, particularly during the first months of the

Table 2. Model Symbols in Appendix A

Symbol	Description
f_N	Fraction of $f_V Q^N$ allocated for N
f_V	Fraction of Q^N allocated for nutrient acquisition
I_g	Median mixed layer light level ($E\ m^{-2}\ d^{-1}$)
μ	Net growth rate (d^{-1})
PAR	Photosynthetically active radiation ($E\ m^{-2}\ d^{-1}$)
Q^N	N:C ratio ($mol\ N\ mol\ C^{-1}$)
Q_s^N	Partial N quota bound in structural protein ($mol\ N\ mol\ C^{-1}$)
R	Respiration (d^{-1})
R^{Chl}	Cost of photosynthesis (d^{-1})
S_l	Light saturation
TEMP	Temperature ($^{\circ}C$)
V^C	C fixation rate ($mol\ C\ mol\ C^{-1}\ d^{-1}$)
V^N	N assimilation rate ($mol\ N\ mol\ C^{-1}\ d^{-1}$)
V^P	P assimilation rate ($mol\ P\ mol\ C^{-1}\ d^{-1}$)
V_0^C	Potential C fixation rate ($mol\ C\ mol\ C^{-1}\ d^{-1}$)
V_0^N	Local potential N assimilation rate ($mol\ N\ mol\ C^{-1}\ d^{-1}$)
V_0^P	Local potential P assimilation rate ($mol\ P\ mol\ C^{-1}\ d^{-1}$)
ζ^N	Cost of DIN uptake ($mol\ C\ mol\ N^{-1}$)

year (Figure 7). The parameter set used for this validation exercise is the same as for all the modeled cell quotas and limitation indices outputs presented above (parameter set "Default," Table 1).

3.4. Model Sensitivity

All model results presented here have been obtained from the chain model using the Default parameters in Table 1. In order to examine the sensitivity of our model predictions to different parameter settings, model outputs were also obtained for two additional parameter sets, Case I and Case II, which were selected to cover much of the range of parameters in Table 2 of *Pahlow et al.* [2013]. For these sensitivity experiments a regional breakdown of the results similar to that of *Behrenfeld et al.* [2005] was used. Monthly model outputs were produced for different regions of the global ocean, characterized by five variance levels based on standard deviations of seasonal Chl, calculated from Chl satellite data ($mg\ m^{-3}$) obtained from MODIS (<http://oceancolor.gsfc.nasa.gov/>), from January 2005 to December 2010 (Figure 8). The variance levels are defined as: $L_0 = 0 < SD_{Chl} < 0.004\ mg\ Chl\ m^{-3}$, $L_1 = 0.004 < SD_{Chl} < 0.007\ mg\ Chl\ m^{-3}$, $L_2 = 0.007 <$

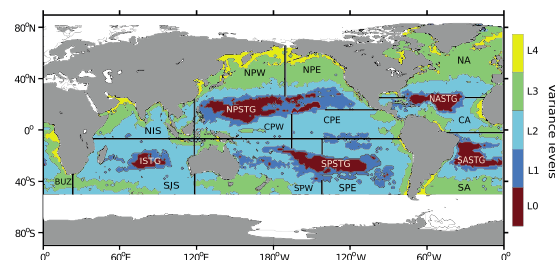


Figure 8. Map of 17 areas of the global ocean divided according to their geographical position. The resulting areas were subdivided based on their seasonal variability of surface Chl (levels L0 to L4), estimated from the satellite sensor MODIS (<http://oceancolor.gsfc.nasa.gov/>) between 2005 and 2010. The subdivision of the 17 geographical areas produced 12 areas of high Chl variability that only have Chl variance levels L2, L3, and L4: North Pacific West (NPW), North Pacific East (NPE), Central Pacific West (CPW), Central Pacific East (CPE), South Pacific West (SPW), South Pacific East (SPE), North Atlantic (NA), Central Atlantic (CA), South Atlantic (SA), Benguela Upwelling Zone (BUZ), North Indian Sea (NIS), and South Indian Sea (SIS); and five areas of low Chl variability that only have levels L0 and L1: North Pacific Sub-Tropical Gyre (NPSTG), South Pacific Sub-Tropical Gyre (SPSTG), North Atlantic Sub-Tropical Gyre (NASTG), South Atlantic Sub-Tropical Gyre (SASTG), and Indian Subtropical Gyre (ISTG).

$SD_{Chl} < 0.03\ mg\ Chl\ m^{-3}$, $L_3 = 0.03 < SD_{Chl} < 0.3\ mg\ Chl\ m^{-3}$, $L_4 = SD_{Chl} > 0.3\ mg\ Chl\ m^{-3}$. The precise cutoff values of these regions are not critical and were simply chosen to yield regions consistent with large-scale ocean circulation and pigment features [*Behrenfeld et al.*, 2005].

Figure 9 contrasts differences between the three parameter sets Default (blue), Case I (red), and Case II (green) with differences between geographical areas for Chl:C, L_N , L_P , and L_I . Figures 9a–9d show two selected areas of the Atlantic Ocean (L3-North Atlantic and L0-North Atlantic Sub-Tropical Gyre), while Figures 9e–9h present two selected areas of the Pacific Ocean (L3-North Pacific East and L2-Central Pacific East). Differences between model results obtained with the distinct

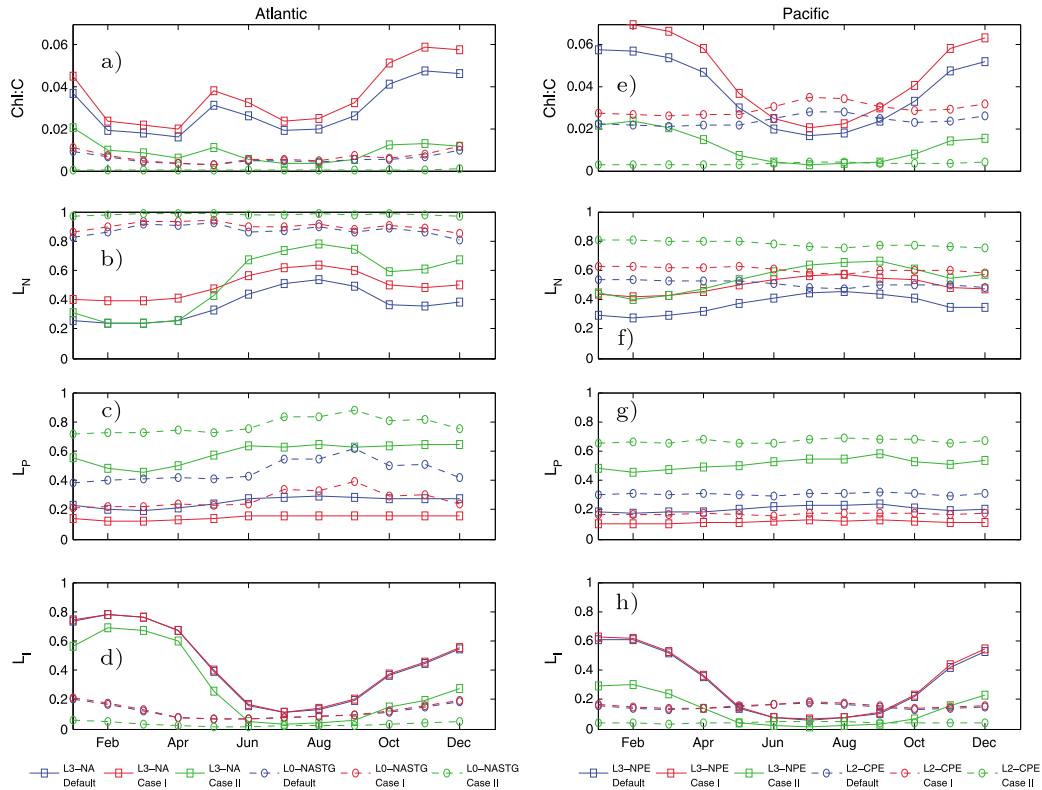


Figure 9. Model sensitivity experiments for parameter settings "Default" (blue), "Case I" (red), and "Case II" (green). Plotted oceanic areas in the Atlantic ocean (a–d): L3-North Atlantic (squares and continuous line) and L0-North Atlantic Sub-Tropical Gyre (circles and dashed line). Plotted oceanic areas in the Pacific ocean (e–h): L3-North Pacific East (squares and continuous line) and L2-Central Pacific East (circles and dashed line). Chl:C (Figures 9a and 9e) is the chlorophyll to carbon ratio of phytoplankton. (Figures 9b and 9f) L_N , (Figures 9c and 9g) L_P , and (Figures 9d and 9h) L_I are the nitrogen, phosphorus, and light limitation indices, respectively.

parameter sets are generally smaller than differences between geographical regions in each model simulation. For the Chl:C ratio, lower values are obtained for the Case II simulation due to a higher carbon cost for photosynthesis (ζ^{Chl}) and a significantly higher light absorption coefficient (α). L_N shows relatively small differences between runs. Case II presents overall the highest N limitation due to a significantly lower nutrient affinity (A_0) with respect to Case I and Default. For L_P , Case II appears again as the most limited simulation, as a result of the combination of a low A_0 and the highest phosphorus subsistence quota (Q_P^0) of all three simulations. Stronger light limitation is found in the Default and Case I simulations due to lower light absorption coefficients (α), which reduce the phytoplankton efficiency of C assimilation. In general, changes in the parameters mostly affect the magnitude of the limitation indices and Chl:C ratio, but not the seasonal trend of the results. The model's seasonal behavior is in all cases determined by the variability of the forcing (nutrient and light) data. Overall spatial patterns of nutrient and light colimitation remain unaltered regardless of which set of parameters is used.

4. Conclusions

Our combined model-data analysis suggests strong N limitation and N-P colimitation in the tropical and subtropical ocean, and seasonal light limitation and N-P colimitation in Northern Hemisphere high latitudes. The eastern equatorial Pacific shows an overall lack of limitation by either N, P, or light, while the Southern Ocean appears strongly light limited during winter. Our colimitation analysis is able to describe the combined effects of N, P, and light (co)limitation, which cannot be achieved with a traditional inspection of

DIN:DIP ratios. However, our model-based results yield to some extent similar patterns as limitation estimates inferred from oceanic DIN:DIP ratios with respect to the Redfield ratio. This comes as a surprising result, given that our mechanistic model allows for flexible rather than Redfield phytoplankton stoichiometry. There is no clear reason why optimality-derived cell quotas should approach the Redfield N:P ratio (~ 16). However, while our predicted N:P varies widely globally (around 5 to 40 mol mol⁻¹), a pointwise average among all seasons of our predicted phytoplankton N:P ratios yields a global N:P of 16. This could suggest that although optimality-derived individual phytoplankton cell quotas do not approach any particular common stoichiometry, the present distribution of available dissolved N and P in the surface ocean induces the optimality-derived N:P ratio of global phytoplankton to have a mean value close to Redfield stoichiometry.

A shortcoming of our current model is the neglect of iron limitation. Including iron dynamics in our analysis could have an important effect on N:P ratios in HNLC regions such as the Southern Ocean. Currently we are not aware of experimental data suitable for including iron (co)limitation in our optimality-based model concept. Apart from these HNLC regions, we believe that the neglect of iron limitation should not induce major changes in the relative distribution of N, P, and light colimitation areas, as these are estimated from cell quotas relative to phytoplankton biomass (and not from N:P ratios). The relative importance of N, P, and light in limiting phytoplankton growth diagnosed here by combining observations and an optimal-growth model, thus provides a useful constraint on models used to predict future marine biological production under changing environmental conditions.

Appendix A: Supplementary Material

S.1 Overview of the Chain Model

In the optimality-based phytoplankton growth model of *Pahlow et al.* [2013], growth (μ) is described as the difference between C fixation (V^c) and respiration (R),

$$\mu = V^c - R \quad (S.1)$$

V^c is a function of N cell quota (Q^N), the potential CO₂ fixation rate (V_0^c), and PAR. PAR in this work is used to quantify I_g (equation (1)). The effect of light limitation is then estimated by the degree of light saturation of the cellular light-harvesting apparatus, S_1 (equation (2)). The C-fixation rate is then defined as,

$$V^c = V_0^c \left(1 - \frac{Q_s^N}{Q^N} - f_V \right) S_1 \quad (S.2)$$

where f_V is the fraction of cellular N allocated for nutrient acquisition, and Q_s^N represents cellular N bound in structural protein. Respiration comprises the cost of photosynthesis (R^{chl}) and the cost of N assimilation ($\zeta^N V^N$) assumed to be proportional to N assimilation (V^N),

$$R = \zeta^N V^N + R^{chl} \quad (S.3)$$

N allocated for nutrient acquisition ($f_V Q^N$) is further divided between DIN and DIP acquisition via another allocation factor (f_N):

$$V^N = f_V f_N V_*^N \quad V^P = f_V (1 - f_N) V_*^P \quad (S.4)$$

where V_*^N and V_*^P are potential rates of N and P uptake as functions of potential uptake rates, V_0^N , V_0^P , and affinity, A_0 .

The allocation factors f_V and f_N are calculated to maximize net balanced growth rate.

S.2 Temperature Dependence

Since the original model [Pahlow *et al.*, 2013] does not include temperature, we introduced a temperature dependence [Eppley, 1972] of the maximum rate parameters as follows:

$$V_0^C \cdot V_0^N \cdot V_0^P = 1.4 * 1.066^{\text{TEMP}}$$

Acknowledgments

We wish to thank M. Behrenfeld and R. O'Malley for sharing their expertise and providing helpful insights on satellite inputs and the computation of the median mixed layer light level (I_g). The research leading to these results has received funding from the European Community's Seventh Framework Programme FP7/2007-2013, Space Theme, under grant agreement 282723 (OSS2015). This work is also a contribution of the Sonderforschungsbereich 754 "Biogeochemistry Interactions in the Tropical Ocean" (www.sfb754.de).

References

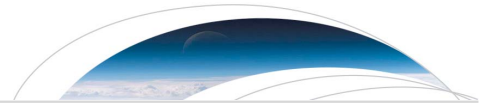
- Ågren, G. I. (2004), The C:N:P stoichiometry of autotrophs—Theory and observations, *Ecol. Lett.*, *7*, 185–191, doi:10.1111/j.1461-0248.2004.00567.x.
- Aumont, O., E. Maier-Reimer, S. Blain, and P. Monfray (2003), An ecosystem model of the global ocean including Fe, Si, P colimitations, *Global Biogeochem. Cycles*, *17*(2), 1060, doi:10.1029/2001GB001745.
- Behrenfeld, M. J., E. Boss, D. A. Siegel, and D. M. Shea (2005), Carbon-based ocean productivity and phytoplankton physiology from space, *Global Biogeochem. Cycles*, *19*, GB1006, doi:10.1029/2004GB002299.
- Boyd, P. W., et al. (2007), Mesoscale iron enrichment experiments 1993–2005: Synthesis and future directions, *Science*, *315*, 612–617, doi:10.1126/science.1131669.
- Cullen, J., and M. Lewis (1988), The kinetics of algal photoadaptation in the context of vertical mixing, *J. Plankton Res.*, *10*(5), 1039–1063.
- Dortch, Q. (1982), The interaction between ammonium and nitrate uptake in phytoplankton, *Mar. Ecol. Prog. Ser.*, *61*, 183–201.
- Droop, M. R. (1983), 25 Years of algal growth kinetics: A personal view, *Bot. Mar.*, *26*, 99–112.
- Eppley, R. W. (1972), Temperature and phytoplankton growth in the sea, *Fish. Bull.*, *70*(4), 1063–1085.
- Falkowski, P. G., and J. Raven (1997), *Aquatic Photosynthesis*, Blackwell Science Ltd., Oxford, U. K.
- Fanning, K. A. (1992), Nutrient provinces in the sea: Concentration ratios, reaction rate ratios, and ideal covariation, *J. Geophys. Res.*, *97*(C4), 5693–5712.
- Flynn, K. J. (2010), Do external resource ratios matter?, *J. Mar. Syst.*, *83*, 170–180, doi:10.1016/j.jmarsys.2010.04.007.
- Geider, R. J., and J. LaRoche (1994), The role of iron in phytoplankton photosynthesis, and the potential for iron-limitation of primary productivity in the sea, *Photosynth. Res.*, *39*, 275–301.
- Geider, R. J., and J. LaRoche (2002), Redfield revisited: Variability of C:N:P in marine microalgae and its biochemical basis, *Eur. J. Phycol.*, *37*, 1–17.
- Geider, R. J., H. L. MacIntyre, and T. Kana (1998), A dynamic regulatory model of phytoplankton acclimation to light, nutrients, and temperature, *Limnol. Oceanogr.*, *43*, 679–694.
- Goldman, J., J. McCarthy, and D. Peavey (1979), Growth rate influence on the chemical composition of phytoplankton in oceanic waters, *Nature*, *279*, 210–215.
- Greene, R. M., R. J. Geider, Z. Kolber, and P. G. Falkowski (1992), Iron-induced changes in light harvesting and photochemical energy conversion processes in eukaryotic marine algae, *Plant Physiol.*, *100*, 565–75.
- Gruber, N., and J. L. Sarmiento (1997), Global patterns of marine nitrogen fixation and denitrification, *Global Biogeochem. Cycles*, *11*(2), 235–266.
- Healey, F. P. (1985), Interacting effects of light and nutrient limitation on the growth rate of *Synechococcus linearis* (cyanophyceae), *J. Phycol.*, *21*, 134–146.
- Klausmeier, C., E. Litchman, T. Daufresne, and S. Levin (2004), Optimal nitrogen-to-phosphorus stoichiometry of phytoplankton, *Nature*, *429*, 171–174, doi:10.1029/2001GL014649.
- Körtzinger, A., W. Koeve, P. Kähler, and L. Mintrop (2001), C:N ratios in the mixed layer during the productive season in the northeast Atlantic Ocean, *Deep Sea Res. Part I*, *48*, 661–688.
- Krauk, J. M., T. A. Villareal, J. A. Sohm, J. P. Montoya, and D. G. Capone (2006), Plasticity of N:P ratios in laboratory and field populations of *Trichodesmium* spp, *Aquat. Microb. Ecol.*, *42*, 243–253.
- Laws, E. A., and T. T. Bannister (1980), Nutrient and light limited growth of *Thalassiosira fluviatilis* in continuous culture, with implications for phytoplankton growth in the ocean, *Limnol. Oceanogr.*, *25*, 457–473.
- Levitus, S. (1982), Climatological atlas of the world ocean, *NOAA Professional Paper 13*, U.S. Government Printing Office, Washington, D. C.
- Llewellyn, C. A., J. R. Fishwick, and J. C. Blackford (2005), Phytoplankton community assemblage in the English Channel: A comparison using chlorophyll a derived from HPLC-CHEMTAX and carbon derived from microscopy cell counts, *J. Plankton Res.*, *27*(1), 103–119, doi:10.1093/plankt/fbh158.
- Martin, J., R. M. Gordon, and S. E. Fitzwater (1990), Iron in Antarctic waters, *Nature*, *345*, 156–158, doi:10.1038/345156a0.
- Martiny, A. C., J. A. Vrugt, F. W. Primeau, and M. W. Lomas (2013a), Regional variation in the particulate organic carbon to nitrogen ratio in the surface ocean, *Global Biogeochem. Cycles*, *27*(3), 723–731, doi:10.1002/gbc.20061.
- Martiny, A. C., C. T. A. Pham, F. W. Primeau, J. A. Vrugt, J. K. Moore, S. A. Levin, and M. W. Lomas (2013b), Strong latitudinal patterns in the elemental ratios of marine plankton and organic matter, *Nat. Geosci.*, *6*, 279–283, doi:10.1038/ngeo1757.
- Mitchell, B. G., E. A. Brody, O. Holm-Hansen, C. McClain, and J. Bishop (1991), Light limitation of phytoplankton biomass and macronutrient utilization in the Southern Ocean, *Limnol. Oceanogr.*, *36*(8), 1662–1677.
- Moore, C. M., et al. (2013), Processes and patterns of oceanic nutrient limitation, *Nat. Geosci.*, *6*, 701–710, doi:10.1038/ngeo1765.
- Moore, J. K., S. C. Doney, D. M. Glover, and I. Y. Fung (2002), Iron cycling and nutrient-limitation patterns in surface waters of the World Ocean, *Deep Sea Res. Part II*, *49*, 463–507.
- Nelson, D. M., and W. Smith (1991), Sverdrup revisited: Critical depths, maximum chlorophyll levels, and the control of Southern Ocean productivity by the irradiance-mixing regime, *Limnol. Oceanogr.*, *36*(8), 1650–1661.
- Pahlow, M. (2005), Linking chlorophyll-nutrient dynamics to the Redfield N:C ratio with a model of optimal phytoplankton growth, *Mar. Ecol. Prog. Ser.*, *287*, 33–43.
- Pahlow, M., and A. Oschlies (2013), Optimal allocation backs Droop's cell-quota model, *Mar. Ecol. Prog. Ser.*, *473*, 1–5, doi:10.3354/meps10181.
- Pahlow, M., H. Dietze, and A. Oschlies (2013), Optimality-based model of phytoplankton growth and diazotrophy, *Mar. Ecol. Prog. Ser.*, *489*, 1–16, doi:10.3354/meps10449.
- Quigg, A., Z. V. Finkel, A. J. Irwin, Y. Rosenthal, T.-Y. Ho, J. R. Reinfelder, O. Schofield, F. M. M. Morel, and P. G. Falkowski (2003), The evolutionary inheritance of elemental stoichiometry in marine phytoplankton, *Nature*, *425*, 291–294, doi:10.1038/nature01953.

- Redfield, A. (1934), On the proportions of organic derivatives in sea water and their relation to the composition of plankton, in *James Johnstone Memorial Volume*, edited by R. Daniel, pp. 176–192, Univ. Press of Liverpool, Cambridge, U. K.
- Rhee, G. (1978), Effects of N:P atomic ratios and nitrate limitation on algal growth, cell composition, and nitrate uptake, *Limnol. Oceanogr.*, *23*(1), 10–25.
- Smith, S. L., M. Pahlow, A. Merico, and K. W. Wirtz (2011), Optimality-based modeling of planktonic organisms, *Limnol. Oceanogr.*, *56*(6), 2080–2094, doi:10.4319/lo.2011.56.6.2080.
- Sterner, R. W., and J. J. Elser (2002), *Ecological stoichiometry: The biology of elements from molecules to the biosphere*, Princeton Univ. Press, Princeton, N. J.
- Terry, K., J. Hirata, and E. Laws (1983), Light limited growth of two marine strains of the marine diatom *Phaeodactylum tricornutum* Bohlin: Chemical composition, carbon partitioning, and the diel periodicity of physiological processes, *J. Exp. Mar. Biol. Ecol.*, *68*, 209–227.
- Terry, K., J. Hirata, and E. Laws (1985), Light-, nitrogen-, and phosphorus-limited growth of *Phaeodactylum tricornutum* Bohlin strain tfx-1: Chemical composition, carbon partitioning, and the diel periodicity of physiological processes, *J. Exp. Mar. Biol. Ecol.*, *86*, 85–100.
- Timmermans, K., W. Stolte, and H. Baar (1994), Iron-mediated effects on nitrate reductase in marine phytoplankton, *Mar. Biol.*, *121*, 389–396.
- Weber, T., and C. Deutsch (2012), Oceanic nitrogen reservoir regulated by plankton diversity and ocean circulation, *Nature*, *489*, 419–22, doi:10.1038/nature11357.
- Westberry, T., M. J. Behrenfeld, D. A. Siegel, and E. Boss (2008), Carbon-based primary productivity modeling with vertically resolved photoacclimation, *Global Biogeochem. Cycles*, *22*, GB2024, doi:10.1029/2007GB003078.
- Winn, C. D., L. Campbell, J. R. Christian, R. M. Letelier, D. V. Hebel, J. E. Dore, L. Fujieki, and D. M. Karl (1995), Seasonal variability in the phytoplankton community of the North Pacific Subtropical Gyre, *Global Biogeochem. Cycles*, *9*, 605–620, doi:10.1029/95GB02149.
- Wu, J., W. Sunda, E. A. Boyle, and D. M. Karl (2000), Phosphate depletion in the North Atlantic Ocean, *Science*, *289*, 759–762, doi:10.1126/science.289.5480.759.

2.2 Chapter 2: *Global monthly sea surface nitrate fields estimated from remotely sensed sea surface temperature, chlorophyll, and modeled mixed layer depth.*

Lionel Arteaga, Markus Pahlow, and Andreas Oschlies.

Published article: Arteaga, L., M. Pahlow, and A. Oschlies (2015), Global monthly sea-surface nitrate fields estimated from remotely sensed sea-surface temperature, chlorophyll, and modelled mixed layer depth, *Geophysical Research Letters*, doi: 10.1002/2014GL062937



Geophysical Research Letters

RESEARCH LETTER

10.1002/2014GL062937

Key Point:

- Global estimation of oceanic nitrate variability through SST, Chl, and MLD

Supporting Information:

- Readme
- Data Set S1
- Figure S1

Correspondence to:

L. Arteaga,
larteaga@geomar.de

Citation:

Arteaga, L., M. Pahlow, and A. Oschlies (2015), Global monthly sea surface nitrate fields estimated from remotely sensed sea surface temperature, chlorophyll, and modeled mixed layer depth, *Geophys. Res. Lett.*, *42*, doi:10.1002/2014GL062937.

Received 19 DEC 2014

Accepted 12 JAN 2015

Accepted article online 16 JAN 2015

Global monthly sea surface nitrate fields estimated from remotely sensed sea surface temperature, chlorophyll, and modeled mixed layer depth

Lionel Arteaga¹, Markus Pahlow¹, and Andreas Oschlies¹

¹GEOMAR Helmholtz Centre for Ocean Research Kiel, Kiel, Germany

Abstract Information about oceanic nitrate is crucial for making inferences about marine biological production and the efficiency of the biological carbon pump. While there are no optical properties that allow direct estimation of inorganic nitrogen, its correlation with other biogeochemical variables may permit its inference from satellite data. Here we report a new method for estimating monthly mean surface nitrate concentrations employing local multiple linear regressions on a global 1° by 1° resolution grid, using satellite-derived sea surface temperature, chlorophyll, and modeled mixed layer depth. Our method is able to reproduce the interannual variability of independent in situ nitrate observations at the Bermuda Atlantic Time Series, the Hawaii Ocean Time series, the California coast, and the southern New Zealand region. Our new method is shown to be more accurate than previous algorithms and thus can provide improved information on temporal and spatial nutrient variations beyond the climatological mean at regional and global scales.

1. Introduction

Monitoring and estimating primary production (PP) in marine environments rely heavily on satellite ocean-color observations due to their tremendously high spatial and temporal coverage not reached by any other current observing system. Many ocean color-based models that estimate PP depend on variables that can be retrieved from satellite observations using empirically derived algorithms (e.g., sea surface temperature (SST), photosynthetically active radiation, and chlorophyll (Chl)). PP is also estimated using ecosystem models, which often require the formulation of interactions among various agents, such as phytoplankton, zooplankton, and inorganic nutrients, representing the main ecosystem functions [Pahlow *et al.*, 2008]. Mechanistic models of phytoplankton growth offer the potential to provide further understanding of the physiological principles that regulate phytoplankton growth rates [e.g., Geider *et al.*, 1998; Pahlow *et al.*, 2013]. However, this kind of model commonly requires information on the availability of inorganic nutrients. Remote sensing tools offer synoptic information at the global level beyond the mean climatological state of different oceanic variables. Nevertheless, global estimations of sea surface nutrient concentrations are difficult to obtain from remote sensing, as there are no optical properties that allow their direct inference from satellite observations.

First attempts to indirectly assess nutrient availability in the surface ocean were based on nutrient-temperature-density relationships [Kamykowski and Zentara, 1986; Garside and Garside, 1995]. Most of the efforts have been directed at estimating dissolved inorganic nitrogen, which is regarded as the most immediate limiting nutrient in the ocean [Falkowski, 1997; Tyrrell, 1999; Moore *et al.*, 2013; Arteaga *et al.*, 2014]. More recently, nitrate concentrations have been diagnosed using satellite or in situ data of SST and mixed layer depth (MLD) [Steinhoff *et al.*, 2010] or SST and Chl [Goes *et al.*, 2000, 2004]. Goes *et al.* [2000, 2004] employed global relationships between surface nitrate concentration and SST and Chl, which are applicable to specific ocean basins. The methods developed by Kamykowski *et al.* [2002] and Switzer *et al.* [2003] used regional relationships based on 10° by 10° averages but provided only a relative assessment of nitrate availability. While Steinhoff *et al.* [2010] used a much finer (1° by 1°) grid for deriving their model, their algorithm is of regional nature and is based on a single multiple-regression function for the North Atlantic.

Despite these previous attempts, there is not yet an established product of nitrate concentrations in the surface layer of the ocean derived from remotely sensed data. Here we present a simple method to estimate monthly surface nitrate concentrations on a global scale by employing local multiple linear regressions using SST and Chl data from the Moderate Resolution Imaging Spectroradiometer (MODIS) and modeled

MLD. A major difference to previous methods, which are of an either regional or indirect nature, is that our approach is inherently local, i.e., it is applied on the same 1° by 1° resolution grid as the data on which it is based and thereby avoids the loss of information associated with averaging on a coarser grid.

2. Methods

In order to estimate surface nitrate concentration, we employ local multiple linear regressions using SST, MLD, and surface Chl as predictors of nitrate. Global surface Chl concentrations and SST are obtained from MODIS available from The Ocean Color site (<http://oceancolor.gsfc.nasa.gov>). To assess the general robustness of our method, we pragmatically employ different MLD models for the calibration and prediction periods. As the aim of our method is to provide monthly estimates of ocean surface nitrate concentrations in a semioperational mode, for the prediction period we choose to employ always the most recent—and presumably most accurate—available MLD model output. All MLD model outputs are obtained from the Ocean Productivity site of Oregon State University (<http://science.oregonstate.edu/ocean.productivity/index.php>): Monthly MLD outputs for 2003–2004 are from the SODAS model [Clancy and Sadler, 1992]. For the period January–June 2005, monthly MLD data were produced by an Isothermal Layer Depth (ILD) model of the Thermal Ocean Prediction System (TOPS), which is a model of the Fleet Numerical Meteorology and Oceanography Center (FNMOC), Monterey, California [Clancy and Martin, 1981; Clancy and Pollak, 1983; Clancy and Sadler, 1992] (ILD-TOPS). MLD for the period July 2005 to Sept 2008 is from a FNMOC high-resolution MLD criteria model. Finally, monthly MLD between October 2008 and December 2010 is from the Hybrid Coordinate Ocean Model [Bleck, 2002].

Since a sufficient seasonal coverage of remotely sensed Chl data could be obtained only for latitudes between 45°N and 45°S, we use only SST and MLD as predictors for higher latitudes. The coefficients of the linear regression are obtained for each 1° by 1° grid cell using the World Ocean Atlas 2009 (WOA09) monthly interpolated climatology of nitrate, and a training climatological data set of SST, Chl, and MLD. WOA09 is the only globally available training data set, and its temporal resolution is restricted to the monthly scale. Thus, it is currently not feasible to use a higher temporal resolution at the global scale. The training climatology is composed of average monthly SST and Chl MODIS data, and modeled MLD for January 2003 to December 2004:

$$(\beta_{\text{SST}}, \beta_{\text{MLD}}, \beta_{\text{Chl}}, C) = \text{regress}(\text{Nit}_{\text{WOA09}}, \text{SST}_{03-04}, \text{MLD}_{03-04}, \text{Chl}_{03-04}) \quad (1)$$

where β_{SST} , β_{MLD} , and β_{Chl} are the coefficients produced by the linear regression (regress) for monthly SST, MLD, and Chl respectively, and C is a local constant for each 1° by 1° grid cell (available as supporting information to this paper). $\text{Nit}_{\text{WOA09}}$, SST_{03-04} , MLD_{03-04} , and Chl_{03-04} are the monthly mean data sets employed to obtain the local regression coefficients.

Once the coefficients of the linear regression for each 1° by 1° grid cell are obtained, we force the multilinear model with an independent monthly data set of MODIS SST, Chl, and modeled MLD obtained for the period between January 2005 and December 2010:

$$\text{Nit}^{\text{est}} = \beta_{\text{SST}} \cdot \text{SST}_{05-10} + \beta_{\text{MLD}} \cdot \text{MLD}_{05-10} + \beta_{\text{Chl}} \cdot \text{Chl}_{05-10} + C \quad (2)$$

where Nit^{est} is the estimated nitrate. As a result, monthly global maps of estimated surface nitrate concentration are obtained on a 1° by 1° resolution grid for the period 2005–2010.

3. Results and Discussion

3.1. Global Patterns

Our predicted 1° by 1° temporally averaged surface nitrate concentration map for the period 2005–2010 is shown in Figure 1a. The spatial patterns of our modeled nitrate are consistent with the WOA09 nitrate climatology (Figure 1b). High nitrate concentrations are obtained at high latitudes, particularly the Southern Ocean, while tropical and subtropical areas show low concentrations, with the exception of the eastern Equatorial Pacific. The similarity of the spatial patterns of surface nitrate is encouraging given that the data set used to obtain the nitrate predictions (January 2005–December 2010) is independent from the data set used to derive the regression coefficients of the linear model (January 2003 to December 2004), and since we implicitly assume the general surface nitrate distribution in the global ocean for 2005–2010 to be similar to the climatology (WOA09).

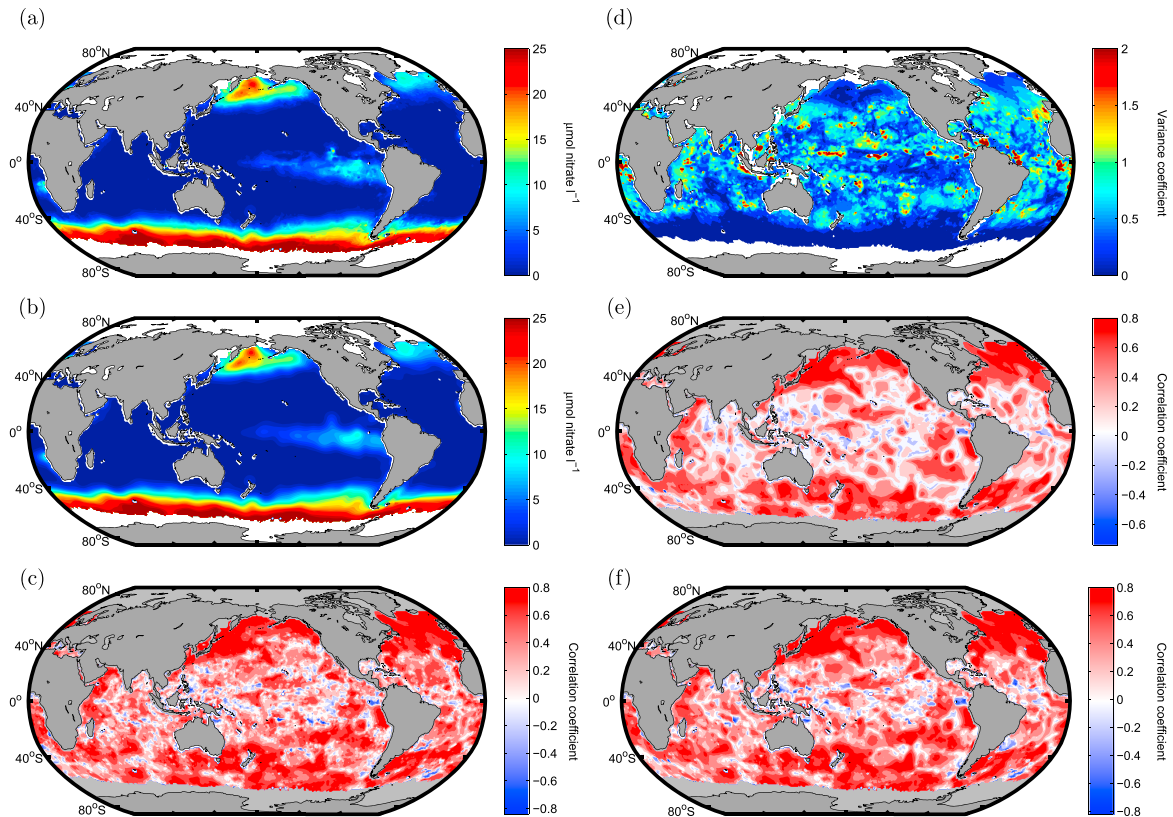


Figure 1. (a) Global surface nitrate concentration average for the period 2005–2010, estimated from SST, Chl, and MLD. (b) Global surface nitrate concentration climatology from World Ocean Atlas 2009 (WOA09). (c) Local correlation coefficient between our predicted nitrate concentrations and WOA09. (d) Variance coefficient of our 6 year predicted nitrate fields ($SD_{\text{monthly05-10}}/\text{mean}_{\text{monthly05-10}}$). (e) Local correlation coefficient between WOA09 and our predicted nitrate concentrations estimated from SST. (f) Local correlation coefficient between WOA09 and our predicted nitrate concentrations estimated from SST and MLD.

The local correlation coefficients (r) between our predicted monthly mean nitrate concentrations and WOA09 are highest at high latitudes, particularly in the northern North Atlantic and North Pacific, where r is close to 0.8 (Figure 1c). The correlation decreases toward the tropics, with very few scattered areas showing a negative correlation. The relative local monthly variance for our 6 years of predicted nitrate fields is calculated as the standard deviation of the whole monthly time series divided by its mean at each 1° by 1° grid point (Variance coefficient $vc = SD_{\text{monthly05-10}}/\text{mean}_{\text{monthly05-10}}$, Figure 1d). This relative temporal variance is highest in tropical regions ($vc \approx 2$) and decreases at midlatitudes ($vc \approx 1$), and toward the poles ($vc \approx 0$).

The relation between SST, MLD, Chl, and nitrate is not the same at all points of the ocean. Seasonal variations in stratification, and the concomitant changes in SST and MLD, are much stronger at higher latitudes in comparison with middle and tropical latitudes. Thus, biotic factors can potentially have a stronger influence on nitrate availability in low latitudes. In order to analyse the effect of including or excluding our individual predictor variables, we also performed univariate (one factor) and bivariate (two factors) linear regressions to evaluate the predictive capacity of employing only SST and/or MLD. Interestingly, when compared against the climatology, nitrate estimated only from SST as a predictor shows a relatively high global pointwise correlation coefficient ($r = 0.46$) (Figure 1e) compared to the multiple linear regression shown above (including SST, MLD, and Chl, $r = 0.51$, Figure 1c). The bivariate regression using both SST and MLD as predictors results in a global average r of 0.51 (Figure 1f), which is the same as for the regression including also Chl. The lack of improvement of the global correlation when Chl is added as a factor could be due to the

small magnitude of the variations in monthly surface nitrate concentrations over tropical and subtropical regions relative to the average concentrations. Nevertheless, Chl appears to contribute substantially to the predictive power of our method with respect to interannual variations, e.g., revealed in time series observations, as we discuss below.

3.2. Interannual and Seasonal Variabilities

The fact that our results replicate the spatial and monthly patterns of the climatology quite well is an encouraging result. However, as our aim is to obtain interannually varying rather than climatological mean monthly nitrate estimations, we compare our predicted monthly surface nitrate concentrations for 2005–2010 with available independent nitrate data obtained for the top 100 m of the ocean from the Bermuda Atlantic Time-series Study (BATS) (<http://bats.bios.edu>), the Hawaii Ocean Time series (HOT) (<http://hahana.soest.hawaii.edu>), the California Cooperative Oceanic Fisheries Investigations program (CalCOFI) (<http://www.calcofi.org>), and the Munida Time Series in the South Pacific Ocean, maintained by the National Institute of Water and Atmospheric Research of New Zealand (<http://cdiac.ornl.gov/oceans/Moorings/Munida.html>), for the same period. Our predicted nitrate estimations are obtained for 1° by 1° grid boxes at 29°N, 60°W for BATS, 24°N, 158°W for HOT, 38°N, 123°W for CalCOFI, and 48°S, 173°E for Munida. Our 1° by 1° estimates agree favorably with the interannual variability of the four ocean time series (Figures 2a–2d). The seasonal variability is predicted to a somewhat lesser degree by the model. For HOT and BATS, estimated nitrate values are somewhat higher than the in situ data, while for CalCOFI the opposite occurs. This is partly due to differences in nitrate concentrations at the selected locations (HOT, BATS, and CalCOFI) between the climatological data (WOA09) used to obtain the linear regression coefficients and the in situ data (Figure 2). The correlation coefficient between model outputs and monthly averaged in situ data for 2005–2010 is relatively good for BATS ($r = 0.53$), CalCOFI ($r = 0.73$), and Munida ($r = 0.60$), but not very high for HOT ($r = 0.16$). The root-mean-square error (RMSE) is relatively high for BATS ($0.24 \mu\text{mol L}^{-1}$) and HOT ($0.044 \mu\text{mol L}^{-1}$), due to their inherently low average nitrate concentration. The RMSE for Munida is low ($1.76 \mu\text{mol L}^{-1}$) and similar to the RMSE obtained by *Sherlock et al.* [2007] with a basin-scale model for the same area. For CalCOFI the RMSE is also relatively low ($2.50 \mu\text{mol L}^{-1}$) and similar to that obtained by *Palacios et al.* [2013] for the northern region of the CalCOFI sampling program with a regional model.

The seasonality in the WOA09 climatology is markedly different from that in the in situ observations for BATS (Figure 2a). Nevertheless, the model output follows both the seasonal and interannual variability of the in situ data, despite the slight overestimation, which indicates a strong local coupling between SST, MLD, surface Chl, and nitrate, essentially allowing a reliable prediction of surface nitrate from satellite-derived observations of those variables. In particular, the extremely high nitrate concentration at BATS in the winter 2009–2010 is well captured by our regression approach (Figure 2a). This underlines the predictive capability of our method since these concentrations are well outside the range of nitrate concentrations in the training data set (Figure 2a).

The observed relationship between nitrate, MLD, and temperature is due to the vertical transport of nutrients and cold water caused by deepening of the surface mixed layer [*Garside and Garside*, 1995]. Nutrient utilization and depletion by phytoplankton is the main process responsible for the correlation between nitrate and surface Chl. The relative contribution of each of these processes on the control of surface nitrate variations could be considerably different in the distinct areas of the global ocean. A comparison of in situ nitrate observations with nitrate estimations using only MLD as a predictor shows that MLD by itself is a poor predictor of nitrate at BATS (Figure 3a, MLD). The same occurs when only SST is employed in the linear regression (Figure 3a, SST). However, using Chl as the only predictor (Figure 3a, Chl) yields the highest correlation with the observations ($r = 0.55$, Table 1). Furthermore, the correlation between observed and modeled nitrate at BATS is high and positive only when Chl is included as a variable in the regression analysis (Table 1). This points to the importance of biological controls of nitrate at BATS and probably oligotrophic regions in general. *Goes et al.* [2000] reached similar conclusions by including Chl in their model for the Pacific Ocean. While our model shows the highest r when Chl is used as a single factor, the high nitrate concentrations observed in the in situ data during 2009 are replicated only when SST and MLD are also included in the regression (Figure 2a). The importance of employing all three variables in the regression analysis is visually clear, however, this does not appear to be reflected in the RMSE, due to (slight) mismatches in the predicted and observed timing of the nitrate peak. When SSTs or Chls are used as the only predictors of nitrate at HOT, the correlation with the observations is negative (Figure 3b, SST and Chl). MLD as the only predictor results in a low positive correlation (Figure 3b, MLD). This suggests that nitrate

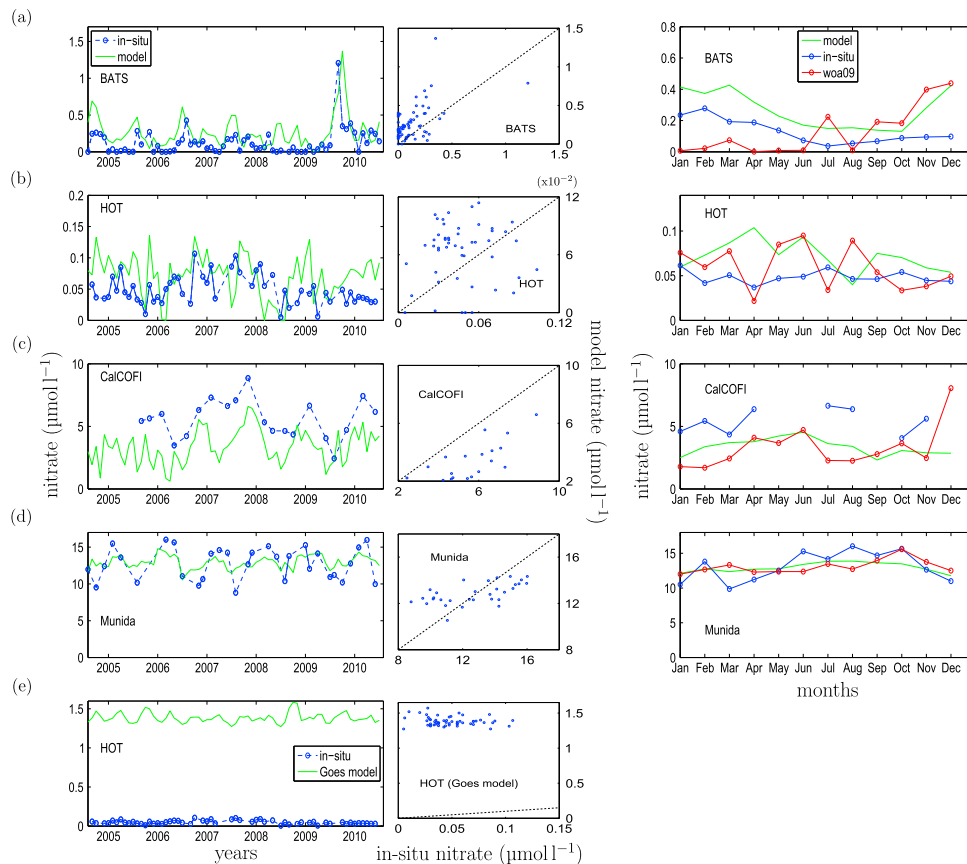


Figure 2. (left) Monthly predicted (green continuous line) and in situ measured (blue dashed line) surface nitrate concentrations for the period 2005–2010. (middle) Scatterplots for modeled and in situ nitrate concentrations and one-to-one (dashed) line. (right) Average monthly nitrate concentrations from January 2005 to December 2010. Model: green continuous line; In situ: blue dots connected with line; WOA09 climatology: red dots connected with line. Model predictions and observations are presented for (a) BATS, (b) HOT, (c) CalCOFI, and (d) Munida. (e) Nitrate prediction obtained for HOT with the model from Goes *et al.* [2000].

concentrations at HOT might also be strongly influenced by other physical or biogeochemical processes not captured by either SST, MLD, or Chl. While our approach is based on the idea that nitrate is either controlled by vertical mixing or phytoplankton consumption, other mechanisms, such as horizontal advection, have been suggested as important contributors of nutrient supply in the Pacific Ocean [Dave and Lozier, 2013].

SST and Chl are also poor single predictors of nitrate at CalCOFI. Similarly, as for HOT, MLD appears to be the best predictor in this region (Figure 3c). While combining MLD and SST results in the highest r for this region ($r = 0.77$, Table 1), the right magnitude of nitrate variations is only replicated when Chl is also included in the regression (Figure 2c). The obtained r for the regression with MLD, SST, and Chl ($r = 0.73$, Table 1) is only slightly lower than for only MLD and SST. Palacios *et al.* [2013] reached similar conclusions in their study, where the addition of physical and biological related variables such as temperature, salinity, and oxygen increased the explanatory power of their regional model for the CalCOFI area. Station Munida is located beyond 45°S; therefore, Chl cannot be included as part of the multiple regression. However, employing the available abiotic predictors SST and MLD individually results in high correlation coefficients (Table 1). For this station, using MLD or SST as the only predictor of nitrate results in a higher correlation coefficient than including both variables in the regression ($r = 0.75$ for MLD, $r = 0.66$ for SST, $r = 0.60$ for SST and MLD), which is likely due to a mismatch between WOA09 and in situ data at this site. As the difference between the

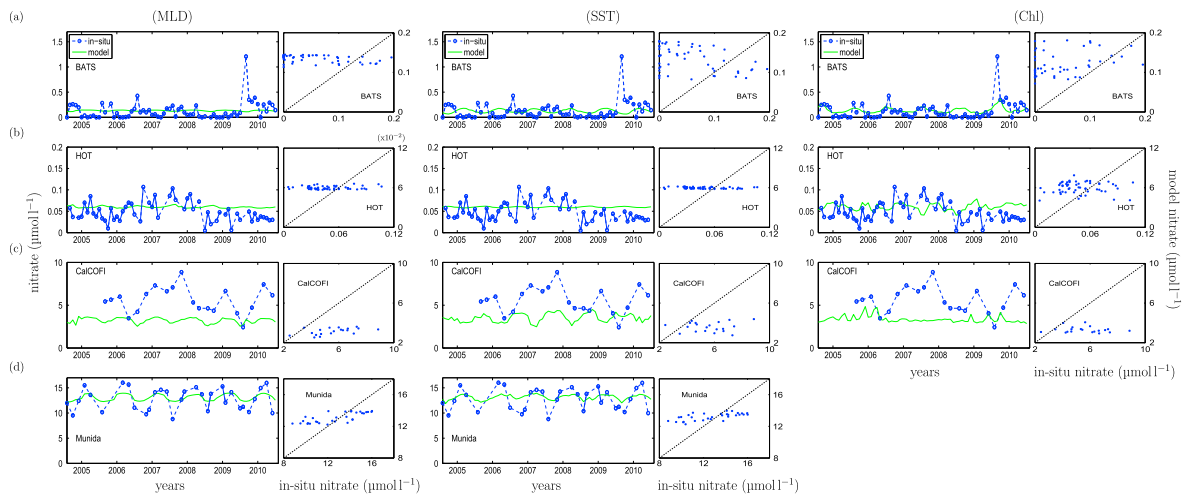


Figure 3. Monthly predicted (green continuous line) and in situ measured (blue dashed line) surface nitrate concentrations from January 2005 to December 2010 along with scatterplots for modeled and in situ nitrate concentrations and one-to-one (dashed) line, for (a) BATS, (b) HOT, (c) CalCOFI, and (d) Munida. Modeled nitrate was obtained with single linear regressions using only MLD (left), SST (middle), and Chl (right) as individual predictors.

correlations employing all available or individual variables is not very large, and it is impossible to discern beforehand which variable is the best predictor for nitrate in a particular point in the ocean, we thus stick to employing all three variables (SST, MLD, and Chl) in the regression analysis as long as they are available.

The use of a 1° by 1° grid avoids averaging and thereby minimizes information loss, which is a major distinction to most previous methods for estimating global nitrate distribution from satellite-derived data [e.g., Goes *et al.*, 2000]. As might be expected, our locally derived relations provide a much improved local predictive power compared to the basin-scale relationships. Figure 2e compares the model of Goes *et al.* [2000] for the nonequatorial Pacific using our forcing SST and Chl data set with observations at HOT. Although working well on the basin scale, the method of Goes *et al.* [2000] highly overestimates nitrate concentrations at HOT between 2005 and 2010, and the predicted nitrate is anticorrelated with the independent in situ observations (Figure 2e and Table 1).

3.3. Error Analysis

The predictive power of our method depends to a large extent on the accurate estimation of SST and Chl from remote sensing, and on the quality of the modeled MLD. Since we use linear regressions, systematic

Table 1. Correlation Coefficients (*r*) and Root-Mean-Square Errors (RMSE) for Nitrate Prediction Using Different Predictors (SST, MLD, and Chl) and In Situ Observations for 2005–2010 at HOT, BATS, CalCOFI, and Munida^a

Model variables	<i>r</i>				RMSE			
	HOT	BATS	CalCOFI	Munida	HOT	BATS	CalCOFI	Munida
SST	−0.20	−0.43	0.07	0.66	0.025	0.19	2.50	1.94
MLD	0.10	−0.45	0.52	0.75	0.025	0.18	2.77	1.76
Chl	−0.002	0.55	−0.14	-	0.027	0.15	2.76	-
SST MLD	0.06	−0.36	0.77	0.60	0.025	0.18	2.50	1.76
SST Chl	−0.04	0.34	0.05	-	0.027	0.16	2.52	-
MLD Chl	0.08	0.52	0.27	-	0.037	0.22	2.81	-
SST MLD Chl	0.16	0.53	0.73	-	0.044	0.24	2.50	-
Goes model (HOT)	−0.16	-	-	-	1.34	-	-	-

^aGoes model (HOT) refers to the model by Goes *et al.* [2000] evaluated against in situ data from HOT. Number of sample points for HOT = 55, BATS = 69, Munida = 31, and CalCOFI = 41.

errors have no effect. Thus, we restrict the error analysis to random errors (noise). To our knowledge, no method exists to separate systematic and random error components. Instead, we here employ the data used for validation to estimate the maximum random error which still allows reproducing the nitrate data in Figure 2. We apply various degrees of noise to the SST, MLD, and Chl data sets and then repeat the above training and validation procedure with the noisy data sets. The maximum noise level still reproducing the time series observations is then applied to the global ocean to obtain an estimate of the local uncertainty of the model prediction.

We introduce random noise to each of the forcing data sets (SST, MLD, and Chl) used in the linear regression, via,

$$ns = \text{data} + \sigma \cdot a \cdot x \quad (3)$$

where ns is the newly created “noisy signal,” data is the original satellite-derived data (SST, Chl, or MLD for 2003–2004), σ is the temporal standard deviation of each grid point of the annual mean map of data, a is a coefficient determining the overall noise level, and x is a uniformly distributed random number between 0 and 1. We then compare the predictive power our method applied to the noisy data sets (i.e., ns_{sst} , ns_{chl} , ns_{mld}), against that resulting from the original (unaltered) data sets.

We employ noise levels obtained with $a = 1, 0.25,$ and 0.1 . The main effect of the noise is a reduction in the predicted amplitude of the seasonal and interannual variations in nitrate concentrations. Only for the lowest noise level, i.e., $a = 0.1$, the resulting predicted nitrate is similar to the prediction without noise (Figure S1). Our method performs much worse with the noisy data sets with respect to the nitrate peak in early 2010, which is reproduced only with the lowest noise level (Figure S1b).

Our error analysis shows that the accuracy of our method can effectively be hampered by the presence of large random errors in the predictive data sets. The fact that the maximum random error compatible with the predictive power indicated in Figure 2 is obtained with $a = 0.1$ suggests a low random error in the satellite-based SST and Chl, and modeled MLD, which are used as predictors of nitrate in the linear regression. Keeping in mind that our artificial noise is added to the actual random error in the modeled and satellite-derived inputs, this result tells us that increasing the noise level (i.e., reducing the accuracy) by more than 10% over the current level would strongly interfere with our ability to obtain useful predictions of surface nitrate concentrations. While some uncertainty remains about the right magnitude of random errors in the forcing data sets, it appears unlikely that the actual noise level is much higher than our maximum estimate. For example, our relatively low upper limit of noise in the satellite-derived Chl compared to the previously estimated 35% [Moore *et al.*, 2009] suggests that either the local error in the satellite-derived and modeled inputs is lower than currently thought or that most of the error can be considered systematic at the local scale of our analysis.

To assess the global effect of our maximum error estimate, i.e., equivalent to adding 10% of σ ($a = 0.1$) to any possibly existing noise, we compute the relative difference (reldiff) between the originally predicted nitrate and the nitrate obtained with a random error induced in the forcing satellite data sets with $a = 0.1$, on each $1^\circ \times 1^\circ$ pixel (Figure S1d):

$$\text{reldiff} = \frac{\text{Nit}^{\text{est}} - \text{Nit}_{a=0.1}^{\text{est}}}{0.5(\text{Nit}^{\text{est}} + \text{Nit}_{a=0.1}^{\text{est}})} \quad (4)$$

where Nit^{est} is the originally predicted nitrate, $\text{Nit}_{a=0.1}^{\text{est}}$ is the nitrate predicted with the random error for $a = 0.1$ applied to the predictive data set. The errors reflect the combined effects of random errors in the three forcing data sets. The relative error is rather small and varies between $\pm 20\%$, with larger errors generally restricted to low and middle latitudes and very small errors (within $\pm 2\%$) found at high latitudes (Figure S1). Therefore, we conclude that the errors associated with the satellite-derived data sets do not appear to hamper our satellite-based method of predicting nitrate distributions for the world ocean.

4. Summary and Conclusions

We present a new method to estimate monthly surface nitrate distributions on a global 1° by 1° resolution grid. Our method is based on local multiple linear regressions applied at each 1° grid cell, employing SST, Chl, and MLD as predictors for nitrate. We evaluate the predictive power of our method against in situ data

from the oceanographic time series from stations BATS, HOT, CalCOFI, and Munida. Our modeled nitrate agrees well with the interannual variability of these stations, while the seasonal variability is reproduced to a lesser extent. Biological processes, represented by Chl, seem to have an important role controlling nitrate variations at BATS. While our analysis seems to indicate that the mechanisms controlling nitrate at HOT are not particularly well represented by either SST, MLD, or Chl, at Munida, nitrate can be well inferred through SST and MLD. At CalCOFI, MLD seems to be the main determinant of nitrate variations; however, SST and Chl are also required to reproduce the variability of the in situ observations. Despite a markedly different seasonality between the WOA09 nitrate and the in situ observations, our method is still able to follow the variability of the in situ data, indicating strong coupling between SST, MLD, surface Chl, and nitrate. Our error analysis of the predictive data set suggests that the method is robust as long as the errors in the forcing data sets do not exceed about 10% of the seasonal variance of the data. This provides some confidence in the use of satellite-derived SST and Chl and modeled MLD, to predict real surface nitrate concentrations in the global ocean.

Local and regional nitrate prediction models remain highly valuable to investigate controls of nitrate at the regional scale. Our nitrate prediction method allows to easily estimate nitrate variations at a global scale and offers the possibility to employ mechanistic models of marine biological production [e.g., Pahlow *et al.*, 2013] that require information on dissolved inorganic nitrogen availability. The sensitivity of phytoplankton growth rates to nutrient variations is an important constraint that needs to be taken into account in the monitoring and prediction of marine biological primary productivity under changing environmental conditions.

Acknowledgments

We wish to thank M. Behrenfeld and R. O'Malley for sharing their expertise on the mixed layer depth data obtained from the Ocean Productivity site of Oregon State University (<http://www.science.oregonstate.edu/ocean.productivity/index.php>). The research leading to these results has received funding from the European Community's Seventh Framework Programme FP7/2007-2013, Space Theme, under grant agreement 282723 (OSS2015). This work is also a contribution of the Sonderforschungsbereich 754 "Biogeochemistry Interactions in the Tropical Ocean" (www.sfb754.de). All the details and web addresses needed to access the data used to produce our results are described in the section 2 of this paper, as well as in the supporting information.

The Editor thanks two anonymous reviewers for their assistance in evaluating this paper.

References

- Arteaga, L., M. Pahlow, and A. Oschlies (2014), Global patterns of phytoplankton nutrient and light colimitation inferred from an optimality-based model, *Global Biogeochem. Cycles*, 28(7), 648–661, doi:10.1002/2013GB004668.
- Bleck, R. (2002), An oceanic general circulation model framed in hybrid isopycnal-Cartesian coordinates, *Ocean Model.*, 4(1), 55–88, doi:10.1016/S1463-5003(01)00012-9.
- Chen, D., L. M. Rothstein, and A. J. Busalacchi (1994), A hybrid vertical mixing scheme and its application to tropical ocean models, *J. Phys. Oceanogr.*, 24(10), 2156–2179, doi:10.1175/1520-0485(1994)024<2156:AHVMSA>2.0.CO;2.
- Clancy, R. M., and P. J. Martin (1981), Synoptic forecasting of the oceanic mixed layer using the navy's operational environmental data base: Present capabilities and future applications, *Bull. Am. Meteorol. Soc.*, 62(6), 770, doi:10.1175/1520-0477(1981)062<0770:SFOTOM>2.0.CO;2.
- Clancy, R. M., and K. D. Pollak (1983), A real-time synoptic ocean thermal analysis/forecast system, *Prog. Oceanogr.*, 12(4), 383–424, doi:10.1016/0079-6611(83)90001-0.
- Clancy, R. M., and W. D. Sadler (1992), The fleet numerical oceanography center suite of oceanographic models and products, *Weather Forecasting*, 7(2), 307–327, doi:10.1175/1520-0434(1992)007<0307:TFNOC>2.0.CO;2.
- Dave, A. C., and M. S. Lozier (2013), Examining the global record of interannual variability in stratification and marine productivity in the low-latitude and mid-latitude ocean, *J. Geophys. Res. Oceans*, 118, 3114–3127, doi:10.1002/jgrc.20224.
- Falkowski, P. G. (1997), Evolution of the nitrogen cycle and its influence on the biological sequestration of CO₂ in the ocean, *Nature*, 387, 272–275, doi:10.1038/246170a0.
- Friedrichs, M. A., et al. (2009), Assessing the uncertainties of model estimates of primary productivity in the tropical Pacific Ocean, *J. Mar. Syst.*, 76, 113–133, doi:10.1016/j.jmarsys.2008.05.010.
- Garside, C., and J. Garside (1995), Euphotic-zone nutrient algorithms for the NABE and EqPac study sites, *Deep Sea Res. Part II*, 42(2–3), 335–347, doi:10.1016/0967-0645(95)00026-M.
- Geider, R. J., H. L. MacIntyre, and T. Kana (1998), A dynamic regulatory model of phytoplankton acclimation to light, nutrients, and temperature, *Limnol. Oceanogr.*, 43(4), 679–694, doi:10.4319/lo.1998.43.4.0679.
- Goes, J. I., T. Saino, H. Oaku, J. Ishizaka, C. S. Wong, and Y. Nojiri (2000), Basin scale estimates of sea surface nitrate and new production from remotely sensed sea surface temperature and chlorophyll, *Geophys. Res. Lett.*, 27(9), 1263–1266, doi:10.1029/1999GL002353.
- Goes, J. I., H. D. R. Gomes, A. Limsakul, and T. Saino (2004), The influence of large-scale environmental changes on carbon export in the North Pacific Ocean using satellite and shipboard data, *Deep Sea Res., Part II*, 51, 247–279, doi:10.1016/j.dsr2.2003.06.004.
- Kamykowski, D., and S.-J. Zentara (1986), Predicting plant nutrient concentrations from temperature and sigma-t in the upper kilometer of the world ocean, *Deep Sea Res., Part A*, 33(1), 89–105, doi:10.1016/0198-0149(86)90109-3.
- Kamykowski, D., S.-J. Zentara, J. M. Morrison, and A. C. Switzer (2002), Dynamic global patterns of nitrate, phosphate, silicate, and iron availability and phytoplankton community composition from remote sensing data, *Global Biogeochem. Cycles*, 16(4), 1077, doi:10.1029/2001GB001640.
- Minnett, P. J., R. H. Evans, E. J. Kearns, and O. B. Brown (2002), Sea-surface temperature measured by the Moderate Resolution Imaging Spectroradiometer (MODIS), paper presented at IGARSS '02 Geoscience and Remote Sensing IEEE International Symposium, Anchorage, Alaska, 24–28 June 2002, vol. 2, pp. 1177–1179, doi:10.1109/IGARSS.2002.1025872.
- Minnett, P. J., O. B. Brown, R. H. Evans, E. L. Key, E. J. Kearns, K. Kilpatrick, A. Kumar, K. A. Maillat, and G. Szczodrak (2004), Sea-surface temperature measurements from the Moderate-Resolution Imaging Spectroradiometer (MODIS) on Aqua and Terra, paper presented at IGARSS '04 Geoscience and Remote Sensing IEEE International Symposium, Anchorage, Alaska, 20–24 Sept. 2004, vol. 7, pp. 4576–4579, doi:10.1109/IGARSS.2004.1370173.
- Moore, C. M., et al. (2013), Processes and patterns of oceanic nutrient limitation, *Nat. Geosci.*, 6, 701–710, doi:10.1038/ngeo1765.
- Moore, T. S., J. W. Campbell, and M. D. Dowell (2009), A class-based approach to characterizing and mapping the uncertainty of the MODIS ocean chlorophyll product, *Remote Sens. Environ.*, 113, 2424–2430, doi:10.1016/j.rse.2009.07.016.

- Palacios, D. M., E. L. Hazen, I. D. Schroeder, and S. J. Bograd (2013), Modeling the temperature-nitrate relationship in the coastal upwelling domain of the California current, *J. Geophys. Res. Oceans*, *118*, 3223–3239, doi:10.1002/jgrc.20216.
- Pahlow, M., A. F. Vézina, B. Casault, H. Maass, L. Malloch, D. G. Wright, and Y. Lu (2008), Adaptive model of plankton dynamics for the North Atlantic, *Prog. Oceanogr.*, *76*(2), 151–191, doi:10.1016/j.pocean.2007.11.001.
- Pahlow, M., H. Dietze, and A. Oschlies (2013), Optimality-based model of phytoplankton growth and diazotrophy, *Mar. Ecol. Prog. Ser.*, *489*, 1–16, doi:10.3354/meps10449.
- Sherlock, V., S. Pickmere, K. Currie, M. Hadfield, S. Nodder, and P. W. Boyd (2007), Predictive accuracy of temperature-nitrate relationships for the oceanic mixed layer of the New Zealand region, *J. Geophys. Res.*, *112*, C06010, doi:10.1029/2006JC003562.
- Steinhoff, T., T. Friedrich, S. E. Hartman, A. Oschlies, D. W. R. Wallace, and A. Körtzinger (2010), Estimating mixed layer nitrate in the North Atlantic Ocean, *Biogeosciences*, *7*(3), 795–807, doi:10.5194/bg-7-795-2010.
- Switzer, A. C., D. Kamykowski, and S.-J. Zentara (2003), Mapping nitrate in the global ocean using remotely sensed sea surface temperature, *J. Geophys. Res.*, *108*(C8), 3280, doi:10.1029/2000JC000444.
- Tyrrell, T. (1999), The relative influences of nitrogen and phosphorus on oceanic primary production, *Nature*, *400*(6744), 525–531, doi:10.1038/22941.

Auxiliary material for
Global sea-surface nitrate fields estimated from remotely sensed sea-surface
temperature, chlorophyll and modeled mixed layer depth

Lionel Arteaga¹, Markus Pahlow¹, Andreas Oschlies¹

¹GEOMAR Helmholtz Centre for Ocean Research Kiel, Kiel, Germany

Geophysical Research Letters [2014GL062363]

Introduction

This auxiliary material contains one supplementary Figure and one supplementary data set. Figure fs01 shows the results of the error analysis described in section 3.3 *Error analysis*. The data set is a netCDF file, “ds01.nc”, that contains local coefficients obtained from the linear regression, β_{sst} , β_{MLD} , β_{Chl} , C , for each oceanic pixel on a $1^\circ \times 1^\circ$ resolution grid. These coefficients can be combined with data from SST, surface Chl, and MLD to estimate surface nitrate concentrations in the global ocean following Equation 2.

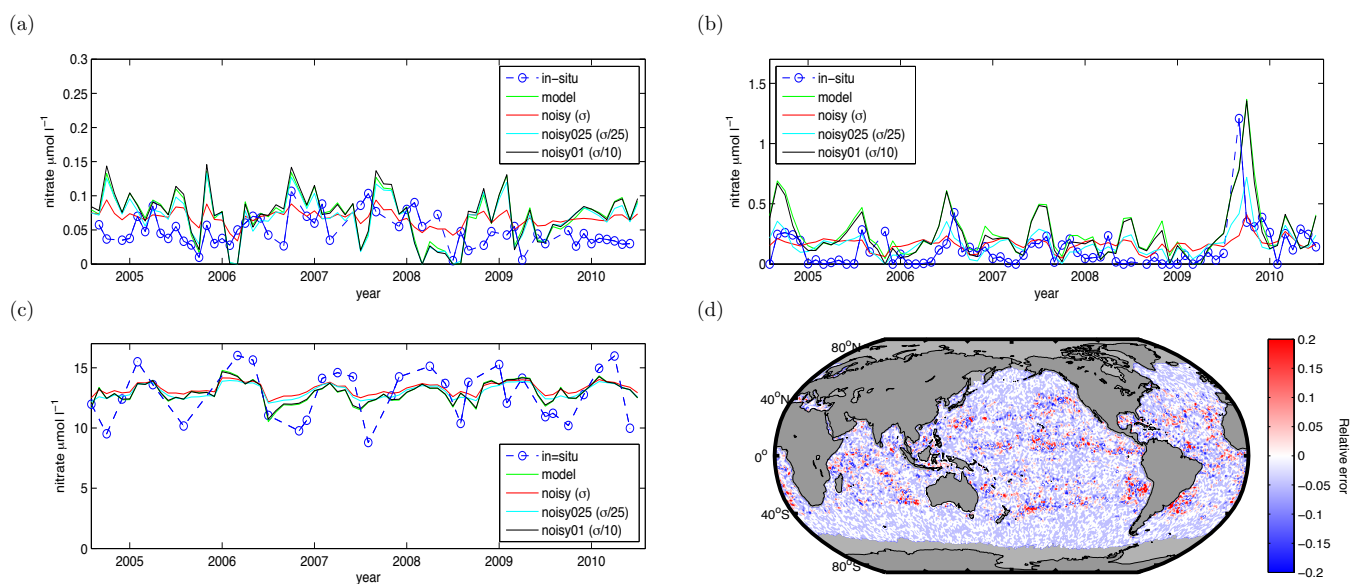
Data

1. ds01.nc: netCDF file of 6 variables (var) and 2 dimensions (dim) with local coefficients for global nitrate estimation.

- 1.1 var1 (dim1): Longitude (size[360 1])
- 1.2 var2: (dim2) Latitude (size[180 1])
- 1.3 var3: Constant coefficient C (size[360 180])
- 1.4 var4: SST coefficient (size[360 180])
- 1.5 var5: MLD coefficient (size[360 180])
- 1.6 var6: Chl coefficient (size[360 180])

Figures

fs01.pdf - Monthly predicted original (green continuous line) and predictions obtained with high ($a = 1$, red continuous line “noisy”), medium ($a = 0.25$, cyan continuous line noisy025), and low ($a = 0.01$, black continuous line “noisy01”) noise levels added to the predictor datasets of nitrate concentrations for HOT (a), BATS (b), and Munida (c) from January 2005 to December 2010. In-situ data: blue dashed line. (d) Global distribution of relative differences between original predicted nitrate (Figure 1a) and nitrate predicted with the maximum estimated random error induced in the predictive data set ($a=0.01$).



2.3 Chapter 3: *Contribution of phytoplankton to particulate organic carbon in the global ocean.*

Lionel Arteaga, Markus Pahlow, and Andreas Oschlies.

Manuscript in preparation.

Contribution of phytoplankton to particulate organic carbon in the global ocean

(Lionel Arteaga, Markus Pahlow, Andreas Oschlies)

(DRAFT)

Abstract

Primary production by marine phytoplankton essentially drives the oceanic biological carbon pump. Global productivity estimates are mostly founded on chlorophyll-based primary production models (*Field, 1998*). A major drawback of this approach is that variations in chlorophyll concentration do not necessarily account for changes in phytoplankton biomass resulting from the physiological regulation of the chlorophyll-to-carbon ratio (Chl:C) (*Geider, 1987; MacIntyre et al., 2000*). Here we present phytoplankton production rates and C concentrations for the global ocean for 2005–2010 obtained by combining satellite Chl observations with a mechanistic model for the acclimation of phytoplankton stoichiometry to variations in nutrients, light and temperature. We compare our inferred phytoplankton C concentrations with an independent estimate of surface particulate organic carbon (POC) to identify for the first time the global contribution of phytoplankton to total POC in the surface ocean. Our annual primary production (46 Pg C yr^{-1}) matches the estimate of a C-based model obtained from satellite observations. We find that most of the oligotrophic ocean is dominated by autotrophic biomass (between 30 and 70% of total carbon). Lower contributions are found in the tropical Pacific POC (10–30% phytoplankton) and the Southern Ocean ($\approx 10\%$). Our method provides a novel analytical tool to identify changes in marine plankton communities and carbon export.

Marine ecosystems contribute substantially to global biogeochemical fluxes transporting photosynthetically fixed organic carbon from the sunlit surface layer to the deep sea, and hence acting as a major regulator of the partitioning of carbon among atmosphere and ocean (*Raven and Falkowski, 1999*). Photosynthesis by phytoplankton constitutes the principal supply route of carbon into the marine ecosystem. While phytoplankton is often measured as chlorophyll (Chl), productivity is usually determined in carbon units (*Cloern et al., 1995*). Global marine primary production (PP) rates are commonly estimated via ocean color-based algorithms using remotely-sensed observations. Early algorithms were generally founded on empirical relations between irradiance, pigment concentration (i.e., Chlorophyll) and estimates of carbon fixation rates (e.g., ^{14}C) (*Behrenfeld and Falkowski, 1997a*). These relations implicitly assume that phytoplankton C (phyto-C) biomass is proportional to Chl concentration, which is not generally true (*Geider et al., 1986; Armstrong, 2006*). Hence, a common drawback of these models is that they do not account for the acclimation of the phytoplankton chlorophyll to carbon ratio (Chl:C) to changes of light and nutrient conditions in the environment.

Nutrient and light (co-)limitation induces physiological changes in phytoplankton composition, which is reflected in the Chl:C ratio (*Geider, 1987; MacIntyre et al., 2000; Arteaga et al., 2014*). Due to this plasticity, Chl can be a poor indicator of phytoplankton biomass (*Westberry et al., 2008*). Among the first global PP estimates that accounted for variations of the Chl:C ratio, is the model of *Behrenfeld et al. (2005)*. *Behrenfeld et al. (2005)* developed a satellite-based PP algorithm that relies on the inference of phytoplankton POC through the estimation of the particulate beam attenuation coefficient at 660 nm (c_p). This carbon-based model (CbPM) was later improved by *Westberry et al. (2008)*, through accounting for changes in the light spectrum with depth, and hence giving a more realistic photoacclimation of phytoplankton to vertically varying light conditions. These modifications led to a lower estimate for global annual production compared to the CbPM initially formulated by *Behrenfeld et al. (2005)* of 67 to 52 Pg C yr⁻¹ (*Westberry et al., 2008*), much closer to the global mean found for different Chl, C-based, and Global Circulation Models (GCM) of 51 Pg C yr⁻¹ (*Carr et al., 2006*).

The diverse physiological effects of nutrient and light limitation can be represented in mechanistically founded phytoplankton models (*Geider et al., 1998; Pahlow and Oschlies, 2009; Pahlow et al., 2013*). Cell quota models have the potential to decouple phytoplankton elemental components (e.g. C, nitrogen (N), phosphorus (P), Chl), while optimality-based models provide the mechanistic foundation to describe physiological acclimation of phytoplankton to a variable physico-chemical environment (*Smith et al., 2011*). We here show that combining empirically-derived color-based observations and mechanistically-founded biological models

can provide further insights into the regulating mechanisms and variability of phytoplankton biomass and associated primary production in the global ocean.

Improved estimates of phytoplankton carbon can also lead to better assessments of carbon export from the surface ocean. The distinction between carbon associated with primary producers and carbon associated with heterotrophic organisms provides valuable information on the assemblage of the ecosystem. Its structure controls the trophic pathways of carbon and eventually the flux of particulate organic carbon that reaches the deep ocean (*Duarte and Cebrin, 1996; Francois et al., 2002*). Here, we estimate seasonally and interannually varying synoptic patterns of phytoplankton carbon biomass in the global ocean. We employ a biological model that describes phytoplankton acclimation to nutrient and light to calculate phytoplankton Chl:C ratios and phytoplankton growth rates. When combined with independent satellite-based observations of surface Chl and POC, we can then quantify global production rates, phytoplankton biomass and, for the first time, its contribution to total POC.

Primary production

We estimate primary production rates integrated over the euphotic depth (Z_{eu}) using a mechanistic phytoplankton physiological model (*Pahlow et al., 2013*) (Fig. 1). The model defines the physiological roles of nitrogen and phosphorus via their association with specific functional cellular compartments (*Sterner and Elser, 2002*). According to this model, net C fixation is directly limited by cellular N. The model optimizes the allocation of cellular N and energy among requirements for nutrient acquisition and light availability (*Pahlow et al., 2013; Arteaga et al., 2014*). Phosphorus constrains nitrogen assimilation in the ribosomes, and thereby limits nitrogen acquisition. As phosphorus has been previously identified as a secondary limiting nutrient with respect to nitrogen (*Arteaga et al., 2014*), we restrict nutrient limitation in this study only to nitrogen.

Monthly phytoplankton growth rates and Chl:C ratios are estimated from the model for the period January, 2005–December, 2010. We initially run the optimality-based model with an average parameter set (Table S.1) obtained for different phytoplankton species (*Pahlow et al., 2013*). We use the resulting biomass-normalised nitrogen cell-quota (phytoplankton N:C ratio, Q^N) and an estimate of light saturation of the cellular light-harvesting apparatus (S_I) to infer nitrogen limitation (L_n) as the relative difference between Q^N and the phytoplankton subsistence quota (Q_0^N), and light limitation as one minus the degree of light

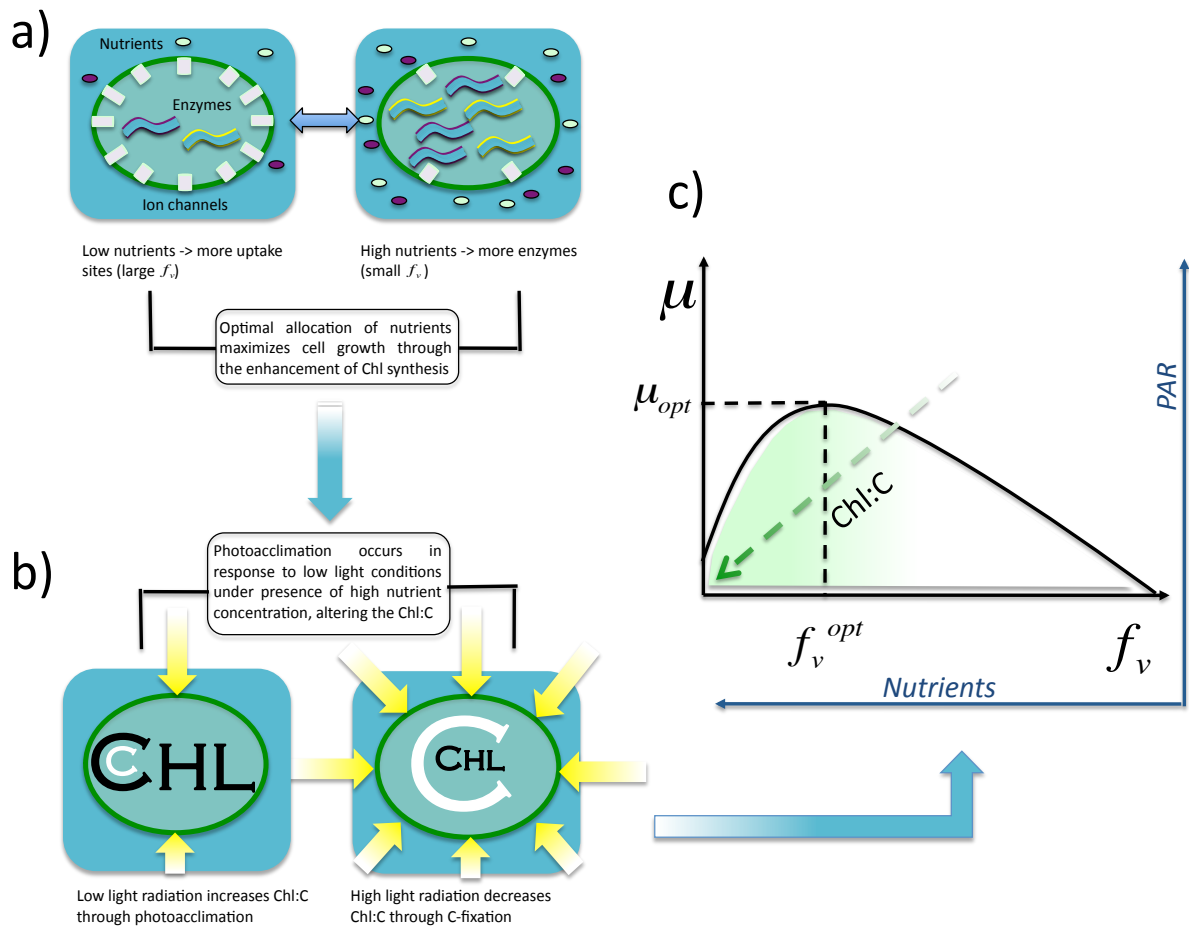


Figure 1: General concept of the optimality-based model: (a) Optimal allocation of nitrogen maximises growth: A greater nitrogen quota fraction (f_v) is allocated for nutrient acquisition when extracellular nutrient concentration is low (left). For higher nutrient concentrations more nitrogen is allocated for carbon fixation (right). Hence, f_v increases as the extracellular nutrient concentration drops. (b) The Chl:C ratio is the result of both photoacclimation and nitrogen allocation. With low light and sufficient nitrogen, Chl is synthesized to enhance light harvesting efficiency, resulting in an increased Chl:C ratio. High light conditions down-regulate Chl production, decreasing Chl:C. (c) Net cell growth is maximized via optimal allocation of nitrogen resources. The Chl:C ratio is maximized by high nutrient-low light conditions, and decreases as light levels increase and/or nutrient concentrations diminish.

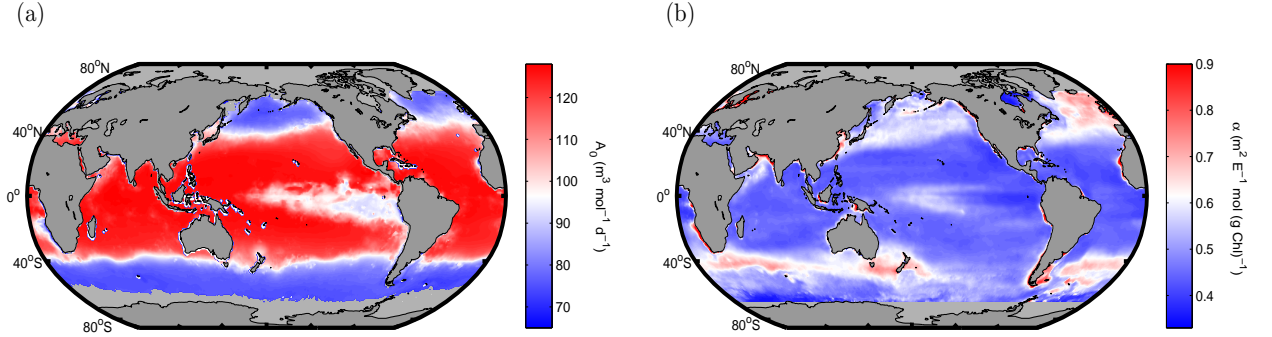


Figure 2: Global distribution of (a) nutrient affinity (A_0) and (b) light affinity (α) as functions of nutrient and light limitation, respectively, estimated by the optimality-based model (*Pahlow et al., 2013*).

saturation (*Arteaga et al., 2014*):

$$L_n = 1 - \frac{Q^n - Q_0^n}{Q^n} = \frac{Q_0^n}{Q^n} \quad (1)$$

$$L_l = 1 - S_l \quad (2)$$

where $L_n = 0$ and $L_l = 0$ indicate no limitation, and $L_n = 1$ and $L_l = 1$ indicate strong limitation.

We then employ L_n and L_l to represent multiple phytoplankton species adapted to different light and nitrogen limitation regimes across the global ocean. Phytoplankton species are defined by varying their Chl-specific light affinity (α) and potential nutrient affinity (A_0) as a function of light and nutrient limitation via

$$\alpha = a_\alpha L_l + b_\alpha \quad (3)$$

$$A_0 = a_A L_n + b_A \quad (4)$$

where the corresponding slopes (a) and offsets (b) are $a_\alpha = 1$, $a_A = 100$, $b_\alpha = 0.3$, and $b_A = 40$, respectively. This results in a general latitudinal pattern composed of phytoplankton with high α and low A_0 in high latitudes and vice versa in tropical regions (Fig. 2). Finally, we apply the phytoplankton model employing the α and A_0 maps obtained with Eqs. (3) and (4) to obtain our estimate of global phytoplankton growth rates and Chl:C ratios.

We calculate global vertically integrated production rates using independent monthly observations of phytoplankton Chl from the Moderate Resolution Imaging Spectroradiometer (MODIS), and Z_{eu} (m) (*Morel and*

Berthon, 1989), using,

$$PP = rgr_m \cdot (C:Chl)_m \cdot Chl_{MODIS} \cdot Z_{eu} \quad (5)$$

where rgr_m and $(C:Chl)_m$ are the predicted growth rate (d^{-1}) and C:Chl ratio ($mol\ mg^{-1}$), and Chl_{MODIS} is the Chl concentration ($mg\ Chl\ m^{-3}$) estimated from the MODIS sensor.

Our estimated global patterns of PP (Fig. 3a) are similar to those obtained by the CbPM (*Westberry et al., 2008*) for the same study period (Fig. 3b), and yield the same annual production rate when both methods are applied to those regions for which satellite data are available ($46\ Pg\ C\ y^{-1}$). Compared to a commonly used Chl-based PP model (i.e., VGPM, *Behrenfeld and Falkowski, 1997b*) (Fig. 3c), our C-based estimation results in higher production rates in tropical regions and lower PP rates in high latitudes. The main reason for this shift in global production patterns is the compensation effect of the variable Chl:C ratio. High Chl concentrations are translated into high PP rates in Chl-based models. In our model-data analysis, high Chl concentrations at high latitudes coincide with high Chl:C ratios resulting from the acclimation of phytoplankton to high-nutrient, low-light conditions. Our predicted Chl:C ratios are thus the result of a balance between the need and the feasibility for photoacclimation as driven by the availability of nutrients and light (*Arteaga et al., 2014*). Thus, our results suggest that high Chl concentrations at high latitudes during winter months are mainly due to photoacclimation, and not increase in phytoplankton (C)-biomass. Overall, our annual PP rate for 2005–2010 is $\approx 15\%$ higher than the Chl-based model ($40\ Pg\ C\ y^{-1}$).

Friedrichs et al. (2009) assessed the uncertainties of primary production estimates for a wide range of satellite ocean color-based and biogeochemical ocean general circulation models. We compare our PP results with in-situ observations for the tropical Pacific Ocean used by *Friedrichs et al. (2009)*. Our estimations were obtained by forcing the model with the same environmental data set (Sea Surface Temperature (SST), Chl, photosynthetically active radiation (PAR)) reported in *Friedrichs et al. (2009, Supplementary information)*. Nitrogen was calculated for the same geographical positions as the observations using the algorithm of *Arteaga et al. (2015)*. Z_{eu} was calculated using the Chl concentration reported in the environmental data set. The correlation coefficient (r) between our modelled and in-situ PP is 0.54 (Fig. 4a), similar to the average correlation obtained for all models evaluated in *Friedrichs et al. (2009)* ($r = 0.51$), and slightly better than what was obtained for the CbPM with the same validation data set ($r = 0.36$). Our model performs well within the range of the best models evaluated by *Friedrichs et al. (2009)* (Fig. 4 and Table S.2). The skill assessment of our model is summarized in the Taylor diagram on Fig. 4b and Table S.2 (see Supplementary information). For this validation exercise we use the same parameter set presented in Table S.1, and global α and A_0 values according to Eqs. (3) and (4) used for our global growth rates and Chl:C estimates

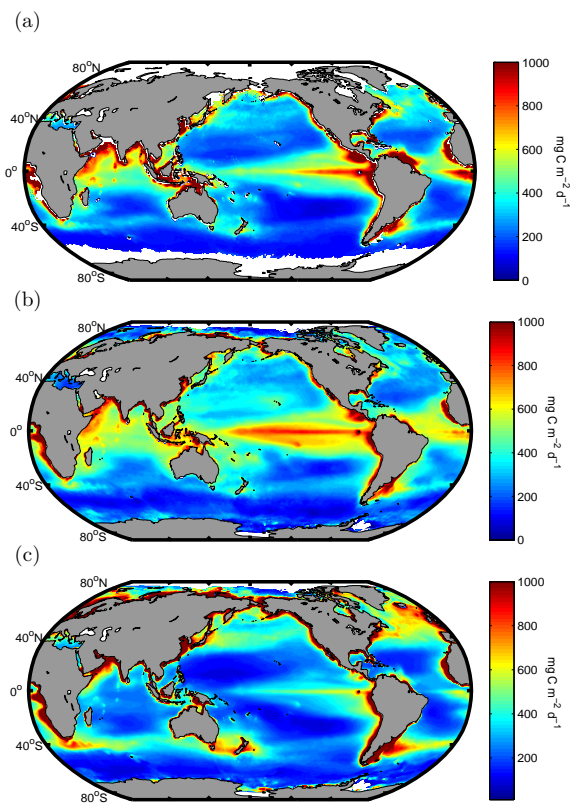


Figure 3: Global primary production rates obtained with (a) the Optimality-based physiological model (*Pahlow et al., 2013*), (b) the Carbon-based production model (*Westberry et al., 2008*), and (c) the Vertical Generalized Production Model (*Behrenfeld and Falkowski, 1997b*). The panels represent averages for the 6 year period 2005–2010.

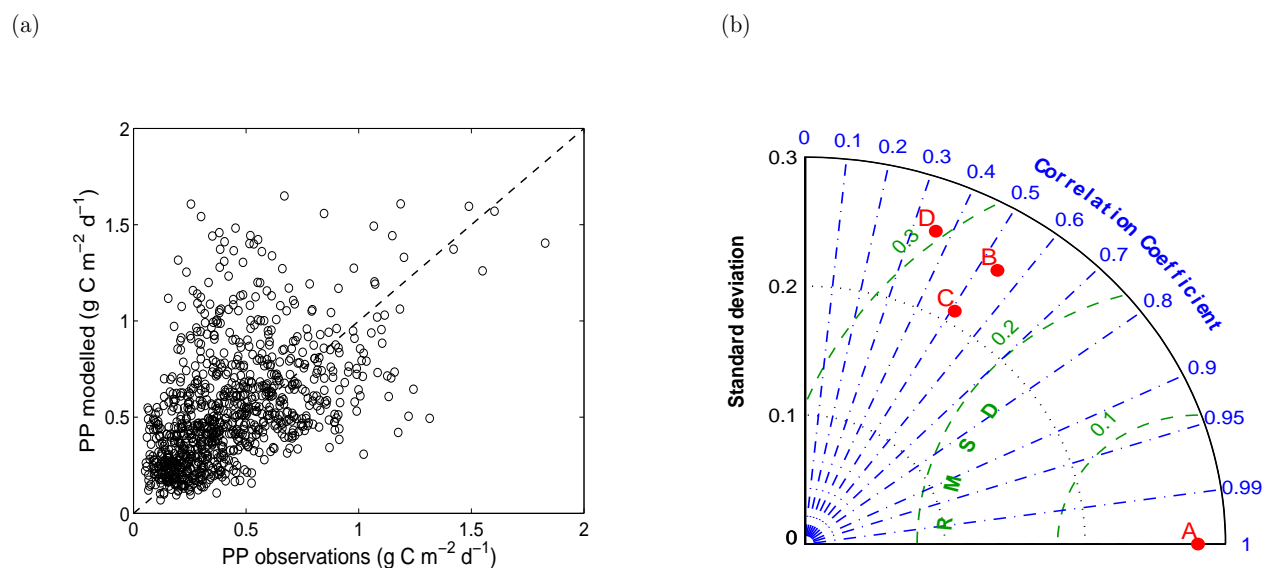


Figure 4: (a) Scatter plot of observed vs. modelled primary production (PP) calculated with the optimality-based physiological model (*Pahlow et al., 2013*). Observations are for the tropical Pacific Ocean from *Friedrichs et al. (2009)*. (b) Taylor diagram of $\log_{10}(\text{PP})$. The standard deviation is given as the distance from the origin. The correlation between modelled and observed PP is represented by the azimuth angle (dashed-blue lines). Dashed green lines are centered-pattern RMSD isolines. The red dots represent observed (A), and modelled PP: (B) Optimality-based (this work), (C) average of all models evaluated in *Friedrichs et al. (2009)*, (D) (*Westberry et al., 2008*). See supplementary information for details of the calculation of the statistical metrics.

Phytoplankton carbon

We estimate global phytoplankton carbon as the product of our predicted C:Chl and observations of surface Chl from the MODIS sensor (Fig. 5a). Satellite-based observations of Chl provide valuable information on the relative patterns of phytoplankton biomass in the global surface ocean. The incorporation of a physiologically-derived C:Chl ratio allows a more accurate description of the distribution of phytoplankton carbon-biomass in the surface ocean.

Estimated phytoplankton C (phyto-C) is highest in coastal regions, where it reaches concentrations of about 30 mg C m^{-3} . The Caribbean and Indian Sea also show high phyto-C concentrations throughout the year. Despite high production rates, phyto-C concentrations in the tropical Pacific Ocean are not as high as in the Atlantic and Indian Oceans. During the northern summer (April–September), high phyto-C concentrations are found in high northern latitudes, particularly over the Atlantic Ocean. The opposite pattern is found during the austral summer, where phyto-C concentrations are high particularly near New Zealand and the Atlantic coast of southern South America. This is the result of differences in Chl concentration and the C:Chl ratio between the two hemispheres (Fig. 5b), with C:Chl being smaller in the winter hemisphere due to photoacclimation by phytoplankton cells (*Geider, 1987; MacIntyre et al., 2000*). It is important to mention that, although our model does not account for the physiological effects of iron on phytoplankton, iron limitation is implicitly included to some degree by using Chl satellite observations. Iron deprivation should reduce phytoplankton growth rates and Chl synthesis, hence increasing C:Chl. While accounting for iron dynamics would result in higher Phytoplankton C concentrations, the net effect of iron limitation on our modelled PP rates is not entirely clear.

We use independent satellite-based estimates of total surface POC (*Dufort-Gaurier et al., 2010*) (Fig. 5c) to assess the contribution of phytoplankton carbon to the total POC pool (Fig. 5d & e). According to these estimates, phytoplankton comprises between 30 and 70 % of total POC in the tropical ocean, with highest values in the oligotrophic subtropical gyres.

The derived phytoplankton contribution to POC has an inverse pattern with respect to total POC concentration. Phytoplankton dominates the oligotrophic areas of the ocean between 40° North and South, while its share to the total POC decreases towards the poles in both hemispheres, where phyto-C constitutes between 10 and 30% of total POC (Fig. 5d & e). The most pronounced seasonal variation in relative phytoplankton biomass occurs in the Pacific Ocean. Phytoplankton C is higher in the North Pacific during boreal summer months (April–September), and higher south of the equator during winter months (October–March). The contribution of phyto-C in the Southern Ocean is fairly constant during both summer and winter. According

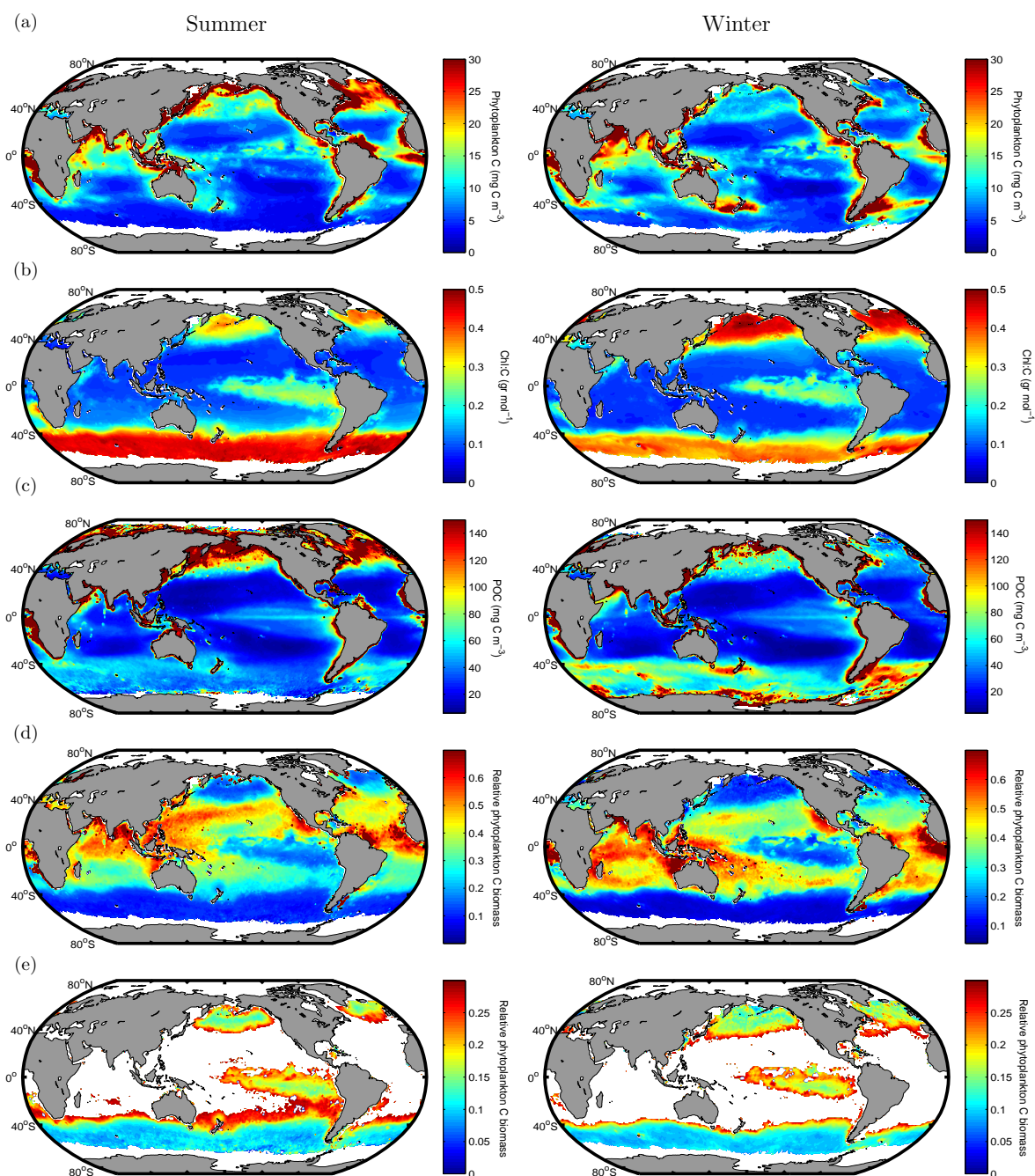


Figure 5: (a) Phytoplankton carbon concentration obtained as the product of monthly global Chl:C (b) as predicted by the model of *Pahlow et al. (2013)* and monthly surface Chl observations from MODIS. (c) Surface POC estimated as in *Dufort-Gaurier et al. (2010)*. (d) Relative contribution of phytoplankton to total surface POC. (e) Relative contribution of phytoplankton up to 0.3 of total POC. Each panel represents the average of the 6 year period 2005–2010. Left panels are summer means (April–September) for the period 2005–2010. Right panels are winter means (October–March).

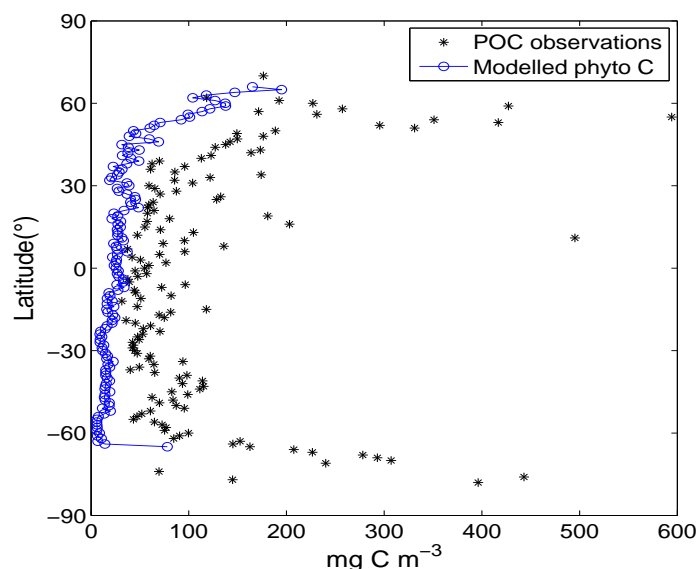


Figure 6: Latitudinal patterns in modelled phytoplankton C (blue dotted line) and POC surface observations (top 10 m, black asterisks) from (Martiny *et al.*, 2014).

to our analysis, the Southern Ocean also has the lowest contribution of phytoplankton-C ($\approx 10\%$) throughout the global surface ocean. However, this contribution might be higher if iron limitation was considered.

We compare the latitudinal gradient of our phyto-C estimates with in-situ POC observations of the surface ocean (top 10 m) obtained from (Martiny *et al.*, 2014) (Fig. 6). POC observations and estimates of phyto-C are larger at high latitudes and decrease towards the equator. Similar to Fig. 5c,d, the relative decrease of POC towards tropical regions is greater than that of phyto-C, implying that the phyto-C compartment of total POC is larger in low latitudes. Our modelled phyto-C does not show a strong latitudinal increase towards southern latitudes, likely as result of the neglect of iron limitation.

The contribution of phytoplankton to total oceanic carbon provides some information about patterns of the trophic structure of marine ecosystems. Our results suggest that oligotrophic areas of the ocean are dominated by autotrophs with little biomass contained in heterotrophs (Williams *et al.*, 2013). A data compilation on zooplankton-C retrieved from the World Ocean Atlas website http://www.nodc.noaa.gov/OC5/WOA01/1d_woa01.html suggests that the zooplankton contribution to POC is generally anti correlated to that of phytoplankton (Fig. S.1). While the global coverage of the observations is sparse, there seems to be an increase in zooplankton-C contribution towards the tropical Pacific, which is opposite to the pattern in phytoplankton biomass. Global rates of POC export tend to be higher in high latitudes and lower in low

latitudes (*Henson et al., 2011*). Nutrient limitation of the autotrophic community and temperature controls on heterotrophic organisms are considered the main drivers of the global patterns in export production rates (*Laws et al., 2000*). As global climate change leads to warmer surface waters and changes in the relative distribution of nutrients and light (*Riebesell et al., 2009*), POC export patterns might change as result of the expansion of oligotrophic areas in the ocean (*Polovina et al., 2009*). Our global estimations of phytoplankton carbon and relative contribution to total POC present a first-hand approach to identify such changes and detect shifts in patterns of global marine habitats.

Methods

We employ the optimality-based model of phytoplankton growth to obtain 1° global monthly growth rates and phytoplankton C:Chl estimations for the period January, 2005–December, 2010 (Supplementary information). The model is forced with monthly sea surface temperature (SST), photosynthetically active radiation (PAR), and nitrate inputs. Monthly SST inputs are obtained from the Moderate Resolution Imaging Spectroradiometer (MODIS) <http://oceancolor.gsfc.nasa.gov>. PAR is included as the “Median Mixed Layer Light Level” (I_g) which approximates the average light intensity experienced by phytoplankton cells in the surface mixed layer (I_g , *Behrenfeld et al., 2005*),

$$I_g = \frac{1}{D} \cdot \text{PAR} \cdot e^{-K490 \cdot \frac{\text{MLD}}{2}} \quad (6)$$

I_g depends on the day-length-fraction (D , given by the time of the year), surface PAR ($\text{E m}^{-2} \text{ d}^{-1}$), the diffusive light attenuation coefficient estimated at 490 nm ($K490$) (m^{-1}) and mixed layer Depth (MLD) (m). Monthly MLD outputs are obtained from the Ocean Productivity site of Oregon State University (<http://science.oregonstate.edu/ocean.productivity/index.php>). Monthly nitrate inputs are obtained from multiple local linear regressions of SST, MLD, and Chl employing the algorithm described in *Arteaga et al. (2015)*. All inputs variable are re-gridded to a 1° spatial resolution grid.

Light and nutrient (nitrogen) limitation is initially derived from the optimality-based model using the parameter set in Table S.1, following Eqs. (1) and (2). The limitation indices are employ to allocate multiple phytoplankton species adapted to different light and nitrogen conditions using Eqs. (3) and (4). We run the physiological phytoplankton model one more time employing the α and A_0 maps obtained above, and estimate global phytoplankton growth rates and Chl:C ratio. Primary production is calculated as the product of modelled growth rates, Chl:C, and satellite-based Chl concentrations from the MODIS sensor,

using Eq. (5). Monthly estimations of surface Chl are obtained from <http://oceancolor.gsfc.nasa.gov>. We compare our PP rates with estimates from the CbPM (*Westberry et al., 2008*) and VGPM models (*Behrenfeld and Falkowski, 1997b*). Monthly VGPM and CbPM PP outputs are obtained from <http://science.oregonstate.edu/ocean.productivity/index.php>.

Phytoplankton carbon (Phyto-C) is estimated as:

$$\text{Phyto-C} = (\text{C:Chl})_m \cdot \text{Chl}_{\text{MODIS}} \quad (7)$$

where $(\text{C:Chl})_m$ is the predicted C:Chl ratio (mol mg^{-1}), and $\text{Chl}_{\text{MODIS}}$ is the Chl concentration (mg Chl m^{-3}) estimated from the MODIS sensor. Surface POC estimates are obtained as described in *Dufort-Gaurier et al. (2010)* (POC_{sat}) by the average of two methods: Based on an empirical power-law built between surface POC and the blue-to-green ratio of the remote-sensing reflectance (*Stramski et al., 2008*); and based on deriving surface POC from a remotely sensed inherent optical property (*Loisel et al., 2002*). The relative contribution of phytoplankton carbon to total POC (Relaphy-C) is estimated as:

$$\text{Relaphy-C} = \frac{\text{Phyto-C}}{\text{POC}_{\text{sat}}} \quad (8)$$

References

- Armstrong, R. (2006), Optimality-based modeling of nitrogen allocation and photoacclimation in photosynthesis, *Deep Sea Research Part II: Topical Studies in Oceanography*, 53(5-7), 513–531, doi:10.1016/j.dsr2.2006.01.020.
- Arteaga, L., M. Pahlow, and A. Oschlies (2014), Global patterns of phytoplankton nutrient and light colimitation inferred from an optimality-based model, *Global Biogeochemical Cycles*, 28(7), 648–661, doi:10.1002/2013GB004668.
- Arteaga, L., M. Pahlow, and A. Oschlies (2015), Global monthly sea-surface nitrate fields estimated from remotely sensed sea-surface temperature, chlorophyll, and modelled mixed layer depth, *Geophysical Research Letters*, doi:10.1002/2014GL062937.
- Behrenfeld, M. J., and P. G. Falkowski (1997a), A consumer’s guide to phytoplankton primary productivity models, *Limnology and Oceanography*, 42(7), 1479–1491, doi:10.4319/lo.1997.42.7.1479.

- Behrenfeld, M. J., and P. G. Falkowski (1997b), Photosynthetic rates derived from satellite-based chlorophyll concentration, *Limnology and Oceanography*, *42*(1), 1–20, doi:10.4319/lo.1997.42.1.0001.
- Behrenfeld, M. J., E. Boss, D. A. Siegel, and D. M. Shea (2005), Carbon-based ocean productivity and phytoplankton physiology from space, *Global Biogeochemical Cycles*, *19*, GB1006, doi:10.1029/2004GB002299.
- Campbell, J., D. Antoine, R. Armstrong, K. Arrigo, W. Balch, R. Barber, M. Behrenfeld, R. Bidigare, J. Bishop, M.-E. Carr, W. Esaias, P. Falkowski, N. Hoepffner, R. Iverson, D. Kiefer, S. Lohrenz, J. Marra, A. Morel, J. Ryan, V. Vedernikov, K. Waters, C. Yentsch, and J. Yoder (2002), Comparison of algorithms for estimating ocean primary production from surface chlorophyll, temperature, and irradiance, *Global Biogeochemical Cycles*, *16*(3), 9–1–9–15, doi:10.1029/2001GB001444.
- Carr, M., M. Friedrichs, M. Schmeltz, M. Noguchiaita, D. Antoine, K. Arrigo, I. Asanuma, O. Aumont, R. Barber, and M. Behrenfeld (2006), A comparison of global estimates of marine primary production from ocean color, *Deep Sea Research Part II: Topical Studies in Oceanography*, *53*(5-7), 741–770, doi:10.1016/j.dsr2.2006.01.028.
- Cloern, J. E., C. Grenz, and L. Videgar-Lucas (1995), An empirical model of the phytoplankton chlorophyll:carbon ratio—the conversion factor between productivity and growth rate, *Limnology and Oceanography*, *40*(7), 1313–1321, doi:10.4319/lo.1995.40.7.1313.
- Duarte, C. M., and J. Cebrian (1996), The fate of marine autotrophic production, *Limnology and Oceanography*, *41*(8), 1758–1766, doi:10.4319/lo.1996.41.8.1758.
- Dufort-Gaurier, L., H. Loisel, D. Dessailly, K. Nordkvist, and S. Alvain (2010), Estimates of particulate organic carbon over the euphotic depth from in situ measurements. application to satellite data over the global ocean, *Deep Sea Research Part I: Oceanographic Research Papers*, *57*(3), 351 – 367, doi:http://dx.doi.org/10.1016/j.dsr.2009.12.007.
- Eppley, R. W. (1972), Temperature and phytoplankton growth in the sea, *Fishery Bulletin*, *70*(4), 1063–1085.
- Field, C. B. (1998), Primary Production of the Biosphere: Integrating Terrestrial and Oceanic Components, *Science*, *281*(5374), 237–240, doi:10.1126/science.281.5374.237.
- Francois, R., S. Honjo, R. Krishfield, and S. Manganini (2002), Factors controlling the flux of organic carbon to the bathypelagic zone of the ocean, *Global Biogeochemical Cycles*, *16*(4), 34–1–34–20, doi:10.1029/2001GB001722.

- Friedrichs, M. A., M.-E. Carr, R. T. Barber, M. Scardi, D. Antoine, R. A. Armstrong, I. Asanuma, M. J. Behrenfeld, E. T. Buitenhuis, F. Chai, J. R. Christian, A. M. Ciotti, S. C. Doney, M. Dowell, J. Dunne, B. Gentili, W. Gregg, N. Hoepffner, J. Ishizaka, T. Kameda, I. Lima, J. Marra, F. Mlin, J. K. Moore, A. Morel, R. T. O'Malley, J. O'Reilly, V. S. Saba, M. Schmeltz, T. J. Smyth, J. Tjiputra, K. Waters, T. K. Westberry, and A. Winguth (2009), Assessing the uncertainties of model estimates of primary productivity in the tropical pacific ocean, *Journal of Marine Systems*, 76, 113 – 133, doi:10.1016/j.jmarsys.2008.05.010.
- Geider, R. J. (1987), Light and temperature dependence of the carbon to chlorophyll ratio in microalgae and cyanobacteria: Implications for physiology and growth of phytoplankton, *New Phytologist*, 106(1), 1–34, doi:10.1111/j.1469-8137.1987.tb04788.x.
- Geider, R. J., T. Platt, and J. Raven (1986), Size dependence of growth and photosynthesis in diatoms: a synthesis, *Marine Ecology. Progress Series*, 30, 93–104.
- Geider, R. J., H. L. MacIntyre, and T. Kana (1998), A dynamic regulatory model of phytoplanktonic acclimation to light, nutrients, and temperature, *Limnology and Oceanography*, 43(4), 679–694, doi:10.4319/lo.1998.43.4.0679.
- Henson, S. A., R. Sanders, E. Madsen, P. J. Morris, F. Le Moigne, and G. D. Quartly (2011), A reduced estimate of the strength of the ocean's biological carbon pump, *Geophysical Research Letters*, 38, L04,606, doi:10.1029/2011GL046735.
- Laws, E. A., P. G. Falkowski, W. O. Smith, H. Ducklow, and J. J. McCarthy (2000), Temperature effects on export production in the open ocean, *Global Biogeochemical Cycles*, 14(4), 1231–1246, doi:10.1029/1999GB001229.
- Loisel, H., J.-M. Nicolas, P.-Y. Deschamps, and R. Frouin (2002), Seasonal and inter-annual variability of particulate organic matter in the global ocean, *Geophysical Research Letters*, 29(24), 49–1–49–4, doi:10.1029/2002GL015948.
- MacIntyre, H. L., T. M. Kana, and R. J. Geider (2000), The effect of water motion on short-term rates of photosynthesis by marine phytoplankton., *Trends in plant science*, 5(1), 12–7, doi:10.1016/S1360-1385(99)01504-6.
- Martiny, A. C., J. A. Vrugt, and M. W. Lomas (2014), Concentrations and ratios of particulate organic carbon, nitrogen, and phosphorus in the global ocean, *Scientific Data*, 1, doi:10.1038/sdata.2014.48.

- Morel, A., and J.-F. Berthon (1989), Surface pigments, algal biomass profiles, and potential production of the euphotic layer: Relationships reinvestigated in view of remote-sensing applications, *Limnology and Oceanography*, *34*(8), 1545–1562, doi:10.4319/lo.1989.34.8.1545.
- Pahlow, M. (2005), Linking chlorophyll-nutrient dynamics to the Redfield N:C ratio with a model of optimal phytoplankton growth, *Marine Ecology Progress Series*, *287*, 33–43, doi:10.3354/meps287033.
- Pahlow, M., and A. Oschlies (2009), Chain model of phytoplankton P, N and light colimitation, *Marine Ecology Progress Series*, *376*, 69–83, doi:10.3354/meps07748.
- Pahlow, M., H. Dietze, and A. Oschlies (2013), Optimality-based model of phytoplankton growth and diazotrophy, *Marine Ecology Progress Series*, *489*, 1–16, doi:10.3354/meps10449.
- Polovina, J. J., E. A. Howell, and M. Abecassis (2009), Ocean’s least productive waters are expanding, *Geophysical Research Letters*, *35*, L03,618, doi:10.1029/2007GL031745.
- Raven, J. a., and P. G. Falkowski (1999), Oceanic sinks for atmospheric CO₂, *Plant, Cell and Environment*, *22*(6), 741–755, doi:10.1046/j.1365-3040.1999.00419.x.
- Riebesell, U., A. Krtzinger, and A. Oschlies (2009), Sensitivities of marine carbon fluxes to ocean change, *Proceedings of the National Academy of Sciences*, *106*(49), 20,602–20,609, doi:10.1073/pnas.0813291106.
- Smith, S. L., M. Pahlow, A. Merico, and K. W. Wirtz (2011), Optimality-based modeling of planktonic organisms, *Limnology and Oceanography*, *56*(6), 2080–2094, doi:10.4319/lo.2011.56.6.2080.
- Sterner, R. W., and J. J. Elser (2002), *Ecological stoichiometry: the biology of elements from molecules to the biosphere*, Princeton University Press.
- Stramski, D., R. A. Reynolds, M. Babin, S. Kaczmarek, M. R. Lewis, R. Röttgers, A. Sciandra, M. Stramska, M. S. Twardowski, B. A. Franz, and H. Claustre (2008), Relationships between the surface concentration of particulate organic carbon and optical properties in the eastern south pacific and eastern atlantic oceans, *Biogeosciences*, *5*(1), 171–201, doi:10.5194/bg-5-171-2008.
- Westberry, T., M. J. Behrenfeld, D. A. Siegel, and E. Boss (2008), Carbon-based primary productivity modeling with vertically resolved photoacclimation, *Global Biogeochemical Cycles*, *22*, GB2024, doi:10.1029/2007GB003078.

Williams, P. J. l. B., P. D. Quay, T. K. Westberry, and M. J. Behrenfeld (2013), The oligotrophic ocean is autotrophic, *Annual Review of Marine Science*, 5(1), 535–549, doi:10.1146/annurev-marine-121211-172335, pMID: 22809190.

Supplementary information

Determination of phytoplankton growth rate

In order to calculate growth rates we employ the optimality-based model of *Pahlow et al. (2013)*. This model is based on the physiological roles of nitrogen and phosphorus within the internal compartments of a phytoplankton cell. Nitrogen is associated with enzyme activity and is directly linked with phytoplankton growth, acting as the main limiting nutrient. Phosphorus constrains nitrogen assimilation in the ribosomes, and thereby limits nitrogen acquisition. However, a previous study with this optimality-based model carried out by *Arteaga et al. (2014)*, identified that phosphorus has a secondary limiting effect on phytoplankton growth in the global ocean. Hence, phosphorus limitation has been shut down in the current analysis, and nutrient limitation has been restricted only to nitrogen.

Phytoplankton growth is described as the difference between carbon fixation (V^C) and respiration (R),

$$\mu = V^C - R \quad (\text{S.1})$$

V^C is a function of the nitrogen cell-quota (Q^N), the potential CO_2 fixation rate (V_0^C), and photosynthetically active radiation (PAR). PAR is used to quantify the median mixed layer light level, I_g (Eq. 6). The effect of light limitation is estimated by the degree of light saturation of the cellular light-harvesting apparatus, S_I (*Pahlow, 2005*).

$$S_I = 1 - e^{-\frac{\alpha I_g \hat{\theta}^C}{V_0^C}} \quad (\text{S.2})$$

where α is the light absorption coefficient, V_0^C is the potential C fixation rate, and $\hat{\theta}^C$ is the chlorophyll to carbon ratio of the chloroplast.

Carbon-fixation rate is then defined as,

$$V^C = V_0^C \left(1 - \frac{Q_s^N}{Q^N} - f_V\right) S_I \quad (\text{S.3})$$

where f_V is the fraction of cellular nitrogen allocated for nutrient acquisition, and Q_s^N represents cellular

nitrogen bound in structural protein. Respiration comprises the cost of photosynthesis (R^{Chl}) and the cost of nitrogen assimilation ($\zeta^{\text{N}}V^{\text{N}}$) assumed to be proportional to nitrogen assimilation (V^{N}),

$$R = \zeta^{\text{N}}V^{\text{N}} + R^{\text{Chl}} \quad (\text{S.4})$$

nitrogen allocated for nutrient acquisition ($f_V Q^{\text{N}}$) is divided between dissolved inorganic nitrogen and dissolved inorganic phosphorus acquisition via another allocation factor (f_{N}):

$$V^{\text{N}} = f_V f_{\text{N}} V_*^{\text{N}} \quad V^{\text{P}} = f_V (1 - f_{\text{N}}) V_*^{\text{P}} \quad (\text{S.5})$$

where V_*^{N} and V_*^{P} are potential rates of N and P uptake as functions of potential uptake rates, V_0^{N} and V_0^{P} , and affinity, A_0 .

The allocation factors f_V and f_{N} are calculated to maximize net balanced growth rate.

Temperature dependence

Since the original model (*Pahlow et al., 2013*) does not include temperature, we introduced a temperature dependence (*Eppley, 1972*) of the maximum rate parameters, in the same manner as in *Arteaga et al. (2014)*:

$$V_0^{\text{C}} = V_0^{\text{N}} = V_0^{\text{P}} = 1.4 * 1.066^{\text{TEMP}} \quad (\text{S.6})$$

For this study, a temperature dependence has also been included for the respiration cost of Chl maintenance ($R_{\text{M}}^{\text{Chl}}$):

$$R_{\text{M}}^{\text{Chl}} : 0.028 * 1.086^{\text{TEMP}} \quad (\text{S.7})$$

Chlorophyll to carbon ratio

The Chl:C ratio is constrained by the effects of nutrient and light limitation on phytoplankton growth. As explained in *Arteaga et al. (2014)*, the Chl:C ratio is regulated to maximize the energy available for nitrogen assimilation. The first step to calculate the Chl:C ratio is the determination of the Chl:C ratio of the chloroplasts:

$$\hat{\theta}^{\text{C}} = \frac{1}{\zeta^{\text{Chl}}} + \frac{V_0^{\text{C}}}{\alpha I_g} \left\{ 1 - W_0 \left[\left(1 + \frac{R_{\text{m}}^{\text{Chl}}}{D V_0^{\text{C}}} \right) e^{\frac{\alpha I_g}{V_0^{\text{C}} \zeta^{\text{Chl}} + 1}} \right] \right\} \quad \text{if } I_g > I_{g_0} \quad (\text{S.8})$$

$$\hat{\theta}^C = 0 \quad \text{if} \quad I_g \leq I_{g_0}$$

where ζ^{Chl} is the cost of photosynthesis, R_m^{Chl} is the cost of Chl maintenance, and W_0 is the 0-branch the Lambert-W function, and:

$$I_{g_0} = \frac{\zeta^{\text{Chl}} R_m^{\text{Chl}}}{D\alpha} \quad (\text{S.9})$$

is the threshold irradiance for chlorophyll synthesis.

The Chl:C ratio of the entire cell is then obtained as a direct result of N and light limitation, represented by Q^{N} and $\hat{\theta}^C$ respectively,

$$\text{Chl:C} = \hat{\theta}^C \left(1 - \frac{Q_s^{\text{N}}}{Q^{\text{N}}} - f_v \right) \quad (\text{S.10})$$

where Q_s^{N} is the partial N quota bound in structural protein, and f_v is the fraction of Q^{N} allocated for nutrient acquisition (*Pahlow et al., 2013*).

Skill assessment

The skill of our model is assessed by comparing our PP estimations with observations of the tropical Pacific Ocean (*Friedrichs et al., 2009*). We computed the same metrics as in *Friedrichs et al. (2009)*. Total root mean square difference (RMSD) is calculates as:

$$\text{RMSD} = \sqrt{\frac{1}{N} \sum_{i=1}^n \Delta^2(i)} \quad (\text{S.11})$$

Model-data misfit in \log_{10} space (Δ) is defined as,

$$\Delta(i) = \lg(\text{PP}_m(i)) - \lg(\text{PP}_d(i)) \quad (\text{S.12})$$

RMSD is composed of two components, the bias (B), and the centered-pattern RMSD (RSMD_{cp}),

$$\text{RMSD}^2 = B^2 + \text{RSMD}_{\text{cp}}^2, \quad (\text{S.13})$$

The bias and RSMD_{cp} provide measures of how well the mean and variability are modeled, respectively (*Friedrichs et al., 2009*),

$$B = \overline{\lg(\text{PP}_m)} - \overline{\lg(\text{PP}_d)} \quad (\text{S.14})$$

$$\text{RMSD} = \sqrt{\frac{1}{N} \sum_{i=1}^n \left\{ \left[\lg(\text{PP}_m(i)) - \overline{\lg(\text{PP}_m)} \right] - \left[\lg(\text{PP}_d(i)) - \overline{\lg(\text{PP}_d)} \right] \right\}^2} \quad (\text{S.15})$$

F_{med} is a non-dimensional inverse transformed value for bias, used to translate the above quantities obtained in decades of \log_{10} ,

$$F_{\text{med}} = 10^B \quad (\text{S.16})$$

if $F_{\text{med}} = 2.0$ the median value of $\text{PP}_m(i)$ is a factor of two larger than the median value of $\text{PP}_d(i)$; if $F_{\text{med}} = 0.5$, the median value of $\text{PP}_m(i)$ is a factor of two smaller than $\text{PP}_d(i)$ (*Campbell et al., 2002; Friedrichs et al., 2009*).

Sensitivity analysis

General sensitivity

We conducted several sensitivity analyses in order to evaluate the effect of each model parameter presented in Table S.1 on the estimation of global primary production rates. We performed 12 additional calculations of global PP for the year 2005, incrementing each of the 6 non-temperature dependent parameters of the model (Table S.1) by 5 and 50%. The results of these calculations are summarized in Table S.3. Overall, changes in the parameters have little effect in the computation of global annual PP rates. Only an increase in the Chl-specific light absorption coefficient (α) has a noticeable effect when it is rose by 50%, resulting in an increase of 30% in mean global annual PP. This is due to a quadratic effect of α on the carbon-based production rate. On one hand, an increase in α results in a more efficient photochemical compartment, which allows the cell to expend less energy on the production of Chl, thus, lowering the Chl:C ratio. On the other hand, a higher Chl light absorption decreases the overall light limitation experienced by the cell, increasing S_I (Eq. S.2), the carbon fixation rate (Eq. S.3) and net growth rate of the cell (Eq. S.1).

An increase in A_0 has opposite effects on the cell. It increases nutrient acquisition, which stimulates the net growth rate (μ), but at the same time allows for a higher synthesis of Chl, which increases the Chl:C ratio. Similar dynamics occur with Q_s^N . As phosphorus limitation is not included in this analysis the effects of Q_0^P are negligible. An increment in the cost of photosynthesis (ζ^{Chl}) results in a lower Chl:C which translates into higher PP, particularly for a 50% increment in ζ^{Chl} . ζ^N has a direct effect on the assimilation of carbon by accentuating nitrogen limitation, hence the increase of this parameter results in a slight decrease in global PP.

Sensitivity of A_0 and α parametrization

We performed a second set of analyses in order to determine the sensitivity of global annual PP rates for 2005, to changes in the parameters of the nutrient and light dependent functions of A_0 and α . The original slope and offset of α ($a_\alpha = 1$ and $b_\alpha = 0.3$) were increased by 10% to $a_\alpha = 1.1$ and $b_\alpha = 0.33$, while for A_0 we decreased the original slope and increased its offset by 10% (from $a_A = 100$ to $a_A = 90$ and from $b_A = 40$ to $b_A = 44$, respectively). The highest relative changes on PP were obtained when the parameters of α were altered simultaneously (Table S.4, sensitivity test 1–4). This points to α as the parameter to which the model is most sensitive, as already evidenced in our initial sensitivity analysis. This change is maximized when a_A is also reduced from 100 to 90, as a lower A_0 results in a higher Chl:C ratio. When α is unaltered, changes in PP are only as high as 0.05 %.

Table S.1: Model parameters values and description.

Symbol	Value	Description
A_0	100	Potential nutrient affinity ($\text{m}^3 \text{mol}^{-1} \text{d}^{-1}$)
α	0.8	Chl-specific light affinity ($\text{m}^2 \text{E}^{-1} \text{mol} (\text{g Chl})^{-1}$)
Q_s^N	0.025	Partial N quota bound in structural protein (mol N mol C^{-1})
Q_0^P	0.0018	Subsistence P quota (mol P mol C^{-1})
ζ^{Chl}	0.6	Cost of photosynthesis (mol mol^{-1})
ζ^N	0.6	Cost of N assimilation (mol mol^{-1})
V_0^C, V_0^N, V_0^P	$1.4 \times 1.066^{\text{TEMP}}$	Potential C, N, and P acquisition rates
R_M^{Chl}	$0.028 \times 1.086^{\text{TEMP}}$	Cost of Chl maintenance

Table S.2: Summary of model skill assessment for primary production. Statistical metrics are given for our optimality-based estimations (Opt-based) using the parameter set in Table S.1, the C-based model from *Westberry et al. (2008)* (CbPM), as well as averages and standard deviations for each metric over all models evaluated in *Friedrichs et al. (2009)* (All).

	Bias	F_{med}	RMSD_{cp}	Total RMSD	Correlation	Standard deviation
Opt-based	0.11	1.29	0.25	0.27	0.54	0.25
CbPM	0.25	1.79	0.30	0.39	0.36	0.26
All	0.14 ± 0.02	1.38	0.25 ± 0.01	0.30 ± 0.01	0.51 ± 0.01	0.21 ± 0.01

Table S.3: Summary of sensitivity experiments: Change in mean annual primary production (PP in Pg C y^{-1}) for 2005 for an increase in the parameter value by 5 and 50%.

Parameter	Parameter value increased by 5%	Change in PP (%)	Parameter value increased by 50 %	Change in PP (%)
A_0 ($m^3 mol^{-1} d^{-1}$)	105	-0.03	150	-0.27
α ($m^2 E^{-1} mol (g Chl)^{-1}$)	0.84	4.0	1.2	28.4
Q_s^N ($mol N mol C^{-1}$)	0.03	-0.16	0.04	-1.9
Q_0^N ($mol P mol C^{-1}$)	0.002	7×10^{-4}	0.003	0.005
ζ^{Chl} ($mol mol^{-1}$)	0.6	0.8	0.9	6.4
ζ^N ($mol mol^{-1}$)	0.6	-0.2	0.9	-2.0

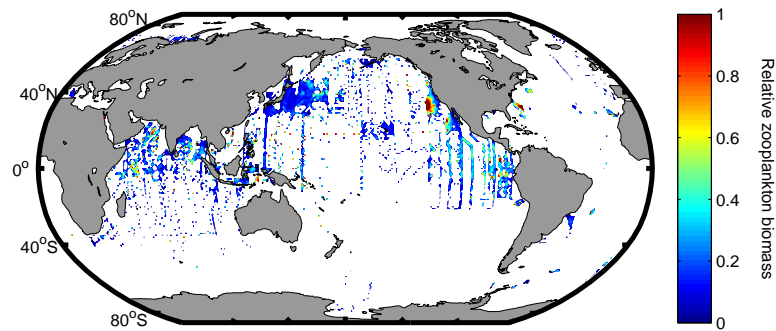


Figure S.1: Relative zooplankton carbon (C) contribution to total surface POC. Zooplankton C concentration was obtained from the World Ocean Atlas website http://www.nodc.noaa.gov/OC5/WOA01/1d_woa01.html, as a collection of all observations available. Relative zooplankton-C biomass was calculated using the mean of the full monthly POC data set (Dufort-Gaurier *et al.*, 2010) for 2005–20210.

Table S.4: Sensitivity of mean annual primary production (PP in Pg C yr⁻¹) for 2005 as a result of changes in the slopes (a_α and a_A) and offsets (b_α and b_A), respectively, of the light (α) and nutrient affinity (A_0) functions: Both a_α and b_α were increased by 10%, whereas for a_A was decreased and b_A was increased by 10%. A total of 15 sensitivity tests were performed covering all possible permutations. The respective 10% change for each component is indicated by “•”. “-” indicates that the original parameter value was kept the unaltered.

Sensitivity test	α slope	α offset	A_0 slope	A_0 offset	Change in PP (%)
Original	1	0.3	0.1	0.04	0
1	•	•	•	•	7.8
2	•	•	•	-	7.9
3	•	•	-	•	7.8
4	•	•	-	-	7.8
5	•	-	•	•	2.9
6	•	-	•	-	2.9
7	•	-	-	•	2.8
8	•	-	-	-	2.9
9	-	•	•	•	5.2
10	-	•	•	-	5.3
11	-	•	•	-	5.3
12	-	•	-	-	5.2
13	-	-	•	•	0.01
14	-	-	•	-	0.05
15	-	-	-	•	-0.03

2.4 Chapter 4: *Nitrogen cycling driven by organic matter export in the South Pacific oxygen minimum zone.*

Tim Kalvelage, Gaute Lavik, Phyllis Lam, Sergio Contreras, Lionel Arteaga, Carolin R. Löscher, Andreas Oschlies, Aurelién Paulmier, and Marcel M. M. Kuypers.

Published article: Kalvelage, T., G. Lavik, P. Lam, S. Contreras, L. Arteaga, C. R. Löscher, A. Oschlies, A. Paulmier, L. Stramma, and M. M. M. Kuypers (2013), Nitrogen cycling driven by organic matter export in the South Pacific oxygen minimum zone, *Nature Geoscience*, 6(3), 228–234, doi: 10.1038/ngeo1739

Nitrogen cycling driven by organic matter export in the South Pacific oxygen minimum zone

Tim Kalvelage¹, Gaute Lavik¹, Phyllis Lam¹, Sergio Contreras^{1†}, Lionel Arteaga², Carolin R. Löscher³, Andreas Oschlies², Aurélien Paulmier^{1†}, Lothar Stramma² and Marcel M. M. Kuypers^{1*}

Oxygen minimum zones are expanding globally, and at present account for around 20–40% of oceanic nitrogen loss. Heterotrophic denitrification and anammox—anaerobic ammonium oxidation with nitrite—are responsible for most nitrogen loss in these low-oxygen waters. Anammox is particularly significant in the eastern tropical South Pacific, one of the largest oxygen minimum zones globally. However, the factors that regulate anammox-driven nitrogen loss have remained unclear. Here, we present a comprehensive nitrogen budget for the eastern tropical South Pacific oxygen minimum zone, using measurements of nutrient concentrations, experimentally determined rates of nitrogen transformation and a numerical model of export production. Anammox was the dominant mode of nitrogen loss at the time of sampling. Rates of anammox, and related nitrogen transformations, were greatest in the productive shelf waters, and tailed off with distance from the coast. Within the shelf region, anammox activity peaked in both upper and bottom waters. Overall, rates of nitrogen transformation, including anammox, were strongly correlated with the export of organic matter. We suggest that the sinking of organic matter, and thus the release of ammonium into the water column, together with benthic ammonium release, fuel nitrogen loss from oxygen minimum zones.

Coastal upwelling of nutrient-rich deep water fuels high surface productivity at the eastern boundaries of (sub)tropical oceans. The resultant export of organic matter stimulates strong microbial respiration in the subsurface. Combined with poor ventilation, permanently O₂-deficient waters called oxygen minimum zones (OMZs) develop at mid-depths^{1,2}. Ongoing global expansion and intensification of OMZs will expectedly continue as anthropogenic pressures on marine environments grow^{3–5}.

Although constituting only ~1% (O₂ ≤ 20 μmol kg⁻¹) of global ocean volume⁶, OMZs have a profound impact on the oceanic nitrogen (N) balance as they account for ~20–40% of global oceanic N loss⁷. Ocean de-oxygenation might enlarge the ocean volume subject to N loss⁸, exacerbate N limitation of phytoplankton, and reduce the ocean's capacity to attenuate rising atmospheric carbon dioxide levels. Assessing the effects of expanding OMZs on the future ocean's nutrient balance, however, remains speculative, as biogeochemical models do not reproduce present-day global patterns of N loss^{9–11}. A major deficiency of those models seems to be the poor representation of coastal regions, whereas an increasing number of studies indicate that N loss in shelf OMZs (refs 12–14), coastal–offshore OMZ water mass exchange¹⁵ and OMZ–sediment interactions¹⁶ play more important roles in the overall N budget.

On the basis of the observed accumulations of nitrite (NO₂⁻) and associated N deficits, most N loss in OMZ waters has traditionally been attributed to heterotrophic denitrification^{17–19}, the step-wise reduction of nitrate (NO₃⁻) to gaseous dinitrogen (N₂). Recent studies have, however, often failed to detect significant denitrifying activity in OMZs; rather, anammox has more commonly been identified as a major N₂-forming pathway in these environments^{12–14,20}.

The regulation of N-loss activity including anammox is not fully understood. Anammox requires NH₄⁺ and NO₂⁻. Sources and sinks of both compounds have been identified in the OMZs, including aerobic NH₃ and NO₂⁻ oxidation, as well as anaerobic NO₃⁻ reduction to NO₂⁻ and dissimilatory NO₃⁻/NO₂⁻ reduction to NH₄⁺ (DNRA; refs 14,15,21,22). Surprisingly, O₂ sensitivity assays show that these processes in OMZ waters share a large overlapping range of O₂ concentrations (>0–20 μmol l⁻¹) in which they can co-occur, implying that within this range, controlling factors other than O₂ are more important^{23,24}. Enhanced autotrophic and heterotrophic N-cycling activity in the upper OMZ (refs 13,14,20,21), and generally elevated anammox rates usually measured in coastal versus offshore OMZs (ref. 6), suggest that N loss might ultimately be regulated by export production of organic matter.

To test this hypothesis, we conducted a large-scale survey of N-cycling rates, functional gene abundances, chlorophyll, nutrient and O₂ concentrations, as well as modelled export production, throughout the eastern tropical South Pacific (ETSP), one of the main OMZs in the world²⁵.

Dissolved inorganic nitrogen in the South Pacific OMZ

Consistent with past observations in the ETSP (refs 18,26), pronounced secondary NO₂⁻ maxima were found in the offshore OMZ between 10° S and 18° S (Supplementary Fig. S1), extending up to hundreds of kilometres westward with maximum concentrations of ~11 μmol l⁻¹. On the basis of the spatial distribution of measured O₂, the lower OMZ boundary occurred at ~600 m on average near the Peruvian shelf (Supplementary Figs S1 and S2). Henceforth, this is used as a depth cutoff to differentiate

¹Max Planck Institute for Marine Microbiology, 28195 Bremen, Germany, ²GEOMAR Helmholtz Centre for Ocean Research Kiel, 24105 Kiel, Germany,

³Institute for General Microbiology, 24118 Kiel, Germany. [†]Present addresses: Large Lakes Observatory, University of Minnesota Duluth, Minnesota 55812, USA (S.C.); Laboratoire d'Etudes en Géophysique et Océanographie Spatiales, UMR 5566, 18 Avenue Edouard Belin, 31401 Toulouse Cedex 9, France and Instituto del Mar del Perú (IMARPE), Esquina Gamarra y General Valle, S/N Chucuito, Lima, Peru (A.P.). *e-mail: mkuypers@mpi-bremen.de.

ARTICLES

NATURE GEOSCIENCE DOI: 10.1038/NNGEO1739

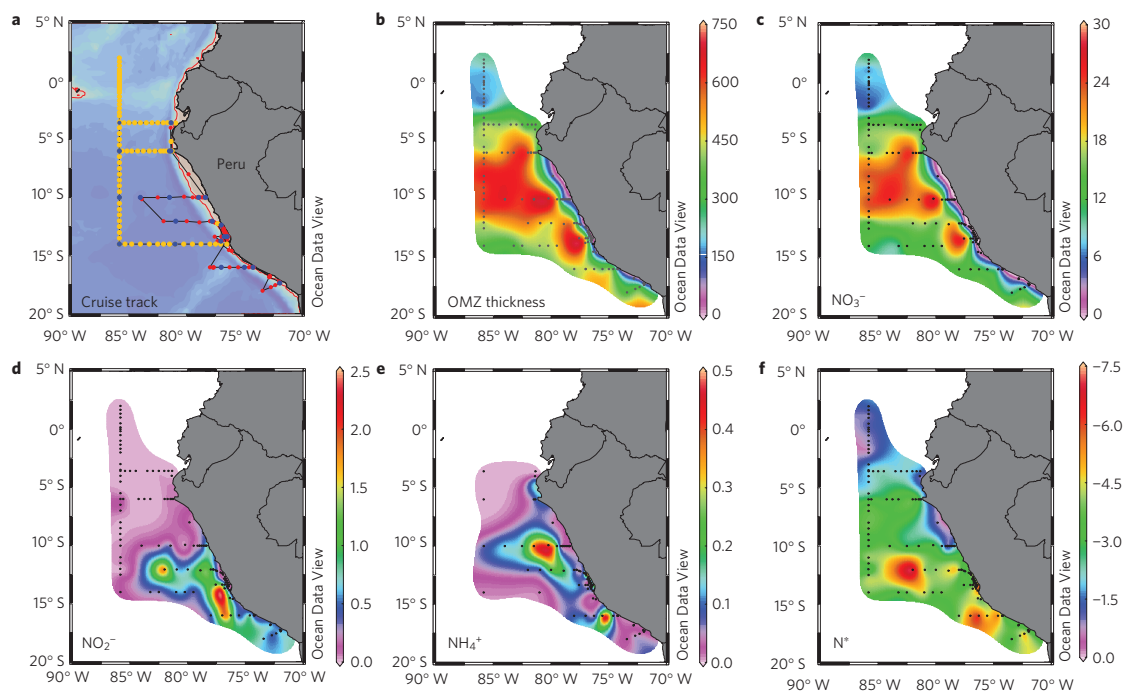


Figure 1 | Maps of sampling locations and nutrient distributions in the ETSP OMZ. **a**, Sampling sites during M77-3 (filled red circles) and M77-4 (filled yellow circles) and ^{15}N experimental stations (filled blue circles). **b**, Vertical extent of the OMZ (in m) as defined by $\text{O}_2 \leq 15 \mu\text{mol l}^{-1}$. **c–f**, Concentrations of NO_3^- , NO_2^- , NH_4^+ and N^* (in mol m^{-2}) integrated over the thickness of the OMZ. Red line in **a** denotes the 600 m isobath that was used to demarcate the coastal OMZ from the offshore OMZ.

coastal OMZ stations, where the OMZ is in direct contact with sediments and benthic N fluxes (<600 m), from all others that are defined as offshore OMZ stations. Integrated over the thickness of the OMZ (defined by $\text{O}_2 \leq 15 \mu\text{mol l}^{-1}$ where N-loss activity remains detectable in O_2 sensitivity assays²⁴; Fig. 1b and Supplementary Fig. S2), depth-integrated NO_2^- concentrations reached $>2 \text{ mol m}^{-2}$ in the offshore region (Fig. 1d). Concentrations of NH_4^+ were low ($<0.25 \mu\text{mol l}^{-1}$) throughout the OMZ, but could be $\geq 0.5 \mu\text{mol l}^{-1}$ over the shelf and near the upper OMZ boundary further offshore. Deeper in the offshore OMZ, plumes of elevated NH_4^+ concentrations ($\leq 3 \mu\text{mol l}^{-1}$) sometimes occurred (Supplementary Fig. S1), resulting in high depth-integrated values (Fig. 1e).

Offshore OMZs were characterized by severe N deficits, expressed here as strongly negative N^* with minima from $-8 \mu\text{mol N l}^{-1}$ at 3.58°S down to $-32 \mu\text{mol N l}^{-1}$ at 16°S . Depth-integrated values of N^* (Fig. 1f) and NO_2^- (Fig. 1d) were significantly correlated (Spearman $R = -0.61$, $P \leq 0.001$). The southward intensification of both NO_2^- maxima and N^* minima probably reflects the accumulated effects of time-integrated microbial activity in OMZ waters that advect poleward along the continental slope with the Peru–Chile Undercurrent^{27,28}. Over the Peruvian shelf between 12°S and 14°S , extreme N deficits (N^* down to $-60 \mu\text{mol l}^{-1}$, Supplementary Fig. S1) were detected along with the presence of hydrogen sulphide (H_2S). These stations are not further considered in the remaining discussions unless otherwise indicated, as the resident microbial communities and processes profoundly differ from typical OMZ scenarios (Schunck *et al.* submitted.).

Sources of nitrite

Nitrite in the OMZs can be generated by NH_3 oxidation, the first step of nitrification, or by the reduction of nitrate to nitrite^{6,21,22}. Ammonia oxidation has been identified as a NO_2^- source in the Peruvian OMZ that is active under near-anoxic conditions^{21,23,29}. Our measured rates of NH_3 oxidation generally peaked at the base of the oxycline ($\sim 90 \text{ nmol N l}^{-1} \text{ d}^{-1}$), decreased to the detection limit at the stations furthest offshore, and were not detectable in the core of the OMZ (Table 1 and Supplementary Table S2). The presence of both archaeal and bacterial ammonia oxidizers is verified by the detection of their functional genes encoding ammonia monooxygenase subunit A (Table 1 and Supplementary Table S3).

Integrated over the thickness of the OMZ, NO_2^- production through NH_3 oxidation increased from undetectable at the westernmost stations to $\leq 4.7 \text{ mmol NO}_2^- \text{ m}^{-2} \text{ d}^{-1}$ near the coast (Fig. 2a and Supplementary Table S1). For the entire OMZ volume examined ($\sim 5.5 \times 10^5 \text{ km}^3$), NH_3 oxidation is estimated to produce $\sim 3.8 \text{ Tg N yr}^{-1}$ of NO_2^- , with 24% attributed to coastal OMZ (≤ 600 m) and 76% offshore (>600 m; Fig. 3). Although significant rates have also been reported for the surface mixed layer in the ETSP (ref. 30), the mixed layer was not included in the present OMZ budget.

Overall, NH_3 oxidation accounted for only $\sim 7\%$ of the total NO_2^- production. Most came from NO_3^- reduction to NO_2^- , consistent with previous findings in the Peruvian, Namibian and Arabian Sea OMZs (refs 15,21,22). Apart from its association with anammox, NO_3^- reduction to NO_2^- is the first step in denitrification and DNRA, and NO_3^- is the next preferred terminal electron acceptor after O_2 for the oxidation of organic matter. NO_3^-

Table 1 | Abundance of selected N-functional genes and N-conversion rates in the ETSP during cruise M77-3.

	N-functional gene abundances (10^2 copies ml^{-1})							N-conversion rates ($\text{nmol N l}^{-1} \text{d}^{-1}$)					
	arch- <i>amoA</i>	β - <i>amoA</i>	γ - <i>amoA</i>	<i>hzo1</i>	<i>hzo2</i>	<i>den-nirS</i> *	<i>nrfA</i>	NH_3 ox.	Anammox	Denitrification	DNRA	NO_2^- ox.	NO_3^- red.
Coastal OMZ (≤ 600 m)													
N	63 (64)	8 (49)	0 (64)	8 (64)	42 (64)	0 (63)	0 (64)	27 (33)	33 (33)	3 (33)	7 (33)	27 (32)	27 (32)
Range	0.16–2773	0.05–1056	–	0.05–0.09	0.14–12.8	–	–	0.22–48.8	2.84–227	2.21–5.42	0.48–1.74	8.48–928	3.79–1010
Mean	676	135	–	0.07	4.45	–	–	8.24	43.4	4.19	1.14	172	203
Median	90	5.0	–	0.06	3.77	–	–	3.40	21.2	4.94	1.10	65.4	101
Offshore OMZ (>600 m)													
N	67 (71)	2 (33)	0 (72)	4 (71)	43 (72)	2 (72)	1 (72)	17 (40)	33 (40)	0 (40)	3 (40)	27 (40)	25 (34)
Range	0.04–2332	0.15–1.36	–	0.01–0.09	0.06–14.7	0.06–1.98	0.11	0.51–88.8	0.71–46.9	–	0.33–1.31	4.58–186	4.53–77.4
Mean	352	0.75	–	0.08	3.15	1.02	0.11	20.9	6.14	–	0.82	40.6	32.1
Median	89.5	0.75	–	0.08	1.51	1.02	0.11	5.79	3.01	–	0.83	30.2	22.3

Functional genes and N-conversion rates were not always determined at the same station and/or depths but with a comparable latitudinal and longitudinal as well as vertical resolution. N = number of samples in which N-functional genes or N processes were detected; in parentheses: number of samples analysed. *denitrifier-*nirS*.

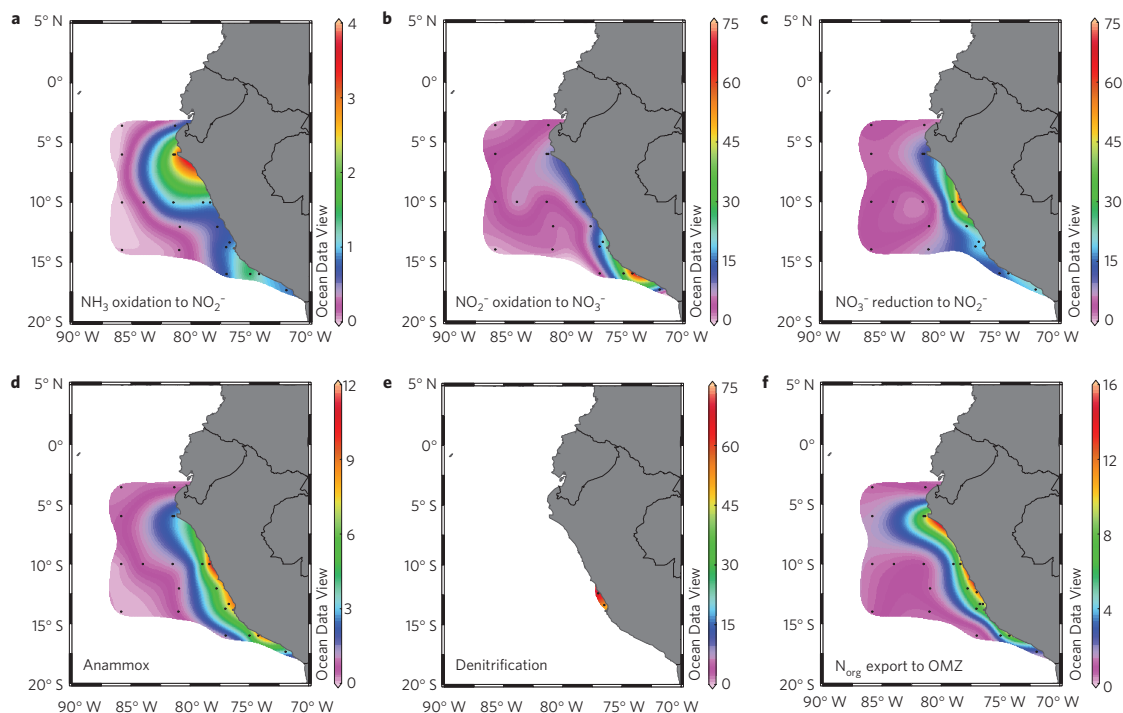


Figure 2 | Depth-integrated N-cycling rates in the ETSP OMZ. a,b, The two steps of the aerobic nitrification, NH_3 oxidation and NO_2^- oxidation. **c**, NO_3^- reduction to NO_2^- . **d,e**, N loss due to anammox as well as denitrification coupled to the oxidation of H_2S during a sulphidic event on the Peruvian shelf. **f**, Modelled export of organic N (N_{org}) from the euphotic zone to the OMZ. All rates are in $\text{mmol N m}^{-2} \text{d}^{-1}$. Black dots represent ^{15}N experimental stations.

reduction was detected throughout the OMZ at all investigated stations; it reached a maximum ($\sim 1 \mu\text{mol N l}^{-1} \text{d}^{-1}$) over the central shelf, but dropped to $\sim 5 \text{ nmol N l}^{-1} \text{d}^{-1}$ at the westernmost offshore stations (Table 1).

Depth-integrated rates showed a similarly declining trend offshore (Fig. 2c and Supplementary Table S1). Integration over the whole region yields an annual NO_3^- reduction of $\sim 49 \text{ Tg N}$, of which 29% occurs in the coastal OMZ and 71% offshore (Fig. 3).

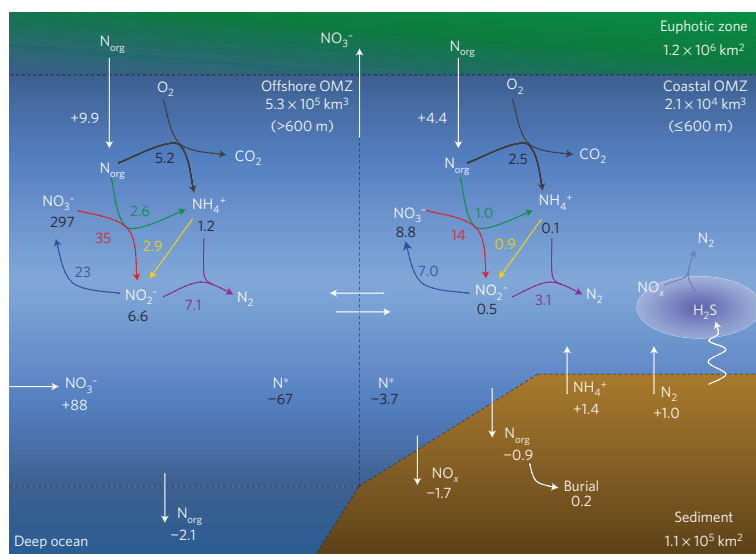


Figure 3 | N fluxes and nutrient inventory of the ETSP OMZ. Black numbers indicate inventories of dissolved inorganic nitrogen (in Tg N). They were derived from the depth-integrated values over the OMZ thickness shown in Figs 1 and 2, and then, on the basis of the 600 m seafloor depth cutoff for coastal versus offshore OMZs, the depth-integrated values were further integrated over the areal extents of the two types of OMZ. Fluxes (in Tg N y^{-1}) within the OMZ or across its boundaries are given in colour and white, respectively. A detailed description of the flux calculations is included in the Supplementary Information.

Table 2 | Spearman rank correlation of depth-integrated nutrients and N-cycling rates as well as modelled export production rates.

	NH ₃ oxidation	NO ₂ ⁻ oxidation	NO ₃ ⁻ reduction	Anammox	Export production
NH ₄ ⁺	0.51*	0.31	0.08	0.30	0.29
NO ₂ ⁻	0.46*	0.49*	0.71***	0.64**	0.10
N*	-0.08	-0.20	-0.05	-0.02	-0.02
Export production	0.56*	0.60**	0.75***	0.79***	
Anammox	0.75***	0.86***	0.88***		
NO ₃ ⁻ reduction	0.49*	0.75***			
NO ₂ ⁻ oxidation	0.73***				

Presented values are correlation coefficients with significant values denoted by * ($P \leq 0.05$), ** ($P \leq 0.01$) and *** ($P \leq 0.001$).

Consistent with previous observations from the Peruvian²³ and the Arabian Sea¹⁵ OMZs, NO₃⁻ reduction significantly correlated with depth-integrated NO₂⁻ concentrations (Spearman $R = 0.71$, $P \leq 0.001$; Table 2), which indicates that NO₃⁻ reduction is a major contributor to the secondary NO₂⁻ maxima.

Sinks of nitrite

Nitrite oxidation, the second step in nitrification, was most active in the upper OMZ throughout the ETSP. Its activity was detected deeper into the OMZ than NH₃ oxidation, consistent with earlier reports^{23,29}. Nitrite oxidation rates were highest (928 nmol N l⁻¹ d⁻¹) over the Peruvian shelf despite low O₂ levels (Table 1), and declined sharply to ≤ 20 nmol N l⁻¹ d⁻¹ along the furthest offshore transect. Although NO₂⁻ oxidation is believed to require O₂, this process has been detected at $< 1-2 \mu\text{mol O}_2 \text{ l}^{-1}$ in the Peruvian^{23,29} and Namibian OMZs (refs 22). O₂ sensitivity assays ($\sim 1-25 \mu\text{mol l}^{-1}$) at two stations further demonstrated only a moderate attenuation by low O₂ (at most $\sim 50\%$ activity reduction at $< 1 \mu\text{mol l}^{-1}$; Supplementary Fig. S3), which agrees well with observations in the Namibian OMZ (ref. 22). Apparently, NO₂⁻ oxidizers are well adapted to O₂-deficient environments.

NO₂⁻ supply from NH₃ oxidation, the first step of nitrification, is thought to constrain NO₂⁻ oxidation rates. Despite the significant correlation between NH₃ and NO₂⁻ oxidation rates (Spearman $R = 0.73$, $P \leq 0.001$; Table 2), NO₂⁻ oxidation rates in the ETSP OMZ exceeded those of NH₃ oxidation often by more than tenfold (Fig. 2a,b and Supplementary Tables S1 and S2). Similar observations in the OMZs off Namibia²² and Peru^{23,29} indicate a decoupling of the two steps of nitrification in O₂-deficient systems. A likely alternative NO₂⁻ source is NO₃⁻ reduction.

On the basis of modelled N fluxes, a NO₂⁻ shunt, in which 45–74% of the NO₃⁻ reduced to NO₂⁻ by denitrifying microorganisms is re-oxidized by aerobic NO₂⁻ oxidizers, has been proposed for the ETSP (ref. 31). In agreement, our annual rates of NO₂⁻ oxidation for the coastal (7 Tg N yr⁻¹) and offshore OMZ (23 Tg N yr⁻¹) are equivalent to 51% and 65%, respectively, of NO₃⁻ reduction (Fig. 3). The strong correlation between the two processes (Spearman $R = 0.75$, $P \leq 0.001$; Table 2) indicates a close coupling between NO₂⁻ oxidation and NO₃⁻ reduction in the ETSP OMZ.

Meanwhile, only sporadic and low rates of DNRA ($\leq 1.3 \text{ nmol l}^{-1} \text{ d}^{-1}$) were detected during our sampling period

(Table 1). A general lack of detectable *nrfA*, a key functional gene encoding for the cytochrome *c* nitrite reductase, corroborates these results (Table 1). DNRA seems to exhibit a high degree of spatio-temporal variability, with similarly low rates measured on the Namibian shelf²², but with tenfold greater rates and *nrfA* gene abundance than previously observed in the OMZs off Peru²¹ and Oman¹⁴. Hence, we cannot exclude DNRA as a significant NO_x^- sink for and NH_4^+ source in the ETSP at other times.

Nitrogen-loss activities

At the time of our sampling, denitrification, expressed as the production of $^{30}\text{N}_2$ from $^{15}\text{NO}_x$, was generally non-detectable. Low rates of denitrification ($2\text{--}5\text{ nmol l}^{-1}\text{ d}^{-1}$) were measured in three samples from the Peruvian shelf OMZ (Table 1 and Supplementary Table S2). Substantially higher rates were detected in a few samples containing measurable amounts of H_2S (Fig. 2e and Supplementary Tables S1 and S2), suggesting a coupling with H_2S oxidation (ref. 32; Schunck *et al.* submitted.). In contrast to the conclusion drawn by a recent study³³, water-column denitrification was only of minor importance ($\ll 1\%$ total N loss) for the overall N budget in the ETSP OMZ (Supplementary Information).

N_2 production attributed to anammox was detected at all stations except the two furthest offshore, consistent with previous studies in the ETSP (refs 13,20,34). Anammox activity was often enhanced in the upper OMZ and markedly elevated in the bottom waters over the shelf and upper continental slope. Rates were highest ($\leq 225\text{ nmol N l}^{-1}\text{ d}^{-1}$) over the central shelf ($10^\circ\text{S--}16^\circ\text{S}$) and declined by two orders of magnitude westward (Table 1). The presence of anammox bacteria was verified by the detection of their characteristic hydrazine (N_2H_4) oxidoreductase genes (*hzol* and 2) throughout the OMZ; whereas denitrifier-*nirS*, encoding for the cytochrome *cd*₁-containing nitrite reductase, was generally not detectable (Table 1 and Supplementary Table S3).

Depth-integrated anammox rates were $>10\text{ mmol N m}^{-2}\text{ d}^{-1}$ on the central shelf, similar to previous findings¹³, and $<1\text{ mmol N m}^{-2}\text{ d}^{-1}$ at the furthest offshore stations (Fig. 2d and Supplementary Table S1). Altogether, anammox accounts for an annual N loss of $\sim 10\text{ Tg}$ in an area of $1.2 \times 10^6\text{ km}^2$, which is at the lower end of earlier estimates for the ETSP ($9\text{--}26\text{ Tg N yr}^{-1}$; refs 13,18,23,35).

Flux measurements of dissolved inorganic nitrogen and N_2 made just before our sampling demonstrate that the sediments underlying the OMZ are further sites of N loss¹⁶. Combined with reaction-diffusion modelling, anammox and denitrification were shown to be active N sinks in the Peruvian coastal sediments. On the basis of the reported sedimentary NO_2^- fluxes and NO_x^- partitioning between anammox, denitrification and DNRA (ref. 16), we estimate a loss of 1 Tg N yr^{-1} from sediments in contact with the OMZ bottom waters (Fig. 3).

Conventionally, the accumulation of NO_2^- in OMZ waters has been interpreted as a sign of active N loss, and thus, is targeted by most field-sampling campaigns^{17–20,23,26,29}. Our data contradict this interpretation. Unlike NO_2^- , depth-integrated anammox rates did not reveal any meridional trends, but decreased from shelf to offshore. Whereas depth-integrated anammox rates and NO_2^- concentration were moderately correlated (Spearman $R = 0.64$; $P < 0.001$; Table 2) significant correlations between volumetric rates and NO_2^- concentrations were observed only for the shelf OMZ (Spearman $R = 0.72$, $P < 0.001$) and not offshore (Spearman, $P > 0.5$). NO_2^- accumulation offshore probably resulted from a greater persistence of NO_3^- reduction to NO_2^- compared with other NO_2^- -consuming processes in a poorly ventilated region, where the net NO_2^- gain was about five times higher compared with the coastal OMZ (11.4 and 2.2 Tg N yr^{-1} , respectively).

Ongoing water-column N loss cannot be deduced simply from the intensity of N^* minima, as shown by the lack of significant

correlation (Spearman $P > 0.05$) between anammox activity and N^* (Table 2). Whereas the depth-integrated N deficit is largest (most negative N^*) offshore, anammox activity is highest over the shelf and upper continental slope. Although comprising only 10% of the area covered and merely 4% of the sampled OMZ volume, coastal OMZ waters contribute as much as 30% of the total N loss (Fig. 3). Meanwhile, N deficits in coastal OMZ waters amount to only 5% (4 Tg N) of the total N deficit (71 Tg N). Hence, the large N deficit offshore most likely results from horizontal advection of N-deficient shelf waters²¹ that accumulate owing to a long residence time in the offshore OMZ (~ 10 years based on N^* and measured N loss). This is analogous to recent observations made in the Arabian Sea: substantial NO_2^- accumulation and low N-loss activity in the central basin, compared with the rapid N loss over the adjacent productive Omani shelf^{4,15}.

Sources of ammonium

N loss driven by anammox requires NH_4^+ , which usually does not accumulate in OMZs. Ammonium concentrations can be kept low by a tight coupling between NH_4^+ production and consumption processes, although the NH_4^+ released at the reported remineralization rates may already be sufficient to fuel anammox. Major sources of NH_4^+ are water-column organic matter remineralization and sedimentary NH_4^+ release.

DNRA and organic matter ammonification are active benthic NH_4^+ sources off the coast of Peru. During two preceding cruises (M77-1 and 2) to the ETSP (ref. 16), large NH_4^+ fluxes ($\sim 0.5\text{--}4\text{ mmol m}^{-2}\text{ d}^{-1}$) from sediments into the overlying OMZ waters were measured on a cross-shelf transect at 11°S . The often enhanced anammox activity in the coastal OMZ bottom waters suggests a strong influence from NH_4^+ diffusing out of the sediments^{13,36}. Assuming an average benthic NH_4^+ flux of $\sim 2\text{ mmol m}^{-2}\text{ d}^{-1}$ and a typical anammox rate of $\sim 4\text{ mmol NH}_4^+\text{ m}^{-2}\text{ d}^{-1}$ for the Peruvian coastal waters, the underlying sediments could supply $\sim 50\%$ of the NH_4^+ needed for the anammox rates observed. Clearly, further NH_4^+ sources are necessary to fulfil the remaining requirements for anammox, especially in offshore OMZ waters, which are spatially decoupled from the sediments.

On the basis of the measured NO_3^- reduction rates, subsequent ammonification of Redfieldian organic matter generates 65% and 73% of the NH_4^+ needed for anammox in the coastal and offshore OMZs, respectively (Fig. 3). These are probably underestimates, considering the observed preferential degradation of N-rich organic matter through NO_3^- respiration under suboxic conditions³⁷. Whether the reduction of NO_3^- is directly coupled to the oxidation of organic matter, or indirectly through a recently proposed cryptic sulphur cycle³⁸, could not be discerned at this point.

Remineralization of sinking organic matter and subsequent NH_4^+ release is usually enhanced near the upper OMZ boundary, and would support the high anammox and NH_3 oxidation activity observed^{13–15,20,21,23}. On average, $\sim 40\%$ of their combined NH_4^+ demands are supplied by NO_3^- reduction, with the remainder possibly coming from microaerobic organic matter remineralization²⁰. The activity of O_2 -dependent nitrification at non-detectable O_2 concentrations in OMZs indicates that microaerobic respiration proceeds even at nanomolar O_2 levels, in accordance with an apparent half-saturation coefficient of $<20\text{ nmol l}^{-1}$ previously reported for microaerobic respiration in these waters³⁹. High O_2 consumption rates, mainly attributable to heterotrophic respiration, and genes encoding for terminal respiratory oxidases with high O_2 affinities were detected in the ETSP on the same expedition (Kalvelage *et al.* unpublished). Although there are suggestions that O_2 is efficiently depleted down to the limits of microaerobic respiration in the OMZ core⁴⁰, regular intrusions of more oxygenated surface waters or mixing events,

ARTICLES

NATURE GEOSCIENCE DOI: 10.1038/NNGE01739

such as those related to eddies⁴¹, may sustain aerobic microbial activity in the upper OMZ.

Surface productivity drives sub-surface nitrogen cycling

Depth-integrated anammox rates correlated strikingly well with NO_3^- reduction, NO_2^- oxidation and NH_3 oxidation (Spearman $R = 0.88$, 0.86 and 0.75 , respectively; $P \leq 0.001$), indicating a common controlling factor for their concerted activity. Our data suggest that N cycling processes in the OMZ are tightly coupled to the export of organic matter.

Export of organic matter at the base of the euphotic zone was estimated from net primary production⁴² (NPP) and the ratio of export-to-total primary production (*ef* ratio)⁴³. At the time of sampling, NPP was up to $\sim 3 \text{ g organic C (C}_{\text{org}}) \text{ m}^{-2} \text{ d}^{-1}$ near the coast and decreased to $< 0.5 \text{ g C}_{\text{org}} \text{ m}^{-2} \text{ d}^{-1}$ further offshore, values typical for the Peruvian upwelling system⁴⁴. Computed *ef* ratios ranged from 0.16 (low-NPP sites) to 0.42 (high-NPP sites). The resulting N-export production rates (converted from measured C: $N = 7.2$ of surface particulate organic matter) were $> 10 \text{ mmol organic N (N}_{\text{org}}) \text{ m}^{-2} \text{ d}^{-1}$ over the shelf and of the order of $\sim 1 \text{ mmol N}_{\text{org}} \text{ m}^{-2} \text{ d}^{-1}$ at the stations furthest offshore (Fig. 2f and Supplementary Table S1). Export production was highly correlated to depth-integrated rates of anammox, NO_3^- reduction and NO_2^- oxidation (Spearman $R = 0.79$, 0.75 and 0.60 , respectively, $P \leq 0.001$) as well as NH_3 oxidation (Spearman $R = 0.56$, $P \leq 0.01$; Table 2). This suggests that the lateral distribution of N-cycling activity, including anammox, is mainly determined by the export of organic matter, which is the ultimate source of the required reactive substrates NH_4^+ and NO_2^- in the OMZ.

Overall, we estimate NPP of 12 and 47 Tg N yr⁻¹ in the coastal and offshore surface waters, respectively, which seem reasonable at a net lateral supply of 88 Tg $\text{NO}_3^- \text{ yr}^{-1}$ to the upwelling region (Fig. 3). The corresponding export fluxes are 4.4 and 9.9 Tg $\text{N}_{\text{org}} \text{ yr}^{-1}$. Taking organic matter sedimentation and export to the deep ocean into account, our results show that the export production to the OMZ is sufficient as an N source to support the measured N fluxes.

In summary, extensive sampling and experimentation throughout the ETSP OMZ shows that the activity of anammox and N-linked processes is highly correlated with export production. High productivity over the shelf and upper slope, as well as sedimentary NH_4^+ release, drive high rates of tightly coupled N cycling processes and thus N loss through anammox in the shallow coastal OMZ compared with the offshore OMZ.

Although the globally expanding OMZs might increase the oceanic volume conducive to N loss, N loss would continue to rise only as long as there is sufficient nutrient supply for primary production in the euphotic zone, and nutrient supply is not hampered by intensified stratification (that is, reduced upwelling) due to ocean warming. These positive and negative feedbacks are important considerations for biogeochemical models, which at present do not adequately reproduce the observed spatial patterns of N loss in OMZs. In light of our results, the activities of N loss through anammox seem to be directly linked to export production rates in biogeochemical models using the following empirical relationship: $\text{anammox} = 0.7 \times \text{N}_{\text{org}} \text{ export}$ (Supplementary Fig. S4). This may facilitate a realistic assessment of the short- and long-term impacts of ocean de-oxygenation and changing productivity on N cycling in OMZs, as well as their effects on neighbouring water masses.

Methods

Physico-chemical and N cycling rate measurements. Large-scale distributions of chemical and biological variables were determined during the cruises M77-3 and 4 from December 2008 to February 2009 onboard R/V *Meteor*. Sea water was collected with either a conductivity–temperature–depth (CTD) rosette system

fitted with 101 Niskin bottles or a pump–CTD system (depth range: $\sim 375 \text{ m}$). Continuous vertical profiles of chlorophyll *a* were obtained fluorometrically and calibrated against discrete values derived from acetone extraction. Oxygen was measured with a Seabird sensor, a conventional amperometric microsensor and a highly sensitive STOX (switchable trace amount oxygen) sensor³⁹ (detection limit: 50 nmol l^{-1}). Dissolved inorganic N and PO_4^{3-} concentrations were analysed using standard protocols^{45,46}. Nitrogen deficits were calculated as N^* following ref. 47. Rates of microbial N cycling (NH_3 and NO_2^- oxidation, NO_3^- reduction, anammox, denitrification and DNRA) were determined in short-term, time-series incubation experiments with various combinations of ^{15}N -labelled and unlabelled compounds as described in refs. 22,48. Oxygen sensitivity assays for NO_2^- oxidation were conducted as previously described²². Consistent rates for anammox were calculated from the various ^{15}N incubation experiments ($^{15}\text{NH}_4^+ \pm ^{14}\text{NO}_2^-$, $^{15}\text{NO}_2^- \pm ^{14}\text{NH}_4^+$, $^{15}\text{NO}_2^- \pm ^{14}\text{NH}_4^+$) for coastal OMZ stations, whereas more variability was associated with offshore OMZ stations. Although the possibility of substrate stimulation due to $^{15}\text{N}/^{14}\text{N}$ amendments cannot be fully eliminated, marine microbes including anammox and nitrifying bacteria^{3,22} are often associated with particles, and thus can experience substrate concentrations several orders of magnitude greater than the ambient water⁴⁹ such that our measured rates could also be substantially underestimated. To examine whether the export production is sufficient to support these measured rates of various subsurface N-cycling processes and ultimately N loss, the maximum potential rates for anammox from the various isotope amendments (Supplementary Table S2) were used in budget calculations. On the basis of our combined rate measurements, nutrient inventories and subsequent modelling, the N fluxes are sufficient to support all measured rates of N transformation. Hence, the here-presented measured rates may not be too far from reality.

Molecular ecological analyses. Water samples for nucleic-acid-based analyses were collected onto polyethersulphone membrane filters ($0.2 \mu\text{m}$; Millipore) and immediately frozen at -80°C until further analysis. Nucleic acids were extracted using a Qiagen DNA/RNA All prep Kit following the manufacturer's protocol with minor modifications⁵⁰. Functional genes for archaeal and bacterial (β/γ -proteobacterial) NH_3 oxidation (arch-*amoA* and β/γ -*amoA*, respectively), anammox (*hzol* 1 and 2), denitrification (denitrifier-*nirS*) and DNRA (*nrfA*) were PCR-amplified as described previously⁵⁰. Standards for quantitative PCRs were obtained from: *Nitrosococcus oceanii* NC10 and *Nitrosomonas marina* NM22 and NM51 (γ - and β -*amoA*, respectively), an environmental clone (GenBank accession number JF796147; arch-*amoA*), *Candidatus 'Scalindua profunda'* (*hzol* 1 and 2), *Pseudomonas aeruginosa* PAO1 (denitrifier-*nirS*) and *Escherichia coli* K12 (*nrfA*).

Modelling of export production. Export production was calculated from estimates of NPP and the ratio of export production to total primary production (*ef* ratio). NPP at the time and location of our experimental stations was computed from measured chlorophyll *a* concentrations and satellite-based (MODIS (Moderate Resolution Imaging Spectroradiometer) ocean colour data) estimates of photosynthetic available radiation using the vertically generalized production model⁵¹. *ef* ratios were calculated from NPP and measured surface temperatures according to ref. 43.

Received 12 July 2012; accepted 21 January 2013; published online 24 February 2013

References

- Kamykowski, D. & Zentara, S. Hypoxia in the world ocean as recorded in the historical data set. *Deep-Sea Res.* **37**, 1861–1874 (1990).
- Karstensen, J., Stramma, L. & Visbeck, M. Oxygen minimum zones in the eastern tropical Atlantic and Pacific oceans. *Progr. Oceanogr.* **77**, 331–350 (2008).
- Diaz, R. J. & Rosenberg, R. Spreading dead zones and consequences for marine ecosystems. *Science* **321**, 926–929 (2008).
- Stramma, L. *et al.* Expanding oxygen-minimum zones in the tropical oceans. *Science* **320**, 655–658 (2008).
- Keeling, R. F., Körtzinger, A. & Gruber, N. Ocean deoxygenation in a warming world. *Annu. Rev. Mar. Sci.* **463–493** (2009).
- Lam, P. & Kuypers, M. M. Microbial nitrogen cycling processes in oxygen minimum zones. *Annu. Rev. Mar. Sci.* **3**, 317–347 (2011).
- Gruber, N. The dynamics of the marine nitrogen cycle and its influence on atmospheric CO_2 . *NATO ASI Ser.* **97–148** (2004).
- Deutsch, C. *et al.* Climate-forced variability of ocean hypoxia. *Science* **333**, 336–339 (2011).
- Moore, J.K. & Doney, S.C. Iron availability limits the ocean nitrogen inventory stabilizing feedbacks between marine denitrification and nitrogen fixation. *Glob. Biogeochem. Cycles* **21**, GB2001 (2007).
- Schmittner, A. *et al.* Future changes in climate, ocean circulation, ecosystems, and biogeochemical cycling simulated for a business-as-usual CO_2 emission scenario until year 4000 AD. *Glob. Biogeochem. Cycles* **22**, GB1013 (2008).

11. Somes, C. J. *et al.* Simulating the global distribution of nitrogen isotopes in the ocean. *Glob. Biogeochem. Cycles* **24**, GB4019 (2010).
12. Kuypers, M. M. *et al.* Massive nitrogen loss from the Benguela upwelling system through anaerobic ammonium oxidation. *Proc. Natl Acad. Sci. USA* **102**, 6478–6483 (2005).
13. Hamersley, M. R. *et al.* Anaerobic ammonium oxidation in the Peruvian oxygen minimum zone. *Limnol. Oceanogr.* **52**, 923–933 (2007).
14. Jensen, M. M. *et al.* Intensive nitrogen loss over the Omani Shelf due to anammox coupled with dissimilatory nitrite reduction to ammonium. *ISME J.* **5**, 1660–1670 (2011).
15. Lam, P. *et al.* Origin and fate of the secondary nitrite maximum in the Arabian Sea. *Biogeosciences* **8**, 1565–1577 (2011).
16. Bohlen, L. *et al.* Benthic nitrogen cycling traversing the Peruvian oxygen minimum zone. *Geoch. Cosmochim. Acta* **75**, 6094–6111 (2011).
17. Cline, J. D. & Richards, F. A. Oxygen deficient conditions and nitrate reduction in the eastern tropical North Pacific Ocean. *Limnol. Oceanogr.* **17**, 885–900 (1972).
18. Codispoti, L. A. & Packard, T. T. Denitrification rates in the eastern tropical south-pacific. *J. Mar. Res.* **38**, 453–477 (1980).
19. Nagvi, S. W. Some aspects of the oxygen-deficient conditions and denitrification in the Arabian Sea. *J. Mar. Res.* **45**, 1049–1072 (1987).
20. Thamdrup, B. *et al.* Anaerobic ammonium oxidation in the oxygen-deficient waters off northern Chile. *Limnol. Oceanogr.* **51**, 2145–2156 (2006).
21. Lam, P. *et al.* Revisiting the nitrogen cycle in the Peruvian oxygen minimum zone. *Proc. Natl Acad. Sci. USA* **106**, 4752–4757 (2009).
22. Füssel, J. *et al.* Nitrite oxidation in the Namibian oxygen minimum zone. *ISME J.* **6**, 1200–1209 (2012).
23. Lipschultz, F. *et al.* Bacterial transformations of inorganic nitrogen in the oxygen-deficient waters of the Eastern Tropical South Pacific Ocean. *Deep-Sea Res.* **37**, 1513–1541 (1990).
24. Kavelage, T. *et al.* Oxygen sensitivity of anammox and coupled N-cycle processes in oxygen minimum zones. *PLoS ONE* **6**, e29299 (2011).
25. Fuenzalida, R. *et al.* Vertical and horizontal extension of the oxygen minimum zone in the eastern South Pacific Ocean. *Deep-Sea Res. II* **56**, 992–1003 (2009).
26. Codispoti, L. A. & Christensen, J. P. Nitrification, denitrification and nitrous oxide cycling in the eastern tropical South Pacific ocean. *Mar. Chem.* **16**, 277–300 (1985).
27. Wooster, W. S., Chow, T. J. & Barrett, I. Nitrite distribution in Peru current waters. *J. Mar. Res.* **23**, 210–221 (1965).
28. Nelson, S. S. & Neshyba, S. On the southernmost extension of the Peru–Chile Undercurrent. *Deep-Sea Res.* **26A**, 1387–1393 (1979).
29. Ward, B. B., Glover, H. E. & Lipschultz, F. Chemoautotrophic activity and nitrification in the oxygen minimum zone off Peru. *Deep-Sea Res.* **36**, 1031–1051 (1989).
30. Fernández, C., Fariás, L. & Alcaman, M. E. Primary production and nitrogen regeneration processes in surface waters of the Peruvian upwelling system. *Progr. Oceanogr.* **83**, 159–168 (2009).
31. Anderson, J. J. *et al.* A model for nitrite and nitrate distributions in oceanic oxygen minimum zones. *Deep-Sea Res.* **29**, 1113–1140 (1982).
32. Lavik, G. *et al.* Detoxification of sulphidic African shelf waters by blooming chemolithotrophs. *Nature* **457**, 581–584 (2008).
33. Dalsgaard, T. *et al.* Anammox and denitrification in the oxygen minimum zone of the eastern South Pacific. *Limnol. Oceanogr.* **57**, 1331–1346 (2012).
34. Ward, B. B. *et al.* Denitrification as the dominant nitrogen loss process in the Arabian Sea. *Nature* **461**, 78–81 (2009).
35. Deutsch, C. *et al.* Denitrification and N₂ fixation in the Pacific Ocean. *Glob. Biogeochem. Cycles* **15**, 483–506 (2001).
36. Dalsgaard, T. *et al.* N₂ production by the anammox reaction in the anoxic water column of Golfo Dulce, Costa Rica. *Nature* **422**, 606–608 (2003).
37. Van Mooy, B. A., Keil, R. G. & Devol, A. H. Impact of suboxia on sinking particulate organic carbon: Enhanced carbon flux and preferential degradation of amino acids via denitrification. *Geochem. Cosmochim. Acta* **66**, 457–465 (2002).
38. Canfield, D. E. *et al.* A cryptic sulphur cycle in oxygen-minimum zone waters off the Chilean coast. *Science* **330**, 1375–1378 (2010).
39. Revsbech, N. P. *et al.* Determination of ultra-low oxygen concentrations in oxygen minimum zones by the STOX sensor. *Limnol. Oceanogr.* **7**, 371–381 (2009).
40. Thamdrup, B., Dalsgaard, T. & Revsbech, N. P. Widespread functional anoxia in the oxygen minimum zone of the eastern South Pacific. *Deep-Sea Res.* **1** **65**, 36–45 (2012).
41. Bertrand, A., Ballón, M. & Chaigneau, A. Acoustic observation of living organisms reveals the upper limit of the oxygen minimum zone. *PLoS ONE* **5**, e10330 (2010).
42. Behrenfeld, M. J. & Falkowski, P. G. Photosynthetic rates derived from satellite-based chlorophyll concentration. *Limnol. Oceanogr.* **42**, 1–20 (1997).
43. Laws, E. A. *et al.* Temperature effects on export production in the open ocean. *Glob. Biogeochem. Cycles* **14**, 1231–1246 (2000).
44. Pennington, J. T. *et al.* Primary production in the eastern tropical Pacific: A review. *Progr. Oceanogr.* **69**, 285–317 (2006).
45. Grasshoff, K. *et al.* *Methods of Seawater Analysis* (Wiley, 1999).
46. Holmes, R. M. *et al.* A simple and precise method for measuring ammonium in marine and freshwater ecosystems. *Can. J. Fish. Aquat. Sci.* **56**, 1801–1808 (1999).
47. Gruber, N. & Sarmiento, J. L. Global Patterns of Marine Nitrogen Fixation and Denitrification. *Glob. Biogeochem. Cycles* **11**, 235–266 (1997).
48. Holtappels, M. *et al.* 15N-labelling experiments to dissect the contributions of heterotrophic denitrification and anammox to nitrogen removal in the OMZ waters of the ocean. *Methods Enzymol.* **486**, 223–251 (2011).
49. Stocker, R. Marine microbes see a sea of gradients. *Science* **338**, 628–633 (2012).
50. Loescher, C. R. *et al.* Production of oceanic nitrous oxide by ammonia-oxidizing archaea. *Biogeochem. Disc.* **9**, 2095–2122 (2012).

Acknowledgements

We wish to thank the Peruvian government for access to their territorial waters. We sincerely thank the cruise leader M. Frank as well as the crews of the cruises M77-3 and 4 onboard R/V *Meteor* for their support at sea. We are grateful for the technical and analytical assistance of G. Klockgether, I. Boosmann, V. Leon, I. Grefe and A. Ellrott. We thank N. P. Revsbech, who generously provided the STOX sensors, and T. Ferdelmann for offering valuable comments to improve the article. This study was supported by the Deutsche Forschungsgemeinschaft through the Sonderforschungsbereich 754 'Climate-Biogeochemistry Interactions in the Tropical Ocean' and the Max Planck Society.

Author contributions

T.K., G.L. and M.M.M.K. designed the study. T.K., G.L., S.C. and A.P. performed ¹⁵N-labelling experiments. T.K., G.L. and P.L. analysed the data. C.R.L. carried out functional gene analyses. L.A. and A.O. modelled export production rates. L.S. provided CTD and ADCP data. T.K., G.L., P.L. and M.M.M.K. wrote the manuscript with input from all co-authors.

Additional information

Supplementary information is available in the online version of the paper. Reprints and permissions information is available online at www.nature.com/reprints. Correspondence and requests for materials should be addressed to M.M.M.K.

Competing financial interests

The authors declare no competing financial interests.

3 Synthesis

3.1 Phytoplankton C:N:P: acclimation vs. adaptation

The results presented in this thesis rely largely on the accurate determination of phytoplankton cell-quotas. The ratio of subsistence and actual cell-quotas ($Q_0^{\text{nutrient}} : Q^{\text{nutrient}}$) is the basis for the determination of nutrient and light colimitation areas (Chapter 1), as well as the distribution of species adapted to different light and nutrient conditions (Chapter 3). The phytoplankton N:P global pattern obtained with the optimality-based model (Fig. 2-Chapter 1), shows in general a high N:P ratio in high latitudes and the Equatorial Pacific, and low N:P in subtropical regions. This pattern is mainly constrained by the distribution of areas of N limitation in the global ocean. N is identified as the main limiting nutrient in the tropical and subtropical ocean (Fig. 4-Chapter 1), hence low phytoplankton N:P ratios are estimated for these regions. This pattern does not entirely adhere to what is observed in samples of particulate organic matter associated with autotrophic organisms, which overall suggests high N:P ratios in low latitudes and viceversa (*Martiny et al., 2013a*). The difference between the model-based N:P and the N:P ratio inferred from POM observations is reduced when the longitudinal mean is calculated across different latitudes (Fig. 3-Chapter 1).

The global phytoplankton N:P pattern predicted by the optimality-based model is a result of phytoplankton acclimation to N and P availability and limitation. This behaviour has been observed in laboratory cultures, where phytoplankton N:P follows the dissolved inorganic N:P ratio (*Rhee, 1974, 1978*). Nevertheless, in the global ocean areas of low dissolved N:P are often believed to be associated with high phytoplankton N:P ratios (*Martiny et al., 2013a*). These areas tend to be zones of intense nutrient limitation, such as the oligotrophic gyres. Different cellular components have their own stoichiometric properties (*Falkowski, 2000*). Phytoplankton is expected to have high N:P ratios in nutrient limited zones as a result of a physiological adaptation to low nutrient conditions. The cellular nutrient-acquisition machinery, greatly conformed by proteins, is high in N but low in P, whereas the growth machinery, composed by molecules such as ribosomal RNA, has a lower N:P ratio (*Geider and La Roche, 2002*). Species adapted to low nutrient and slow growth conditions are expected to have an inherent high N:P elemental composition, while fast growing species are thought to have a lower N:P ratio (*Arrigo, 2005*). As a consequence, phytoplankton species in low latitudes (nutrient-limited areas) are assumed to be associated with high N:P ratios, while species in high latitudes (nutrient-rich areas) are assumed to be associated with low N:P ratios.

The hypothesis that phytoplankton stoichiometry is determined by adaptation anticipates high phytoplank-

ton N:P in low latitudes and low N:P in high latitudes. On the contrary, the acclimation hypothesis predicts low N:P in low latitudes and viceversa. The idea of a genetically determined cellular composition adapted to certain environmental conditions is to some extent supported by global observations of phytoplankton N:P (*Martiny et al., 2013a*). At the same time, the hypothesis of a dynamic optimal phytoplankton acclimation to diverse nutrient and light regimes appears also valid, and is supported by laboratory studies as well as global observations in phytoplankton C:P and C:N ratios (see Chapter 1 and *Martiny et al., 2013b*). Two major question thus arise: What determines phytoplankton stoichiometry in the global ocean? Are changes in stoichiometric ratios mainly driven by a pre-established adaptation or by dynamic continuous acclimation of phytoplankton to its physicochemical environment?

The optimality-based model predicts not only observed patterns of C:P and C:N, but also the expected distribution of the global Chl:C ratio. High Chl:C is expected in high latitudes where light limitation is important, while a low Chl:C ratio is predicted in low latitudes where light levels are constantly high (see Chapter 1 and 3). Chl synthesis is expected to depend on photosynthetic rates, which at the same time rely on enzyme activity and hence N availability. If the adaptation hypothesis dominates the regulation of phytoplankton elemental composition, how can the idea of a low N:P in light-limited high latitudes be reconciled with a high Chl:C ratio in these regions? A possible explanation is that Chl:C is not directly related to N:P, but to the C:N ratio. The adaptation hypothesis initially predicts a low phytoplankton N-content in high latitude fast-growth regions, and a high N-content in low latitude slow-growth regions. This would thus imply high C:N in high latitudes and viceversa, which is against observed patterns of C:N obtained from POM samples (*Martiny et al., 2013b*), and global C:N patterns predicted by the acclimation hypothesis (Chapter 1). Hence, while the acclimation hypothesis provides a clear link between phytoplankton elemental stoichiometry and Chl cell-quota, the relation between expected patterns of Chl:C and assumed C:N:P ratios according to the adaptation hypothesis is not entirely clear.

A likely realistic scenario is that both hypotheses (acclimation and adaptation) complement each other to explain the variability in phytoplankton cellular composition. Different phytoplankton species might have a predetermined range of cellular compositions resulting from adaptation to ambient conditions. At the same time, the internal regulation of phytoplankton composition is a dynamic process observed in culture experiments (*Pahlow and Oschlies, 2009; Pahlow et al., 2013*), that likely also takes place in the ocean. This optimal regulation probably acts on top of any preset constraints to cellular stoichiometry, altering the cells elemental composition. A possible approach to account for both processes consists in employing a species allocation scheme as described in Chapter 3. This approach would result in phytoplankton adapted

to nutrient-limiting conditions in low latitudes to have a higher nutrient affinity with respect to high latitude species. Phytoplankton in low latitudes would have higher N uptake rates, increased N cell-quota, and greater N:P ratios, as expected from POM observations (*Martiny et al., 2013a*). On the other hand, phytoplankton in high latitudes would show a lesser increase in N cell-quota, and hence lower N:P ratio with respect to phytoplankton in lower latitudes.

3.2 Phytoplankton physiology and oceanic productivity

Bio-optical satellite models of primary productivity do not explicitly account for the effects of nutrient limitation on phytoplankton growth. In order to assess both nutrient- and light-dependent physiological constraints on growth and PP, a method to infer monthly nitrate concentrations in the global surface ocean was developed in Chapter 2. One of the main conclusions of the colimitation analysis presented in Chapter 1 is that N is the main limiting nutrient in the global ocean. P seems to have only a colimiting effect. This conclusion is derived from physiological changes in N and P cell-quotas of phytoplankton (instead of regional patterns of dissolved inorganic N:P).

The estimation of PP described in Chapter 3 employs a physiological model to describe changes in the relative composition of phytoplankton with respect to carbon. While the relative patterns of biomass are inferred from satellite-Chl observations, the model predicts the Chl:C ratio resulting from photoacclimation at each 1° by 1° grid-box. Thus, this method is in essence a C-based method, as phytoplankton C-biomass is inferred prior to the estimation of the global production rates.

As shown in Chapter 3, C-based models of PP have also been developed from bio-optical algorithms (*Behrenfeld et al., 2005; Westberry et al., 2008*). These models show a distinct global latitudinal trend in oceanic primary productivity from Chl-based models. It is remarkable that the results obtained from a mechanistic-model able to describe phytoplankton physiological changes in Chl:C, yield global patterns and annual PP rates very similar to an independent C-based satellite model (Chapter 3). Satellite Chl-based models presently constitute the main reference of global PP patterns in the ocean. They are frequently used to evaluate the performance of global circulation models (GCMs) in simulating marine primary productivity. Most of these GCMs are calibrated in order to replicate and project the future carbon cycle. Given the observed differences between C and Chl-based models, important questions emerge over what each PP pattern represents, and which one describes more accurately the global carbon cycle.

Both bio-optical algorithms (C- and Chl-based), as well as the optimality-based model have been evaluated against independent in situ observation of C-fixation based on ^{14}C (see Chapter 3 and *Friedrichs et al.,*

2009). Nonetheless, no substantial differences were found among the predictive skills of these models. Part of the reason for this lack of differences between models is that all in situ observations correspond to the same oceanographic region in the Equatorial Pacific. The most striking contrast between C- and Chl-based models is observed when comparing global latitudinal trends in PP. Chl-based models assume that high Chl concentrations in high latitudes represent high PP rates, whereas C-based models attribute this pattern to high Chl:C ratios. Hence, to accurately describe differences between both types of models, a globally distributed data set of PP observations spread across several latitudinal degrees is necessary.

An alternative approach to assess the effects of phytoplankton flexible stoichiometry on predicted PP patterns by GCMs, is the incorporation of optimality-based dynamics in the biogeochemical compartment of such models. At the moment, alterations derived from climate change under intensive greenhouse gas emissions scenarios (RCP8.5, *Riahi et al., 2011*) are projected to decrease global net PP (NPP) rates by $\approx -8.6\%$ (*Bopp et al., 2013*). Total predicted changes in global NPP range from 0 to -16% (*Bopp et al., 2013*). Regional changes in NPP can have opposite sign and be substantially larger than global trends (*Steinacher et al., 2010*). Furthermore, alterations in the production of higher trophic levels (e.g., mesozooplankton) can be twice as large as projected changes in NPP (*Stock et al., 2014*). The main environmental drivers of these projected changes in NPP is a redistribution of nutrient and light availability as a result of strengthening surface ocean stratification (*Sarmiento et al., 2004; Schneider et al., 2008; Riebesell et al., 2009*). However, all these variations are inherently tied to the premise of phytoplankton fixed stoichiometry and lack of physiological acclimation (i.e. fixed Chl:C ratio). The results presented in this thesis show that phytoplankton growth, and hence PP, adjust via physiological acclimation to different nutrient and light limitation regimes. Hence, the assessment of repercussions of climate change for marine biogeochemical cycles, and primary productivity in particular, can yield different conclusions if physiological optimality-based formulations are employed.

Aiming to initiate the inclusion of physiological formulations of phytoplankton growth in global Earth system models, the optimality-based model of *Pahlow et al. (2013)* was coupled to the University of Victoria Earth System Climate Model (UVic_ESCM) (*Weaver et al., 2001*). The results derived from this modelling study are still under analysis. In the next section, the overall structure and changes made in the biogeochemical compartment of the UVic_ESCM are described, and an initial analysis of global biogeochemically relevant results is presented.

3.3 Coupling an optimality-based phytoplankton formulation into an Earth system climate model

3.3.1 Model implementation

A set of formulations describing optimality-based growth of phytoplankton (*Pahlow et al., 2013*) were included in the biogeochemical component of the UVic.ESCM (version 2.9) (*Weaver et al., 2001*). This biogeochemical component was recently improved by *Keller et al. (2012)* in order to better reproduce seasonal changes in marine ecosystems and the effect this has on ocean biogeochemistry.

The current version of the UVic.ESCM at the time of writing, includes NO_3 and PO_4 as nutrients. The change in time of each variable concentration (X) in the model is described by,

$$\frac{\partial X}{\partial t} = Tr + S \quad (1)$$

where Tr represents all transport terms including advection, isopycnal and diapycnal diffusion, and convection, and S denotes the source minus sink terms. In the UVic.ESCM, $S(\text{NO}_3)$ and $S(\text{PO}_4)$ are usually related via a fixed stoichiometric relationship (N:P=16, *Redfield, 1934*). The newly included phytoplankton model accounts for simultaneous colimitation by N and P in the cells. This translates in varying uptake rates of NO_3 and PO_4 not connected by any particular stoichiometric ratio. As a result, both sources, $S(\text{NO}_3)$ and $S(\text{PO}_4)$, are now described separately,

$$S(\text{NO}_3) = N_{remi} + N_{exc} + PhytN_{morpt} - PhytN\mu - DiazN\mu \quad (2)$$

$$S(\text{PO}_4) = P_{remi} + P_{exc} + PhytP_{morpt} - PhytP\mu - DiazP\mu \quad (3)$$

where N_{remi} and P_{remi} are N and P remineralization terms, N_{exc} and P_{exc} are N and P excretion terms, $PhytN_{morpt}$ and $PhytP_{morpt}$ are phytoplankton mortality terms defined for N and P that contribute directly to the pools of dissolved inorganic nutrients, $PhytN\mu$ and $PhytP\mu$ are the N and P uptake rates of non-diazotrophic (regular) phytoplankton, while $DiazN\mu$ and $DiazP\mu$ are the N and P uptake rates of diazotrophs. The remineralization rates are temperature (T) dependent and remain as in *Keller et al. (2012)*:

$$N_{remi} = remi_0 \cdot b^{cT} \cdot DetN \quad (4)$$

$$P_{remi} = remi_0 \cdot b^{cT} \cdot DetP \quad (5)$$

where $remi_0$ is an initial remineralization rate, $DetN$ and $DetP$ are the detritus components of N and P respectively, and b and c are temperature sensitivity parameters. Excretion is defined as the difference between zooplankton assimilation and growth efficiencies (γ and ϖ respectively). Excretion terms for C (C_{exc}), N, and P are defined as,

$$C_{exc} = C_{graz} \cdot (\gamma - \varpi) \quad (6)$$

$$N_{exc} = \gamma \cdot N_{graz} - (\gamma \cdot C_{graz} - C_{exc}) \cdot Q_{zoo}^N \quad (7)$$

$$P_{exc} = \gamma \cdot P_{graz} - (\gamma \cdot C_{graz} - C_{exc}) \cdot Q_{zoo}^P \quad (8)$$

where Q_{zoo}^N and Q_{zoo}^P are the N and P cell-quotas of zooplankton. C_{graz} , N_{graz} , and P_{graz} are the grazing terms for C, N, and P respectively. Each grazing term represents the sum of all grazing components: regular and diazotrophic phytoplankton ($Phyt(C, N, P)_{graz}$, $Diaz(C, N, P)_{graz}$), detritus ($Det(C, N, P)_{graz}$), and zooplankton ($Zoop(C, N, P)_{graz}$).

$$C_{graz} = PhytC_{graz} + DiazC_{graz} + DetC_{graz} + ZoopC_{graz} \quad (9)$$

$$N_{graz} = PhytN_{graz} + DiazN_{graz} + DetN_{graz} + ZoopN_{graz} \quad (10)$$

$$P_{graz} = PhytP_{graz} + DiazP_{graz} + DetP_{graz} + ZoopP_{graz} \quad (11)$$

Phytoplankton growth is described as the difference between carbon fixation (V^C) and respiration (R), for regular ($PhytC\mu$) and diazotrophic phytoplankton ($DiazC\mu$),

$$PhytC\mu = V_{phyt}^C - R \quad (12)$$

$$DiazC\mu = V_{diaz}^C - R \quad (13)$$

For a thorough description of the determination of phytoplankton growth rate see Chapter 3, Supplementary information, Eq. S.1–S.5.

Sources and sinks for regular and diazotrophic phytoplankton are determined separately for C, N, and P,

$$S(\text{PhyC}) = \text{PhytC}\mu - \text{PhytC}_{\text{graz}} - \text{PhytC}_{\text{morpt}} - \text{PhytC}_{\text{morp}} \quad (14)$$

$$S(\text{PhyN}) = \text{PhytN}\mu - \text{PhytN}_{\text{graz}} - \text{PhytN}_{\text{morpt}} - \text{PhytN}_{\text{morp}} \quad (15)$$

$$S(\text{PhyP}) = \text{PhytP}\mu - \text{PhytP}_{\text{graz}} - \text{PhytP}_{\text{morpt}} - \text{PhytP}_{\text{morp}} \quad (16)$$

$$S(\text{DiazC}) = \text{DiazC}\mu - \text{DiazC}_{\text{graz}} - \text{DiazC}_{\text{morpt}} - \text{DiazC}_{\text{morp}} \quad (17)$$

$$S(\text{DiazN}) = \text{DiazN}\mu - \text{DiazN}_{\text{graz}} - \text{DiazN}_{\text{morpt}} - \text{DiazN}_{\text{morp}} \quad (18)$$

$$S(\text{DiazP}) = \text{DiazP}\mu - \text{DiazP}_{\text{graz}} - \text{DiazP}_{\text{morpt}} - \text{DiazP}_{\text{morp}} \quad (19)$$

where $\text{PhytC}_{\text{morpt}}$ and $\text{DiazC}_{\text{morpt}}$ are the regular phytoplankton and diazotroph C mortality terms that contribute directly to the dissolved inorganic carbon (DIC) pool. $\text{PhytC}_{\text{morp}}$, $\text{PhytN}_{\text{morp}}$, and $\text{PhytP}_{\text{morp}}$ are regular phytoplankton mortality terms that contribute to the formation of detritus C (DetC), N (DetN), and P (DetP). $\text{DiazC}_{\text{morp}}$, $\text{DiazN}_{\text{morp}}$, and $\text{DiazP}_{\text{morp}}$ are diazotroph mortality terms that contribute to the formation of DetC , DetN , and DetP respectively.

In order to simplify the modifications in the biogeochemistry of the UVic_ESCM, zooplankton stoichiometry is kept constant. Sources and sinks of zooplankton N (ZoopN) are calculated as:

$$\text{ZoopN} = \gamma \cdot N_{\text{graz}} - N_{\text{exc}} - \text{ZoopN}_{\text{mor}} - \text{ZoopN}_{\text{graz}} \quad (20)$$

where $\text{ZoopN}_{\text{mor}}$ is a zooplankton mortality term that contributes to DetN . Hence, zooplankton C (ZoopC) and P (ZoopP) are calculated via,

$$\text{ZoopC} = \frac{\text{ZoopN}}{Q_{\text{zoo}}^{\text{N}}} \quad (21)$$

$$ZoopP = ZoopC \cdot Q_{zoo}^P \quad (22)$$

where $Q_{zoo}^N = 0.15$, and $Q_{zoo}^P = 9 \cdot 10^{-3}$. Finally, detritus sources and sinks for C ($S(DetC)$), N ($S(DetN)$), and P ($S(DetP)$) are described by:

$$S(DetC) = (1 - \gamma) \cdot C_{graz} + PhytC_{morp} + DiazC_{morp} + ZoopC_{mor} - C_{remi} - DetC_{graz} - C_{exp} + C_{impo} \quad (23)$$

$$S(DetN) = (1 - \gamma) \cdot N_{graz} + PhytN_{morp} + DiazN_{morp} + ZoopN_{mor} - N_{remi} - DetN_{graz} - N_{exp} + N_{impo} \quad (24)$$

$$S(DetP) = (1 - \gamma) \cdot P_{graz} + PhytP_{morp} + DiazP_{morp} + ZoopP_{mor} - P_{remi} - DetP_{graz} - P_{exp} + P_{impo} \quad (25)$$

Where C_{exp} , N_{exp} , P_{exp} and C_{impo} , N_{impo} , P_{impo} are the vertical export and import rates of C, N, and P respectively. $ZoopC_{mor}$ and $ZoopP_{mor}$ are zooplankton mortality terms. C_{remi} is C remineralization, defined in the same way as for N and C.

$$C_{remi} = remi_0 \cdot b^{cT} \cdot DetC \quad (26)$$

The latest biogeochemical configuration of the UVic.ESCM including regular and diazotrophic phytoplankton has 6 tracer variables within its marine ecological module ([Keller et al., 2012](#)): Nitrate, phosphate, phytoplankton, diazotrophs, zooplankton, and detritus. Phytoplankton, diazotrophs, zooplankton, and detritus were calculated in terms of either N or P, and related to C via the Redfield ratio (106C:6.6N:1P). The inclusion of the optimality-based model requires the explicit calculation of C, N, and P for regular and diazotrophic phytoplankton, as well as detritus. This results in a total of 12 tracer variables within the marine ecosystem compartment of the model.

3.3.2 Preliminary results

An initial simulation of 100 years was carried out to assess the initial trends of the UVic.ESCM coupled with the optimality-based phytoplankton model. The total content of carbon in the ocean stabilizes at about

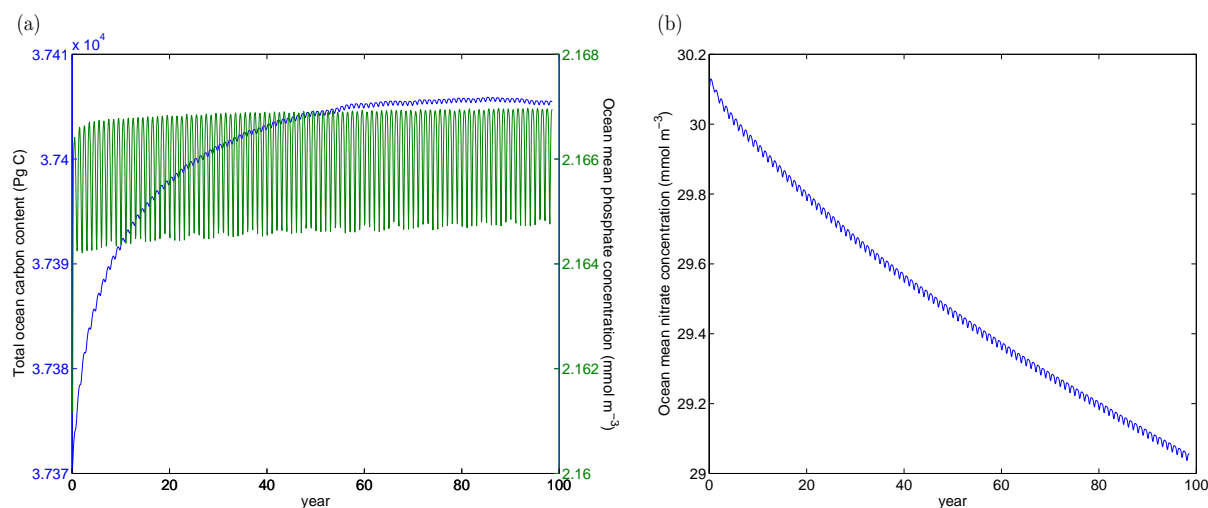


Figure 1: (a) Total oceanic carbon content (blue line) and global mean oceanic phosphate concentration (green line) of the first 100 years simulation of the UVic_ESCM coupled with the optimality-based phytoplankton model. (b) Global trend in mean oceanic nitrate concentration of the same model simulation.

3740.5 Pg of C, after an initial increase during the first 60 years of the simulation (Fig. 1a). The global phosphate (PO_4) concentration in the ocean also presents a slight increase over the first 60 years, reaching a mean stable concentration at about 2.166 $\text{mmol PO}_4 \text{ m}^{-3}$ (Fig. 1a). The major problem observed so far in the implementation of the optimality-based formulation is a constant decrease in nitrate (NO_3) in the ocean. Over the first 100 years, the mean ocean nitrate concentration decreases about 1 % (~ 1 $\text{mmol NO}_3 \text{ m}^{-3}$), from 30 to 29 $\text{mmol NO}_3 \text{ m}^{-3}$ (Fig. 1b). The major reason for this nitrogen loss is likely a misplacement of diazotrophic phytoplankton growth (Fig. 2), which results in very low N_2 fixation rates, therefore producing an imbalance in the oceanic nitrogen cycle.

Global vertically integrated uptake rates of C, N, and P for non-diazotrophic and diazotrophic phytoplankton are shown in Fig. 2. Primary production by non-diazotrophic phytoplankton (i.e. C-uptake) is highest in the tropical ocean, particularly over the Pacific and Indian ocean. This global pattern of PP is similar to the trend of the physiological C-based model obtained from the combination of satellite observations and optimality-based formulations (Chapter 3). The uptake rate of C is about 4 times higher than the N uptake rate, and about 16 times larger than the uptake of P. Global growth of diazotrophic phytoplankton occurs mainly over the Southern Ocean and northern North Atlantic. While the distribution of diazotrophic phytoplankton growth is poorly known, the general expectation is that diazotrophs mainly grow in areas

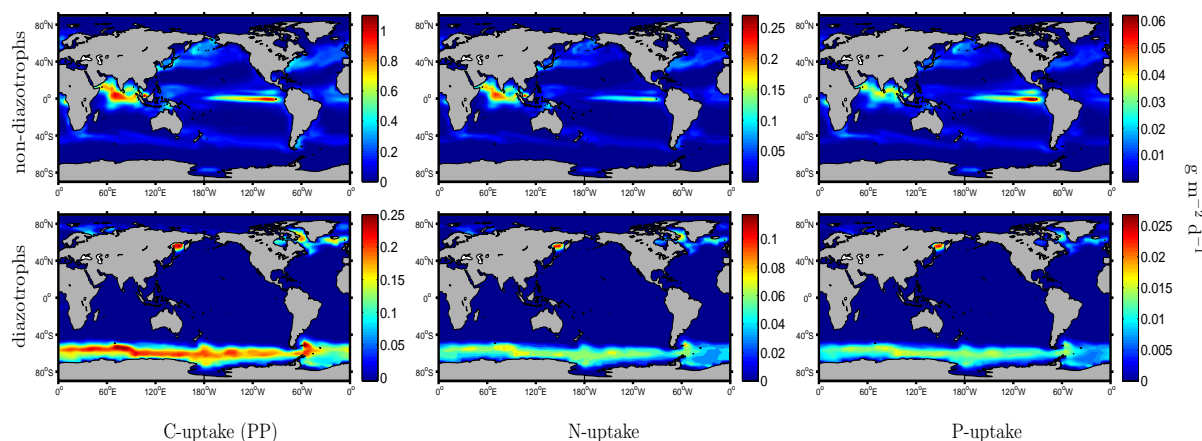


Figure 2: Vertically integrated uptake rates of C (i.e. primary production, $\text{g C m}^{-2} \text{d}^{-1}$), N ($\text{g N m}^{-2} \text{d}^{-1}$), and P ($\text{g P m}^{-2} \text{d}^{-1}$) for non-diazotrophic and diazotrophic phytoplankton (top and bottom panels respectively), averaged for the whole duration (i.e. 100 years) of the UVic_ESCM-optimality-based simulation.

where high N_2 fixation rates have been identified, specifically over the tropical Atlantic, eastern tropical Pacific, and Arabic sea (Sohm *et al.*, 2011). This global mismatch between diazotroph growth and N_2 fixation areas (Fig. 3a) results in very low and unrealistic annual N_2 fixation rates ($\sim 0.1 \text{ Tg C y}^{-1}$), producing a global imbalance in the nitrogen cycle (i.e. net nitrogen loss) due to much higher denitrification rates ($\sim 400 \text{ Tg C y}^{-1}$).

Denitrification occurs in the eastern tropical Pacific and Indian Sea, similar as in the previous model version of Keller *et al.* (2012), and as expected from observations (Codispoti, 2007) (Fig. 3b). Other two denitrification areas also appear in the northern Pacific and in the Southern Ocean at 180°W . The obtained annual global denitrification rate of $\sim 400 \text{ Tg C y}^{-1}$ exceeds most commonly accepted estimates (Codispoti, 2007; Gruber and Sarmiento, 1997). This high modelled denitrification rates might be a consequence of the unusual patterns in diazotroph growth and low N_2 fixation. The simulated global oxygen (O_2) concentration at ~ 300 meters shows the three major oxygen minimum zones (OMZ) over the Atlantic, Pacific and Indian Oceans (Stramma *et al.*, 2008) (Fig. 3c). Low oxygen concentrations are also simulated for the Southern Ocean and northern North Pacific. High denitrification rates in OMZs are also possible due to a poor constraint of the connection between the nitrogen and oxygen cycles, as the stoichiometric relationships between organic matter respiration, oxygen consumption and denitrification, have not yet been adjusted to the optimality-based formulations.

Modelled zonally averaged vertical profiles of PO_4 , dissolved inorganic carbon (DIC), and O_2 (Fig. 4) are

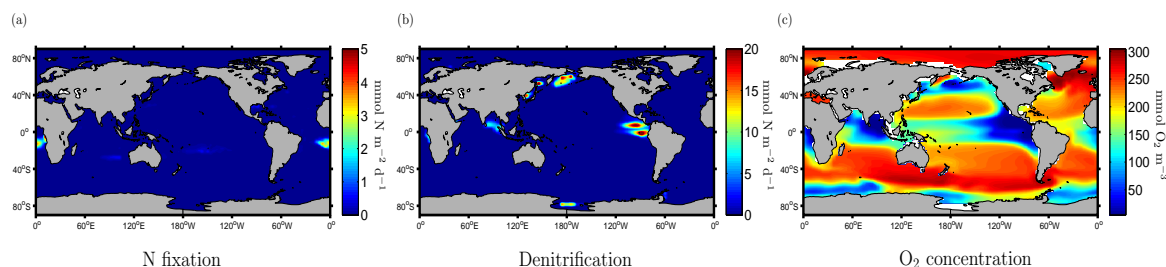


Figure 3: Vertically integrated N_2 fixation (a) and denitrification (b) rates averaged for the whole duration (i.e. 100 years) of the UVic_ESCM-optimality-based simulation. (c) Mean oxygen concentrations at ~ 300 m.

similar to previous model versions and observations from the World Ocean Atlas 2009 (WOA09) (*Keller et al., 2012*). PO_4 and DIC concentrations are high in the deep ocean across all shown ocean basins (Atlantic, Pacific and Indian). PO_4 and DIC present higher concentrations in southern latitudes in the Atlantic ocean, while for the Pacific and Indian basins, the highest concentrations are found in northern latitudes. OMZs are simulated for all three basins. In the Atlantic ocean, low oxygen concentrations are simulated in the tropical ocean, as reported by observations (*Stramma et al., 2008*), but there is also a second area of low O_2 in the southern part of the basin (Fig. 4). This low O_2 concentrations are likely a result of high respiration rates induced by the accumulation of organic matter, driven by the unusually high primary productivity of diazotrophic phytoplankton in this area.

3.4 Conclusions and future directions

This thesis evaluates global physiological constraints of phytoplankton growth. A global analysis of nutrient and light colimitation areas indicates that nutrient limitation dominates over the tropical and subtropical ocean, while light limitation of phytoplankton growth is found in high latitudes, particularly in the Southern Ocean (Chapter 1). Nitrogen is identified as the major limiting nutrient. As a consequence, a satellite- and model-based method was developed to infer global nitrate concentrations in the surface ocean. Global nitrate variations can be successfully simulated employing SST, MLD and surface-Chl data (Chapter 2). Combining the studies above, global primary production rates and phytoplankton-C surface concentrations are inferred using a physiological phytoplankton model. According to these estimates, C-based inferred primary production is highest in tropical regions, particularly over the Pacific ocean. The global contribution of phytoplankton to total POC is estimated to be $\sim 50\%$ in low latitudes, and $\sim 15\%$ in high latitudes (Chapter 3). The role of organic matter export in driving nitrogen loss processes was estimated by employing

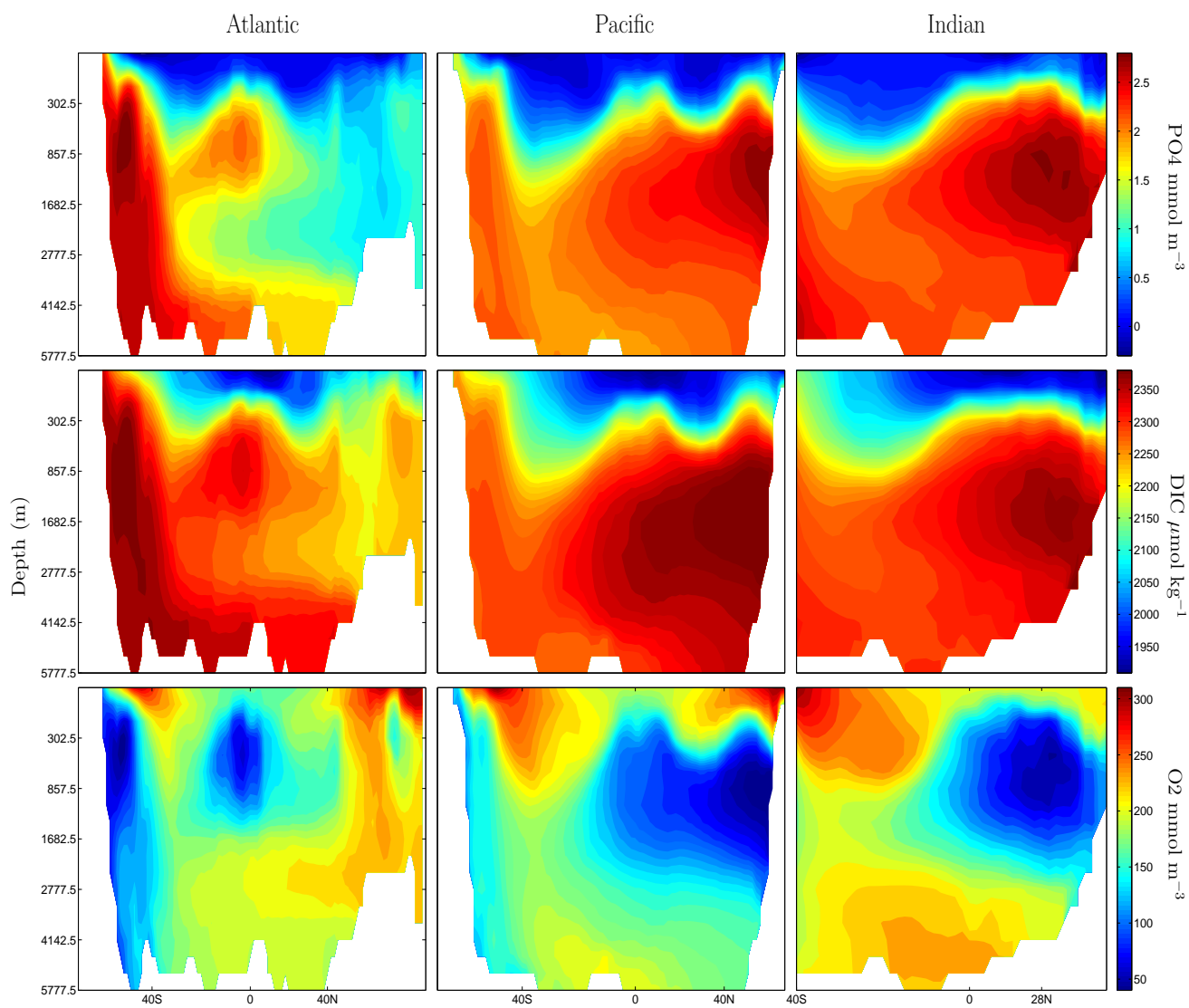


Figure 4: Zonally averaged ocean basin comparisons of PO4 (top), DIC (middle), and O2 (bottom) for the first 100 years simulation of the UVic_ESCM coupled with the optimality-based phytoplankton model.

bio-optical and satellite-based models of primary production and carbon export. Export production in the eastern tropical South Pacific oxygen minimum zone was highly correlated to depth-integrated rates of anammox, nitrate reduction, and nitrite oxidation. This suggests that the lateral distribution of N-cycling activity is mainly determined by the export of organic matter, which is the ultimate source of the required reactive substrates for N utilization in this OMZ (Chapter 4).

Optimality-based cell quota models are able to explain much of the variability in phytoplankton stoichiometry. The inclusion of physiological formulations is important to better constrain biogeochemical fluxes. However, the description of phytoplankton diversity also seems to be necessary in ecological models aiming to monitor and project global and regional environmental changes (i.e., accounting for acclimation and adaptation processes). The inclusion of optimality-based formulations in Earth system models has great potential in explaining and decoupling the cycling of carbon, nitrogen and other important biogeochemical elements. Different hypotheses suggest that changes in phytoplankton resource utilization can drive or contribute to alterations in the global climate system (*Sigman and Boyle, 2000; Martin, 1990*). Future work should be directed to the further development and inclusion of physiological formulations in Earth system models. A first step in this direction is presented in the Synthesis section of this thesis. Once the modelled biogeochemical patterns emerging from the coupling of the UVic_ESCM and the optimality-based model are better constrained, further work will be aimed to assess changes in primary production and export rates under varying ambient conditions derived from increased ocean surface stratification, as expected from ongoing climate change.

In terms of model development, a key aspect that still needs to be resolved is the influence of iron limitation on phytoplankton stoichiometry and growth. Iron has diverse constraints on phytoplankton physiology, affecting both nutrient and light assimilation dynamics (*Timmermans et al., 1994*). As major regions of the ocean are considered to be under iron limitation (*Martin et al., 1990; Boyd et al., 2007*), the description of iron dynamics within phytoplankton cellular physiology is a necessary requirement to accurately assess global patterns of phytoplankton stoichiometry. Culture studies evaluating changes in phytoplankton growth rates as a function of iron cell-quota are a fundamental initial step to precise the effects of iron on cellular growth. At the same time, global in situ observations of carbon:iron and iron:nitrogen ratios are necessary for model evaluation.

Cell-quota and physiological models of phytoplankton growth are an attractive tool to further understand the sensitivities of biogeochemical cycles to the biochemistry of marine microorganisms. The expansion of such models is inherently tied to laboratory studies aiming to investigate individual and combined limiting

effects of multiple nutrients and elements on cellular physiology. Without these observations, there cannot be a mechanistic understanding of the intracellular dynamics regulating growth, and hence significant novel model formulations cannot be expressed. The current knowledge on global biogeochemical cycles suggests that marine ecosystems are not only affected by changing ambient conditions, but can also drive and regulate alterations in the global climate system. Altogether, projections of the future climate system and its feedbacks with the marine environment can be better constrained through the expansion of physiological models and their evaluation in global Earth system models. The success of this task relies on the continuous and combined interaction of both modelling and experimental research.

References

- Arrigo, K. R. (2005), Marine microorganisms and global nutrient cycles, *Nature*, *437*, 349–355.
- Behrenfeld, M. J., E. Boss, D. A. Siegel, and D. M. Shea (2005), Carbon-based ocean productivity and phytoplankton physiology from space, *Global Biogeochemical Cycles*, *19*, GB1006, doi:10.1029/2004GB002299.
- Bopp, L., L. Resplandy, J. C. Orr, S. C. Doney, J. P. Dunne, M. Gehlen, P. Halloran, C. Heinze, T. Ilyina, R. Séférian, J. Tjiputra, and M. Vichi (2013), Multiple stressors of ocean ecosystems in the 21st century: projections with cmip5 models, *Biogeosciences*, *10*(10), 6225–6245, doi: 10.5194/bg-10-6225-2013.
- Boyd, P. W., T. Jickells, C. S. Law, S. Blain, E. a. Boyle, K. O. Buesseler, K. H. Coale, J. J. Cullen, H. J. W. de Baar, M. Follows, M. Harvey, C. Lancelot, M. Levasseur, N. P. J. Owens, R. Pollard, R. B. Rivkin, J. Sarmiento, V. Schoemann, V. Smetacek, S. Takeda, A. Tsuda, S. Turner, and a. J. Watson (2007), Mesoscale iron enrichment experiments 1993-2005: synthesis and future directions., *Science*, *315*, 612–617, doi: 10.1126/science.1131669.
- Codispoti, L. A. (2007), An oceanic fixed nitrogen sink exceeding 400 Tg N a⁻¹ vs the concept of homeostasis in the fixed-nitrogen inventory, *Biogeosciences*, *4*(2), 233–253, doi: 10.5194/bg-4-233-2007.
- Falkowski, P. G. (2000), Rationalizing elemental ratios in unicellular algae, *Journal of Phycology*, *36*, 3–6.
- Friedrichs, M. A., M.-E. Carr, R. T. Barber, M. Scardi, D. Antoine, R. A. Armstrong, I. Asanuma, M. J. Behrenfeld, E. T. Buitenhuis, F. Chai, J. R. Christian, A. M. Ciotti, S. C. Doney, M. Dowell, J. Dunne, B. Gentili, W. Gregg, N. Hoepffner, J. Ishizaka, T. Kameda, I. Lima, J. Marra, F. Mlin, J. K. Moore, A. Morel, R. T. O'Malley, J. O'Reilly, V. S. Saba, M. Schmeltz, T. J. Smyth, J. Tjiputra, K. Waters, T. K.

- Westberry, and A. Winguth (2009), Assessing the uncertainties of model estimates of primary productivity in the tropical pacific ocean, *Journal of Marine Systems*, 76, 113 – 133, doi: 10.1016/j.jmarsys.2008.05.010.
- Geider, R., and J. La Roche (2002), Redfield revisited: variability of C:N:P in marine microalgae and its biochemical basis, *European Journal of Phycology*, 37(1), 1–17, doi: 10.1017/S0967026201003456.
- Gruber, N., and J. L. Sarmiento (1997), Global patterns of marine nitrogen fixation and denitrification, *Global Biogeochemical Cycles*, 11(2), 235–266.
- Keller, D. P., A. Oschlies, and M. Eby (2012), A new marine ecosystem model for the university of victoria earth system climate model, *Geoscientific Model Development*, 5(5), 1195–1220, doi: 10.5194/gmd-5-1195-2012.
- Martin, J. (1990), Glacial-interglacial CO₂ change: The iron hypothesis, *Paleoceanography*, 5, 1–13, doi: 10.1029/PA005i001p00001.
- Martin, J., R. M. Gordon, and S. E. Fitzwater (1990), Iron in Antarctic waters, *Nature*, 345, 156–158, doi:10.1038/345156a0.
- Martiny, A. C., C. T. a. Pham, F. W. Primeau, J. a. Vrugt, J. K. Moore, S. a. Levin, and M. W. Lomas (2013a), Strong latitudinal patterns in the elemental ratios of marine plankton and organic matter, *Nature Geoscience*, 6, 279–283, doi: 10.1038/ngeo1757.
- Martiny, A. C., J. A. Vrugt, F. W. Primeau, and M. W. Lomas (2013b), Regional variation in the particulate organic carbon to nitrogen ratio in the surface ocean, *Global Biogeochemical Cycles*, 27(3), 723–731, doi: 10.1002/gbc.20061.
- Pahlow, M., and A. Oschlies (2009), Chain model of phytoplankton P, N and light colimitation, *Marine Ecology Progress Series*, 376, 69–83, doi: 10.3354/meps07748.
- Pahlow, M., H. Dietze, and A. Oschlies (2013), Optimality-based model of phytoplankton growth and diazotrophy, *Marine Ecology Progress Series*, 489, 1–16, doi: 10.3354/meps10449.
- Redfield, A. (1934), On the proportions of organic derivatives in sea water and their relation to the composition of plankton, *James Johnstone Memorial Volume, University Press of Liverpool*, 176–192.
- Rhee, G. (1978), Effects of N: P atomic ratios and nitrate limitation on algal growth, cell composition, and nitrate uptake, *Limnology and Oceanography*, 23(1), 10–25.

- Rhee, G.-Y. (1974), Phosphate uptake under nitrate limitation by *scenedesmus* sp. and its ecological implications, *Journal of Phycology*, *10*(4), 470–475, doi: 10.1111/j.1529-8817.1974.tb02742.x.
- Riahi, K., S. Rao, V. Krey, C. Cho, V. Chirkov, G. Fischer, G. Kindermann, N. Nakicenovic, and P. Rafaj (2011), Rcp 8.5a scenario of comparatively high greenhouse gas emissions, *Climatic Change*, *109*(1-2), 33–57, doi: 10.1007/s10584-011-0149-y.
- Riebesell, U., A. Krtzinger, and A. Oschlies (2009), Sensitivities of marine carbon fluxes to ocean change, *Proceedings of the National Academy of Sciences*, *106*(49), 20,602–20,609, doi: 10.1073/pnas.0813291106.
- Sarmiento, J. L., R. Slater, R. Barber, L. Bopp, S. C. Doney, A. C. Hirst, J. Kleypas, R. Matear, U. Mikolajewicz, P. Monfray, S. V., S. A. Spall, and R. Stouffer (2004), Response of ocean ecosystems to climate warming, *Global Biogeochemical Cycles*, *18*, GB3003, doi:10.1029/2003GB002134.
- Schneider, B., L. Bopp, M. Gehlen, J. Segschneider, T. L. Frölicher, P. Cadule, S. C. Doney, M. J. Behrenfeld, and F. Joos (2008), Climate-induced interannual variability of marine primary and export production in three global coupled climate carbon cycle models, *Biogeosciences*, *5*, 597–614.
- Sigman, D. M., and E. A. Boyle (2000), Glacial/interglacial variations in atmospheric carbon dioxide, *Nature*, *407*(6806), 859–869, doi: 10.1038/35038000.
- Sohm, J. A., E. A. Webb, and D. G. Capone (2011), Emerging patterns of marine nitrogen fixation, *Nature Reviews Microbiology*, *9*(7), 1740–1526, doi: 10.1038/nrmicro2594.
- Steinacher, M., F. Joos, T. L. Frölicher, L. Bopp, P. Cadule, V. Cocco, S. C. Doney, M. Gehlen, K. Lindsay, J. K. Moore, B. Schneider, and J. Segschneider (2010), Projected 21st century decrease in marine productivity: a multi-model analysis, *Biogeosciences*, *7*(3), 979–1005, doi: 10.5194/bg-7-979-2010.
- Stock, C. A., J. P. Dunne, and J. G. John (2014), Drivers of trophic amplification of ocean productivity trends in a changing climate, *Biogeosciences*, *11*(24), 7125–7135, doi: 10.5194/bg-11-7125-2014.
- Stramma, L., G. C. Johnson, J. Sprintall, and V. Mohrholz (2008), Expanding oxygen-minimum zones in the tropical oceans, *Science*, *320*(5876), 655–658, doi: 10.1126/science.1153847.
- Timmermans, K., W. Stolte, and H. Baar (1994), Iron-mediated effects on nitrate reductase in marine phytoplankton, *Marine Biology*, *121*, 389–396.

Weaver, A. J., M. Eby, E. C. Wiebe, C. M. Bitz, P. B. Duffy, T. L. Ewen, A. F. Fanning, M. M. Holland, A. MacFadyen, H. D. Matthews, K. J. Meissner, O. Saenko, A. Schmittner, H. Wang, and M. Yoshimori (2001), The uvic earth system climate model: Model description, climatology, and applications to past, present and future climates, *Atmosphere-Ocean*, *39*(4), 361–428, doi: 10.1080/07055900.2001.9649686.

Westberry, T., M. J. Behrenfeld, D. A. Siegel, and E. Boss (2008), Carbon-based primary productivity modeling with vertically resolved photoacclimation, *Global Biogeochemical Cycles*, *22*, GB2024, doi: 10.1029/2007GB003078.

Acknowledgements

First and foremost, I would like to thank my supervisors Andreas Oschlies and Markus Pahlow. Andreas gave me the opportunity to join his group back during my first days in Kiel, when I was not even sure what modelling really meant. That small vote of confidence allowed me to discover what I believe is my vocation, and for that I will always be thankful. Markus disposition to teach and help was truly unending. From the very beginning he treated me like a colleague more than like a student, which always filled me with confidence throughout my Phd years. Thank you for explaining me optimality-based models a hundred times.. and thank you for the next hundred times to come.

Very special thanks to Scarlett and Roberto who supported me and took care of me all this time. They are the kind of friends that last forever and I can only be thankful to have. Also thanks to my oldest and kindest German friend, Dana, for always being there for me, no matter what.

Thank you to the BM group for all the intimidating group meetings. While sometimes the deadlines and the hunger clouded my vision, the group meeting was one of the places where I learned the most, and where I saw real science taking place. I will always remember you all, and in particular all my fellow Phd students and those who collaborated closely with me, Fabian, Shubham, Jan, Fi, Bei, Alex, Levin, Jenny, Chris, David, Ivonne, and everyone else in the group.

Special thanks to two wonderful women who made possible the highlight of my Phd, Avan Antia and Katrin Meissner. Avan's continuous encouragement for excellence always provided me with an extra drive, and lead me to pursue the opportunity to visit Australia. Katrin's kindness and friendship truly made me feel like home in Sydney, and now it is like having a big sister in the other part of the world. Cheers to all my Aussie and pseudo-Aussie friends, Jules, Nicola, Willem, David, Alice, Swa, Jatin, Esteban, Daniel, Andrew and everyone in the CCRC, for making my time in Australia unforgettable. Grazie to a very beautiful person, Carolina, with whom I shared the most special moments in this wonderful experience.

Thank you to Thorsten Picker and all my Jiu-Jitsu team for resetting my mind after every hard day. Every war on the mats taught me a lesson for life.

And finally, gracias to the foundation of all. My parents, my sister, my grandmother and my uncle. Being far from home is not easy. Tough times are tougher, but accomplishments taste also different, somehow sweeter. Knowing that your unconditional support is always there fills me with confidence and makes me pursue new challenges. I now look forward to new adventures, taking with me something from each one of those mentioned above. Thank you all!

GEOMAR Helmholtz
Centre for Ocean Research Kiel
Biogeochemical Modelling division
<http://www.geomar.de/en/mitarbeiter/fb2/bm/larteaga/>

Düsternbrooker Weg 20
24105 Kiel, Germany
+49 431 600-402
larteaga@geomar.de

Curriculum Vitae
Lionel Arteaga

Research interests

The focus of my scientific research is the sensitivities of the global carbon cycle and its connection to changes in the global climate system. I specialize on the study of biogeochemical cycles through numerical models and satellite observations in order to understand the state of global marine ecosystems and their connection to past and future climate events.

Personal information

- **Name:** Lionel Alejandro Arteaga Quintero.
- **Nationality:** Venezuelan.
- **Date of birth:** 27th of June, 1985.
- **Place of birth:** Puerto Ordaz, Venezuela.

Education

- **Ph.D-Student Ocean Biogeochemistry.** Present. GEOMAR -University of Kiel.
Thesis title: *Combining model and satellite analyses to describe phytoplankton growth.*
Supervisors: Prof. Dr. Andreas Oschlies, Dr. Markus Pahlow.
Research Visit. March – September, 2014. Climate Change Research Center
University of New South of Wales.
Project: Adaptation of an optimality-based phytoplankton model into a global circulation earth-system climate model.
Supervisor: Ass. Prof. Katrin Meissner.
- **M.Sc. Biological Oceanography.** 2011. IFM-GEOMAR - University of Kiel.
Thesis title: *Evaluation of regional patterns of light and nutrient colimitation in the global ocean. A modelling approach.*
- **Lic. Biology.** 2008. Universidad Simón Bolívar.
Thesis title: *Description of the Venezuelan gulf upwelling system through satellite data.*
Honor distinction: Outstanding *licenciatura* dissertation.

Awards

- ISOS Integrated School of Ocean Sciences Kiel PhD miniproposal award: *Ocean Biogeochemistry under Changing Climate with a Phytoplankton Optimality-based model*.

Experience

- 2011 - Present: **Research assistant. GEOMAR Helmholtz Centre for Ocean Research Kiel:** Analysis of global phytoplankton growth limitations, primary production and export production employing a novel optimality-based model combined with satellite-based observations.
- 2014, Mar-Sep: **Visiting scientist. Climate Change Research Center, UNSW:** Improvement of the biogeochemical compartment of the UVic earth-system model through the incorporation of an adaptable optimality-based phytoplankton model.
- 2008 - 2009: **Research scientist. Oceanographic Digital Observatory, Universidad Simón Bolívar:** Analysis of the coastal upwelling system of Venezuela through remotely-sensed data. http://ood.cbm.usb.ve/wiki/surgencia_golfo_vzla
- 2007 - 2008: **Teaching assistant. Universidad Simón Bolívar.** Teaching and support activities on expeditions of the practical course of *Ecology II*, within the curriculum of the career on *General Biology*.

Peer-reviewed publications

- Arteaga, L., M. Pahlow, and A. Oschlies (2015), Global monthly sea-surface nitrate fields estimated from remotely sensed sea-surface temperature, chlorophyll, and modelled mixed layer depth, *Geophysical Research Letters*, doi: 10.1002/2014GL062937
- Arteaga, L., M. Pahlow, and A. Oschlies (2014), Global patterns of phytoplankton nutrient and light colimitation inferred from an optimality-based model, *Global Biogeochemical Cycles*, 28(7), 648–661, doi: 10.1002/2013GB004668
- Kalvelage, T., G. Lavik, P. Lam, S. Contreras, L. Arteaga, C. R. Löscher, A. Oschlies, A. Paulmier, L. Stramma, and M. M. M. Kuypers (2013), Nitrogen cycling driven by organic matter export in the South Pacific oxygen minimum zone, *Nature Geoscience*, 6(3), 228–234, doi: 10.1038/ngeo1739

Meetings

- **Arteaga, L**, Pahlow, M and A. Oschlies. *Changes in phytoplankton stoichiometry inferred optimality-based model*. **Oral presentation** at the *Aquatic Sciences Meeting*, Granada, Spain. February, 2015.
- **Arteaga, L**, Pahlow, M and A. Oschlies. *Global patterns of phytoplankton nutrient and light colimitation inferred from an optimality-based model*. **Poster presentation** at the *Ocean Sciences Meeting*, Honolulu, Hawaii. February, 2014.

 Lionel Arteaga

- **Arteaga, L**, Pahlow, M and A. Oschlies. *Satellite-derived ocean primary production inferred from an optimality-based phytoplankton model*. **Oral presentation** at the 45th International Liège Colloquium: *Primary production in the ocean: from the synoptic to the global scale*, Liège, Belgium. May, 2013.
- **Arteaga, L**, Pahlow, M and A. Oschlies. *Satellite-derived ocean primary production inferred from an optimality-based phytoplankton model*. **Poster presentation** at the *International Ocean Colour Science Meeting*, Darmstadt, Germany. May, 2013.
- **Arteaga, L**, Pahlow, M and A. Oschlies. *Light and Nutrient Colimitation in the Global Ocean*. **Oral presentation** at the *Ocean Strategic Services Services beyond 2015 (OSS2015) progress meeting*, Centre for Maritime Research and Experimentation, La Spezia, Italy. July, 2012.
- **Arteaga, L**, Pahlow, M and A. Oschlies. *Light and Nutrient Colimitation in the Global Ocean*. **Poster presentation** at the *European Geosciences Union General Assembly*, Vienna, Austria. April, 2012.
- Klein, E, Chollet I, Romero C, and **L. Arteaga**. *On the Size of Upwelling systems*. **Poster presentation** at the *Dynamics of Eastern Boundary Upwelling Ecosystems Symposium*, Las Palmas, Gran Canaria, Spain. June, 2008.

 Courses and Summer Schools

- ARC Climate System Science Winter School *Geophysical Fluid Dynamics*. Canberra, Australia. 16 – 20 June, 2014.
- SFB 754 Summer School *Climate-Biogeochemistry Interactions in the Tropical Ocean*. Kristineberg, Sweden. 18 – 30 August, 2013.
- GreenSeas Summer School *Global plankton data: ecosystems, monitoring and modelling in an era of global warming*. Cape Town, South Africa. 27 January – 3 February, 2013.
- *European Earth System and Climate Modelling School* (Organized by the Max Planck Institute for Meteorology -Hamburg- and the National Centre for Atmospheric Science -Reading-). Kos, Greece. 1 – 11 June, 2012.
- *Fortran for Scientific Computing*. High Performance Computing Center Stuttgart (HLRS), Stuttgart, Germany. 5 – 9 March, 2012.
- MEECE Summer School *Marine Ecosystem Evolution in a Changing Environment*. Ankara, Turkey. 7 – 14 September, 2011.
- 6th Sino-German Summer School, *Responses of Ocean Biogeochemistry to Global Change*. Kiel, Bremen and Bremerhaven, Germany. 26 July – 6 August, 2010.

 Oceanographic Cruises

- Benthic and biogeochemical sampling along the western Baltic Sea, on the German vessel *Alkor*. October, 2010.

Lionel Arteaga

Software skills

- Numerical computing: MATLAB, Fortran, R.
- Operative Systems: Unix (Mac), Linux, Windows.
- General: LaTeX, Microsoft office (Word, Power Point, Excel).

Languages

- Spanish: Mother tongue.
- English: Excellent.
- German: Level B1 (Intermediate).

Academic references

- Prof. Dr. Andreas Oschlies (PhD and Master supervisor, aoschlies@geomar.de)
- Dr. Habil. Markus Pahlow (PhD and Master co-supervisor, mpahlow@geomar.de)
- Ass. Prof. Katrin Meissner (PhD co-supervisor, k.meissner@unsw.edu.au)

Hiermit erkläre ich, dass die vorliegende Dissertation mit dem Titel:

**Assessment of global phytoplankton growth inferred from satellite and
physiological model-based analyses**

selbständig von mir angefertigt wurde. Die Dissertation - abgesehen von der Beratung durch die Betreuerin oder den Betreuer - ist nach Form und Inhalt meine eigene Arbeit und es wurden keine anderen als die angegebenen Quellen und Hilfsmittel verwendet. Die vorliegende Arbeit ist unter Einhaltung der Regeln guter wissenschaftlicher Praxis der Deutschen Forschungsgemeinschaft entstanden und wurde weder ganz noch zum Teil an anderer Stelle im Rahmen eines Prüfungsverfahrens vorgelegt oder veröffentlicht. Weiterhin erkläre ich mich einverstanden, dass diese Dissertation an die Bibliothek des GEOMAR und die Universitätsbibliothek der CAU weitergeleitet wird.

Lionel Alejandro Arteaga Quintero

Kiel, April 2015